

## Drivers and implications of declining fossil fuel CO<sub>2</sub> concentrations in Chinese cities revealed by radiocarbon measurements

Pingyang Li<sup>1,2</sup>, Boji Lin<sup>1,2,3</sup>, Zhineng Cheng<sup>1,2</sup>, Jing Li<sup>1,2</sup>, Jun Li<sup>1,2</sup>, Duohong Chen<sup>4,\*</sup>, Tao Zhang<sup>4</sup>, Run Lin<sup>1,2</sup>, Sanyuan Zhu<sup>1,2</sup>, Jun Liu<sup>4</sup>, Yujun Lin<sup>4</sup>, Shizhen Zhao<sup>1,2</sup>, Guangcai Zhong<sup>1,2</sup>, Zhenchuan Niu<sup>5,6</sup>, Ping Ding<sup>7</sup>, Gan Zhang<sup>1,2,\*</sup>

<sup>1</sup> State Key Laboratory of Advanced Environmental Technology, Guangzhou Institute of Geochemistry, Chinese Academy of Sciences, Guangzhou 510640, People's Republic of China

<sup>2</sup> Guangdong Key Laboratory of Environmental Protection and Resources Utilization, and Joint Laboratory of the Guangdong-Hong Kong-Macao Greater Bay Area for the Environment, Guangzhou Institute of Geochemistry, Chinese Academy of Sciences, Guangzhou 510640, People's Republic of China

<sup>3</sup> University of Chinese Academy of Sciences, Beijing 100049, People's Republic of China

<sup>4</sup> Environmental Key Laboratory of Regional Air Quality Monitoring, Ministry of Ecology and Environment, Guangdong Ecological and Environmental Monitoring Center, Guangzhou 510308, People's Republic of China

<sup>5</sup> State Key Laboratory of Loess, Institute of Earth Environment, Chinese Academy of Sciences, Xi'an 710061, People's Republic of China

<sup>6</sup> Institute of Global Environmental Change, Xi'an Jiaotong University, Xi'an 710061, People's Republic of China

<sup>7</sup> State Key Laboratory of Deep Earth Processes and Resources, Guangzhou Institute of Geochemistry, Chinese Academy of Sciences, Guangzhou 510640, People's Republic of China

Correspondence to: Gan Zhang (zhanggan@gig.ac.cn), Duohong Chen (chenduohong@139.com)

**Abstract.** China's clean air policies have successfully mitigated fossil fuel CO<sub>2</sub> (CO<sub>2ff</sub> or C<sub>ff</sub>) emissions in bottom-up inventories since 2013. Yet, evidence from top-down measurements and their underlying drivers remains ~~lacking~~limited. Here, we quantify C<sub>ff</sub> concentrations and fuel-specific contributions using atmospheric  $\Delta(^{14}\text{CO}_2)$  and  $\delta(^{13}\text{CO}_2)$  measurements across representative Chinese cities. We found ~~distinct~~regional ~~differences~~trends in C<sub>ff</sub> and co-emission characteristics: megacities like Guangzhou show ~~an indicative~~significant ~~inter-period decrease in wintertime C<sub>ff</sub> concentrations~~declines (of roughly 56–64% lower in 2022 than in 2010 in afternoon-equivalent terms decrease from 2010 to 2022) along with their source—regions, while smaller cities have yet to demonstrate ~~similar~~reductions comparable decreases. These ~~improvements~~changes are consistent with ~~an~~be attributed to a 23% ~~coal consumption~~ reduction in coal use, a 17% increase in the natural-gas use contribution (evidenced by stable isotope analysis), and improved combustion efficiency (indicated by a 63% ~~falling~~decline in R<sub>CO/CO<sub>2ff</sub></sub> ratios). Notably, the ~~24-year~~three-decade observational record (1998–2022) shows steeper declines in urban R<sub>CO/CO<sub>2ff</sub></sub> ratios than inventory estimates, suggesting current emission inventories may underestimate combustion efficiency improvements and CO emission reductions relative to C<sub>ff</sub> mitigations. These findings ~~are consistent with~~indicate nationwide progress toward mitigating C<sub>ff</sub> and co-emitted CO in major Chinese citiesemission peaks, with megacities leading the transition. They also underscore how coal-to-gas transitions and technological upgrades simultaneously advance air quality and climate goals. Importantly, our results highlight the critical need to integrate top-

35 down observational frameworks (e.g. radiocarbon measurements) with traditional inventories to better capture rapid, policy-  
driven emission changes and inform future co-benefit optimization strategies.

## 1 Introduction

As the world's largest energy consumer, China's heavy reliance on fossil fuels has resulted in severe air pollution and  
40 substantial fossil fuel CO<sub>2</sub> (CO<sub>2ff</sub> or C<sub>ff</sub>) emissions, accounting for 31 % of global fossil CO<sub>2</sub> emissions in 2022  
(Friedlingstein et al., 2023a). These emissions pose critical threats to public health and ecological stability. In response,  
China has enacted progressive policies including the 2013 Clean Air Action Plan (Zheng et al., 2018; Zhang et al., 2019),  
2018 Blue Sky Defense Battle, and 2022 Pollution-Carbon Synergy Plan, achieving co-benefits in air quality improvement  
and C<sub>ff</sub> mitigation as quantified through bottom-up inventories like Multi-resolution Emission Inventory for China (MEIC)  
45 (Shi et al., 2022). However, the effectiveness of these policies in reducing atmospheric C<sub>ff</sub> concentrations, and the underlying  
drivers of these reductions, remains unverified and unexplored through top-down observational approaches, creating a  
critical knowledge gap in climate policy assessment.

Bottom-up inventories and top-down measurements are approaches commonly used to determine atmospheric C<sub>ff</sub> emissions,  
but each has inherent limitations that can affect accuracy and reliability. Although bottom-up inventories are available at  
50 increasingly higher spatiotemporal resolution (Han et al., 2020), they are time-consuming to compile and update promptly,  
often lack quantitative estimation of uncertainty (Lo Vullo and Monforti, 2019), and frequently debated in attributing  
emissions to specific sources (Gurney et al., 2021). In contrast, top-down studies encompass all existing sources within a  
geographic region but struggle to achieve accurate partitioning of the fossil fuel and biospheric CO<sub>2</sub> contributions. This  
methodological impasse can be resolved by <sup>14</sup>C analysis, which exploits the unique <sup>14</sup>C-depletion signature of C<sub>ff</sub> compared  
55 to contemporary biogenic sources (Levin et al., 2003; Turnbull et al., 2006), enabling unambiguous fossil fuel emission  
quantification.

Urban areas, occupying merely 3 % of global land yet responsible for 75 % of global C<sub>ff</sub> emissions (reaching 80 % in China)  
(Dhakal, 2009; Duren and Miller, 2012), represent strategic priorities for emission mitigation. Recent advances in analytical  
tools can help identify key drivers of urban C<sub>ff</sub> reductions.  $\delta(^{13}\text{CO}_2)$  signatures successfully distinguished coal, oil, and  
60 natural gas contributions in cities like Beijing and Xi'an (Wang et al., 2022b), while  $\Delta\text{CO}/\text{C}_{\text{ff}}$  ( $\Delta\text{CO}$  denotes the difference  
between observed and background values;  $\Delta\text{CO} = \text{CO}_{\text{obs}} - \text{CO}_{\text{bg}}$ ) ratios tracked combustion efficiency variations across  
national (China, South Korea) and urban (Paris, Heidelberg) scales (Turnbull et al., 2011; Lee et al., 2020; Lopez et al., 2013;  
Rosendahl, 2022). To address the research gaps mentioned above, we performed spatiotemporal mapping of 2022 C<sub>ff</sub>  
concentrations across representative Chinese cities using dual-carbon isotope constraints ( $\Delta(^{14}\text{CO}_2) + \delta(^{13}\text{CO}_2)$ ) for fuel-  
65 specific source attribution. By integrating multi-source inventories with extended  $\Delta\text{CO}/\text{C}_{\text{ff}}$  observations through 2022, we  
developed a robust framework for top-down verification of policy-driven emission reductions. Our methodology not only

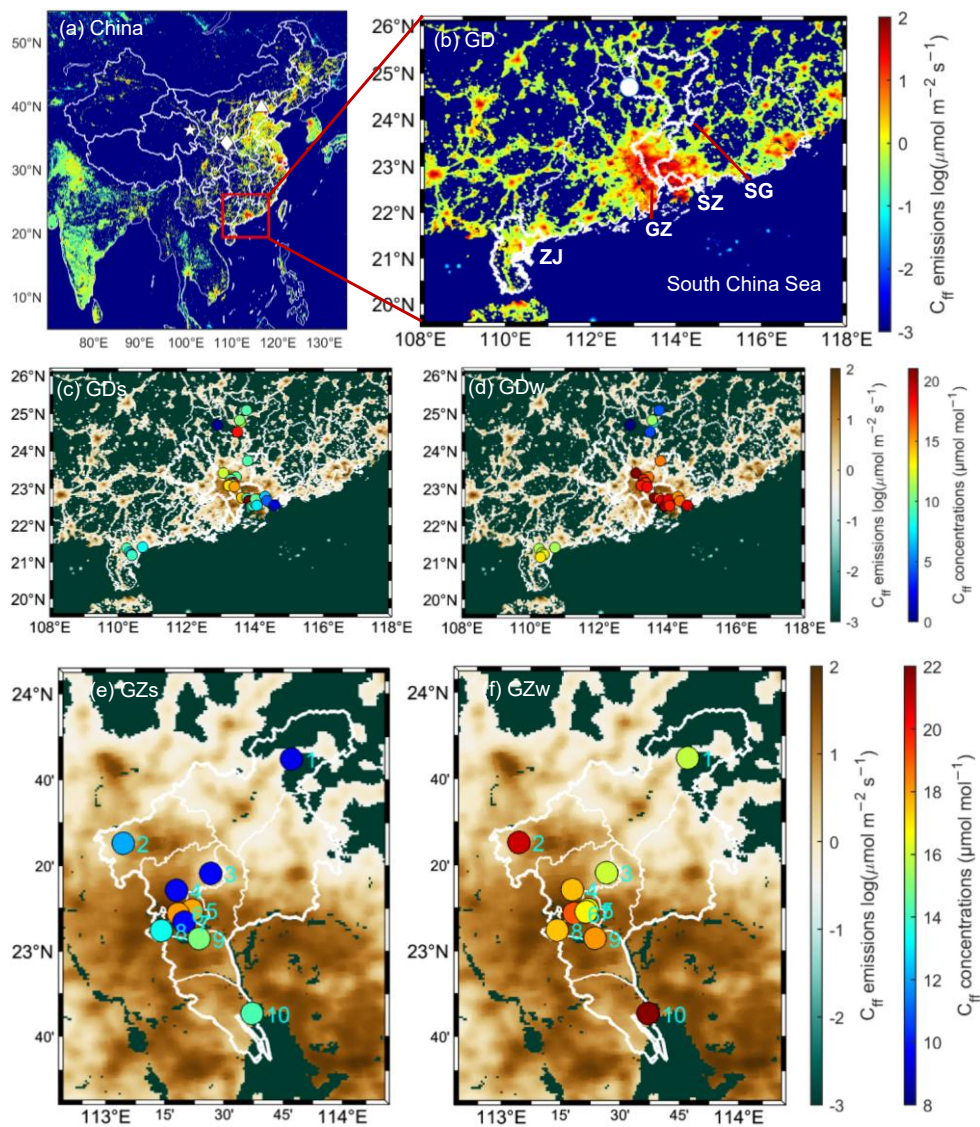
quantifies  $C_{ff}$  concentration decreases but also identifies the key mechanisms behind these reductions, offering critical insights for refining climate mitigation strategies and supporting sustainable urban development.

## 70 2 Data and methods

### 2.1 Study area and sample collection

We selected representative Chinese cities of varied population sizes for this study: Guangzhou, Shenzhen, and Beijing for megacities (urban permanent resident populations >10 million), Xi'an for supercities (5–10 million), Zhanjiang for large cities (1–5 million), and Shaoguan for medium and small cities (<1 million), which is retrieved from the Tabulation on 2020  
75 China Population Census by County (Council, 2022). Since we could obtain results in Beijing and Xi'an from previous studies, we conducted field sampling in the four cities in Guangdong Province, China (Fig. 1). Guangdong Province is located south of the Nanling Mountains and on the coast of the South China Sea, lying within subtropical and tropical low-latitude regions. The area experiences a prevailing southeast monsoon from the ocean during summer and a northeast monsoon from the continent during winter. The four cities in Guangdong Province differ in terms of area, population, gross  
80 domestic product (GDP),  $C_{ff}$  inventory emissions, population density, topographic elevation, and land use/land cover. Guangzhou and Shenzhen represent two of China's seven megacities — approximately 45 exist globally — within the Pearl River Delta (PRD), the world's largest urban agglomeration (Taubenböck et al., 2019). Guangzhou, the capital of Guangdong Province, has a population of 18.7 million, GDP of 2 884 billion Yuan, and built-up area covering 35.2 %. Shenzhen, a high-tech hub transformed by post-1978 reforms, hosts 17.7 million people with GDP reaching 3 239 billion  
85 Yuan and 53.8 % built-up coverage. In contrast, Zhanjiang (large city) and Shaoguan (medium and small city) have smaller populations — 7.0 million and 2.9 million respectively — and lower GDPs of 371.3 billion Yuan and 156.4 billion Yuan. Zhanjiang features extensive cultivated land (31.747.8 %) and coastal ports (Zmbs, 2025), while Shaoguan is distinguished by 74.58.4 % forest+vegetation coverage (Smbs, 2024).

90



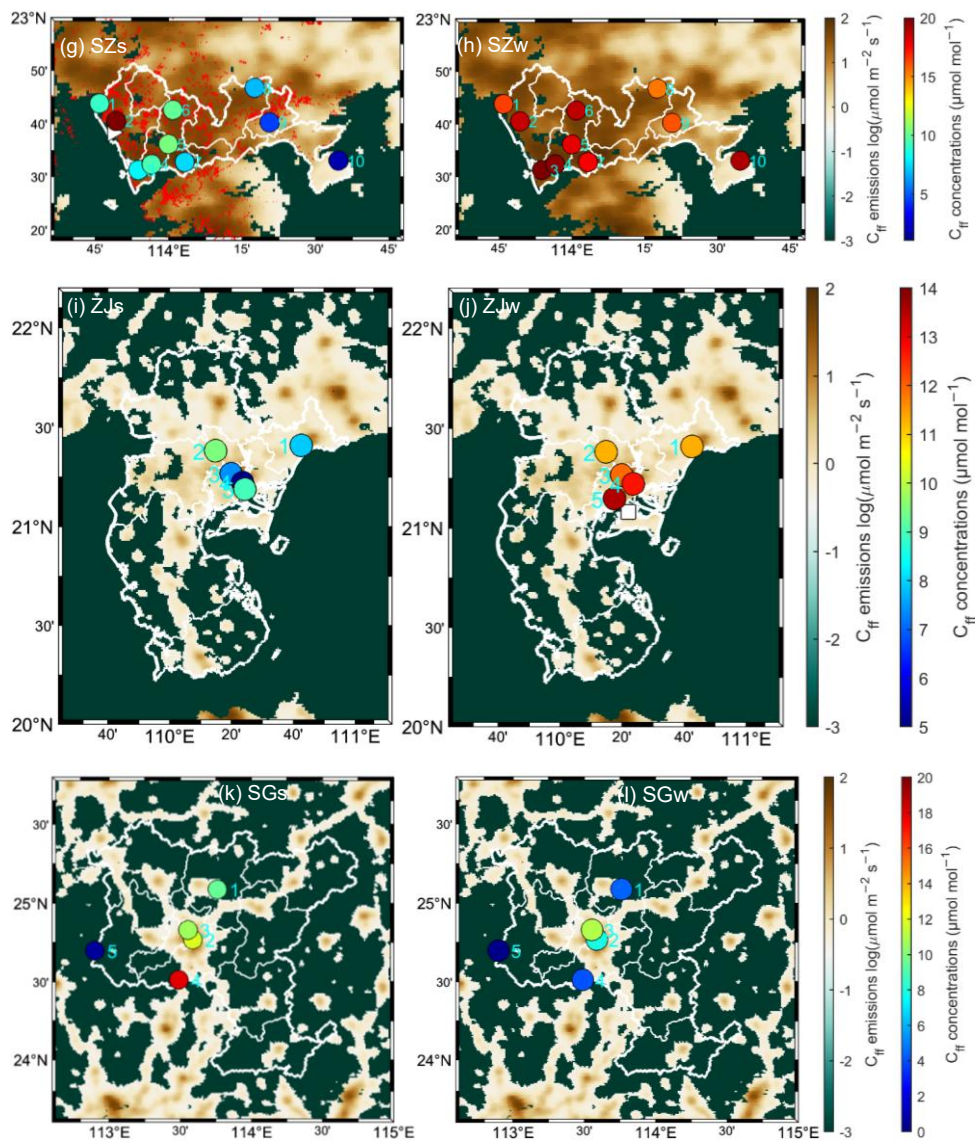


Figure 1: Locations of sampling sites and spatial distribution of  $C_{\text{ff}}$  concentrations during summer (s) and winter (w) in (c and d, GD) Guangdong Province and the cities of (e and f, GZ) Guangzhou, (g and h, SZ) Shenzhen, (i and j, ZJ) Zhanjiang, and (k and l, SG) Shaoguan. White-filled symbols denote Beijing ( $\blacktriangle$ ), Xi'an ( $\blacklozenge$ ), and Waliguan ( $\blackstar$ ) in (a); Nanling ( $\bullet$ ) in (b); Shenzhen Airport ( $\blacktriangleright$ ) in (g); and Zhanjiang Port ( $\blacktriangleleft$ ) in (j). Shenzhen's industrial land use (<https://download.geofabrik.de/asia/china.html>, last access: 11 Nov. 2025) is shown as red in (g), with the spatial distribution of all industrial enterprises and  $\text{CO}_2$ -emitting facilities documented in Li et al. (2025a). Colored circles in (c-l) represent the observations, while the shading indicates the  $C_{\text{ff}}$  inventory emissions from the Open-source Data Inventory for Anthropogenic  $\text{CO}_2$  (ODIAC) (Oda and Maksyutov, 2024) in August and December with  $1 \times 1$  km grid spacing. White lines indicate boundaries of cities in Guangdong Province (c and d), and boundaries of districts in the four cities (e-l). In (c) and (d), bold white lines indicate boundaries of nine cities of the Pearl River Delta. The left color bar represents the  $C_{\text{ff}}$  inventory emissions, while the right color bar represents the  $C_{\text{ff}}$  observations.

We collected 240 air samples from 30 sites during summer (28 July – 30 August 2022) and winter (12 December 2022 – 6 January 2023) campaigns, with weekly sampling in both periods. Because atmospheric transport variability can influence observed  $C_{\text{ff}}$  signals, we evaluated the meteorological representativeness of the sampling months using ERA5 diagnostics and trajectory analyses. Specifically, we assessed whether the August and December 2022 flask measurements were representative of typical summer and winter transport conditions. Standardized anomalies ( $z = (x_{\text{target}} - \mu_{\text{season}}) / \sigma_{\text{season}}$ ) were calculated for five ERA5 meteorological variables: 10 m eastward wind (U10), 10 m northward wind (V10), 2 m air temperature (T2M), surface pressure (SP), and planetary boundary-layer height (PBLH). Each target month was compared against (i) the concurrent 2022 seasonal background (June–July–August, JJA; December–January–February, DJF) and (ii) the 2010–2021 seasonal climatology. The choice of 2010 as the starting year ensures consistency with the earlier dataset from 2010, which is directly compared in this study. A month was considered “typical” when  $|z| \leq 1$  and its dominant wind direction fell within the canonical summer ( $90\text{--}225^\circ$ ) or winter ( $0\text{--}45^\circ$ ) monsoon sectors.

The locations and details of these sampling sites are shown in Fig. 1 and summarized in Table A1. Ten sampling sites were located in Guangzhou (GZ1–GZ10), ranging from urban downtown to suburban areas, selected based on spatial gradients of  $C_{\text{ff}}$  emissions derived from the Open-source Data Inventory for Anthropogenic  $\text{CO}_2$  (ODIAC) (Oda and Maksyutov, 2011; Oda and Maksyutov, 2024). Another 10 sampling sites were distributed uniformly throughout Shenzhen (SZ1–SZ10). In Zhanjiang (ZJ1–ZJ5) and Shaoguan (SG1–SG5), five sampling sites were selected in each city, primarily in urban areas, and distributed according to the first and second most dominant wind directions. These sites are located on the tower or on the roof of the building with 10–12 m extendable masts and are chosen to be free from any modifying effects of surrounding skyscrapers. Most of our sampling sites are generally no more than 300 m from the nearest air quality monitoring station. The sampling height is usually kept above 30 m above the ground level to avoid the influence of local sources. We assume that the measurements at the sampling sites in Guangzhou and Shenzhen are statistically sufficient to assess the whole cities, while those in Zhanjiang and Shaoguan are sufficient to assess the urban areas. Air sampling occurred between 13:00 and 17:00 local time, coinciding with the deepest planetary boundary layer and well-mixed atmospheric conditions. Post-filtration samples were transferred into pre-evacuated/flushed 3 L borosilicate flasks using 12 V micro-diaphragm pumps. These delivered a flow rate of  $6 \text{ L min}^{-1}$  at  $25^\circ \text{C}$  and  $101.3 \text{ kPa}$ , with pressurization to  $172.4\text{--}206.8 \text{ kPa}$ . The duration of the sampling was approximately 15–20 min in total.

## 2.2 Measurement of atmospheric CO<sub>2</sub> and $\delta(^{13}\text{C})$

135 Whole-air samples were dried using magnesium perchlorate at a constant flow rate of 25 mL min<sup>-1</sup>, controlled by a mass  
flow controller. The CO<sub>2</sub> concentrations and  $\delta(^{13}\text{C})$  values were then measured using a Picarro G2201-i high-precision  
carbon isotope analyzer (Picarro, Inc., Santa Clara, CA, USA) with cavity ring-down spectroscopy. Each sample was  
measured for 10 min, and only data from the final 5 min were used to calculate the average CO<sub>2</sub> concentration and  $\delta(^{13}\text{C})$   
value. Calibration for the CO<sub>2</sub> concentrations and the  $\delta(^{13}\text{C})$  values was performed using the method described by Wen et al.  
140 (2013) with three standards: (a)  $(409.47 \pm 0.02)$  ppm ( $\mu\text{mol mol}^{-1}$ ; similar hereafter),  $(-8.717 \pm 0.013)$  ‰; (b)  $(447.78 \pm 0.01)$   
 $\mu\text{mol mol}^{-1}$ ,  $(-9.759 \pm 0.006)$  ‰; and (c)  $(503.65 \pm 0.01)$   $\mu\text{mol mol}^{-1}$ ,  $(-11.456 \pm 0.004)$  ‰, obtained from the Chinese  
Academy of Meteorological Sciences. The CO<sub>2</sub> concentrations of the standards are traceable to the X2019 standard scale  
maintained by the Central Calibration Laboratory of the World Meteorological Organization, and the  $\delta(^{13}\text{C})$  values are  
traceable to the stable isotope laboratory of the Institute of Arctic and Alpine Research based on the NBS-19 and NBS-20  
145 standards. The  $\delta(^{13}\text{C})$  values were reported relative to the international Vienna Pee Dee Belemnite standard (Coplen, 1996).  
The precision was better than 0.2  $\mu\text{mol mol}^{-1}$  for CO<sub>2</sub> concentrations and 0.1 ‰ for  $\delta(^{13}\text{C})$  values.

## 2.3 Measurement of atmospheric $\Delta(^{14}\text{C})$

The residual air samples were transferred into a vacuum system at a flow rate of 300 mL min<sup>-1</sup>. It was then first passed  
150 through a cold trap consisting of dry ice and ethanol slurry to freeze out water, followed by passage through a liquid nitrogen  
cold trap ( $-196$  °C) to freeze down the CO<sub>2</sub> (Xu et al., 2007). The extracted and purified CO<sub>2</sub> was converted into graphite  
using the hydrogen reduction method. The graphite was then pressed into an aluminum holder for <sup>14</sup>C measurements using  
an NEC 0.5MV 1.5SDH-2 accelerator mass spectrometer (AMS, National Electrostatics Corporation, USA) (Zhu et al.,  
2015). Each measurement wheel typically comprises 13 primary standards (oxalic acid II), 13 secondary standards (IAEA-  
155 C7), 13 solid process blanks (*p*-phthalic acid), 6 gas process blanks (<sup>14</sup>C-free CO<sub>2</sub> in synthetic air from a cylinder), and some  
authentic air samples. The results are presented as  $\Delta(^{14}\text{C})$ , which is the per mill (‰) deviation from the absolute radiocarbon  
reference standard, corrected by fractionation and decay (Stuiver and Polach, 1977). We analyzed 17 pairs of parallel air  
samples to evaluate the quality control and assurance of the entire sampling and laboratory analysis process, including  
sampling, extraction, graphitization, and AMS measurement. The AMS measurement uncertainty and the average deviation  
160 are  $(2.1 \pm 0.3)$  ‰ and  $(0.2 \pm 2.9)$  ‰, respectively (see Fig. A1). We thus specify a one-sigma measurement uncertainty of  
2.9 ‰ for  $\Delta(^{14}\text{C})$  based on these repeat measurements of air samples.

#### 2.4 C<sub>ff</sub> concentration estimation (incorporated biomass burning emissions)

Recently added atmospheric CO<sub>2</sub> (CO<sub>2obs</sub> or C<sub>obs</sub>) is thought to consist of background CO<sub>2</sub> (CO<sub>2bg</sub> or C<sub>bg</sub>) and excess CO<sub>2</sub> (CO<sub>2xs</sub> or C<sub>xs</sub>). The C<sub>xs</sub> mainly includes C<sub>ff</sub> and biogenic CO<sub>2</sub> (CO<sub>2bio</sub> or C<sub>bio</sub>). The corresponding  $\Delta(^{14}\text{C})$  values are expressed as  $\Delta_{\text{obs}}$ ,  $\Delta_{\text{bg}}$ ,  $\Delta_{\text{ff}}$  (-1000 ‰, zero <sup>14</sup>C content), and  $\Delta_{\text{bio}}$ , respectively. The mass balance equations for atmospheric CO<sub>2</sub> and  $\Delta(^{14}\text{C})$  are expressed as follows (Levin et al., 2003):

$$C_{\text{obs}} = C_{\text{bg}} + C_{\text{xs}} = C_{\text{bg}} + C_{\text{ff}} + C_{\text{bio}} \quad (1)$$

$$C_{\text{obs}}\Delta_{\text{obs}} = C_{\text{bg}}\Delta_{\text{bg}} + C_{\text{ff}}\Delta_{\text{ff}} + C_{\text{bio}}\Delta_{\text{bio}} \quad (2)$$

$$C_{\text{ff}} = \frac{C_{\text{obs}}(\Delta_{\text{bg}} - \Delta_{\text{obs}})}{\Delta_{\text{bg}} + 1000\text{‰}} - \frac{C_{\text{bio}}(\Delta_{\text{bg}} - \Delta_{\text{bio}})}{\Delta_{\text{bg}} + 1000\text{‰}} = \frac{C_{\text{obs}}(\Delta_{\text{bg}} - \Delta_{\text{obs}})}{\Delta_{\text{bg}} + 1000\text{‰}} - \beta \quad (3)$$

The added C<sub>ff</sub> component is determined using Eq. (3). The CO<sub>2</sub> and  $\Delta(^{14}\text{C})$  from other sources, such as air-sea exchange (see Appendix C1) and nuclear facilities (see Appendix C2), have been neglected owing to their relatively small amounts. The second term ( $\beta$ ) represents a disequilibrium correction for the effect of CO<sub>2</sub> sources from biospheric exchange with distinct  $\Delta(^{14}\text{C})$  signatures relative to atmospheric values, primarily attributed to heterotrophic respiration (Rh) and biomass burning (BB). We quantified  $\beta$  using integrated modeling frameworks (see Appendixes B and C3). The heterotrophic respiration correction ( $\beta_{\text{Rh}}$ ) was derived from FLEXPART simulations (Pisso et al., 2019) with CASA-GFED4s data (Randerson et al., 2017; Van Der Werf et al., 2017), yielding values of  $(-0.06 \pm 0.03) \mu\text{mol mol}^{-1}$  in summer and  $(-0.11 \pm 0.04) \mu\text{mol mol}^{-1}$  in winter. The biomass burning corrections ( $\beta_{\text{BB}}$ ) was calculated under two assumptions: (1)  $\Delta(^{14}\text{C})$  endmembers assume 100 % perennial biomass, and (2) C<sub>BB</sub> emissions represent 100 % of C<sub>bio\_edgar</sub> in EDGAR2024 (covering open and closed combustion) (Edgar, 2024).  $\beta_{\text{BB}}$  showed maximum values of  $(-0.09 \pm 0.08) \mu\text{mol mol}^{-1}$  during summer and  $(-0.24 \pm 0.12) \mu\text{mol mol}^{-1}$  during winter. The combined correction ( $\beta = \beta_{\text{Rh}} + \beta_{\text{BB}}$ ) under the maximum-assumption simulation was  $(-0.16 \pm 0.09) \mu\text{mol mol}^{-1}$  in summer and  $(-0.35 \pm 0.15) \mu\text{mol mol}^{-1}$  in winter, which contrasts with the seasonal pattern in Turnbull et al. (2009):  $(-0.5 \pm 0.2) \mu\text{mol mol}^{-1}$  during summer and  $(-0.2 \pm 0.1) \mu\text{mol mol}^{-1}$  during winter. This study is the first to explicitly account for/integrate BB emissions within a C<sub>ff</sub> estimation framework, allowing us to quantify their contribution and associated uncertainty relative to revealing its dominant impact over Rh under our these assumptions. To maintain methodological consistency and comparability with previous work, for the final C<sub>ff</sub> values reported here adopt the correction estimations, we applied the corrections from Turnbull et al. (2009), to maintain methodological consistency and comparability with previous work which does not explicitly include BB. Nevertheless, our simulations, which incorporate BB emissions and their uncertainties, indicate that the broad comparability ( $\leq -0.5 \mu\text{mol mol}^{-1}$ ) in the magnitude of the required corrections ( $\leq -0.5 \mu\text{mol mol}^{-1}$ ) is broadly consistent with Turnbull et al. (2009) provides independent support for the applied values, and our simulations confirm that the our main conclusions are robust across this range of potential corrections.

## 2.5 C<sub>ff</sub> footprint by FLEXPART model

Surface flux sensitivity ~~simulations~~ ~~of~~ C<sub>ff</sub> were ~~performed~~ ~~conducted~~ using the FLEXible PARTicle (FLEXPART) dispersion model (version 10.4) (Pisso et al., 2019). In this study, FLEXPART is used to characterize source–receptor sensitivities (“footprints”) to support qualitative interpretation of the sampled upwind regions and potential source influences; it is not used to meteorologically normalize the long-term trends in C<sub>ff</sub>. The model produced source–receptor relationships, often referred to as “footprints” for atmospheric surface measurements, which represent the response of the observations at a measuring station to a source emission. The footprints are calculated using driven by global meteorological fields from the National Centers for Environmental Prediction’s Climate Forecast System (CFSv2) Reanalysis model (Saha et al., 2011). They are computed by releasing 10 000 virtual particles from each receptor at each sampling time and tracking them backward for 30 days over the domain of 0°–60° N, 70° E–150° E, with resolution of 0.1°×0.1°.

## 2.6 Fuel-specific fractions of C<sub>ff</sub> by Keeling plot and Bayesian mixing model

The method to determine coal, oil, and natural gas (i.e., fossil fuel type) fractions of C<sub>ff</sub> is described briefly using a Keeling plot (Miller and Tans, 2003) and the Bayesian mixing model (MixSIAR) (Stock et al., 2018). We calculated the excess  $\delta(^{13}\text{C})$  (intercepts  $\delta_{\text{xs}}$ , Eq. (4)) above the background level based on the best-fit lines in the Keeling plot. To determine the  $\delta(^{13}\text{C})$  of the fossil fuel source ( $\delta_{\text{ff}}$ , Eq. (5)), we estimated the weighted averages of the fossil fractions F<sub>ff</sub> using a two end-member mixing analysis on C<sub>xs</sub>. The  $\delta(^{13}\text{C})$  of the biogenic source ( $\delta_{\text{bio}}$ ) was set to  $-26.1\text{‰}$ , which is the average  $\delta(^{13}\text{C})$  value of the background air plus the  $-16.8\text{‰}$  discrimination by the terrestrial ecosystem (Bakwin et al., 1998). We then estimated the coal, oil, and natural gas fractions of C<sub>ff</sub> (F<sub>coal</sub>, F<sub>oil</sub>, and F<sub>ng</sub>, Eqs. (6) and (7)) using a Bayesian tracer mixing model framework implemented as an open-source R package. The model used the  $\delta_{\text{ff}}$  values as mixing data and the end-member  $\delta(^{13}\text{C})$  signatures of coal, oil, and natural gas as the source data.

We adopted the end-member  $\delta(^{13}\text{C})$  signatures measured in Beijing:  $\delta_{\text{coal}} = (-24.3 \pm 0.2)\text{‰}$ ,  $\delta_{\text{oil}} = (-28.9 \pm 0.5)\text{‰}$  and  $\delta_{\text{ng}} = (-33.2 \pm 0.9)\text{‰}$  (Wang et al., 2022a). This selection was based on three considerations: First, coal  $\delta(^{13}\text{C})$  signatures exhibit remarkable regional stability in China. Second, oil signatures from the Pearl River Mouth Basin of  $(-28.1 \pm 1.6)\text{‰}$  (Cheng et al., 2013) show close agreement with Beijing values of  $(-28.9 \pm 0.5)\text{‰}$ . Third, measured natural gas signatures like  $(-33.2 \pm 0.9)\text{‰}$  in Beijing and  $(-32.0 \pm 0.1)\text{‰}$  in Xi’an are significantly enriched compared to literature averages [ $-39.5\text{‰}$  in Beijing and  $(-38.9 \pm 2.6)\text{‰}$  in Pearl River Mouth Basin] (Ping et al., 2018; Quan et al., 2018), as using the lower literature values would lead to underestimation of natural gas contributions.

$$\delta_{\text{obs}} = C_{\text{bg}}(\delta_{\text{bg}} - \delta_{\text{xs}}) \times \frac{1}{C_{\text{obs}}} + \delta_{\text{xs}} \quad (4)$$

$$\delta_{\text{xs}} = F_{\text{ff}}\delta_{\text{ff}} + (1 - F_{\text{ff}})\delta_{\text{bio}} \quad (5)$$

$$\delta_{\text{ff}} = F_{\text{coal}}\delta_{\text{coal}} + F_{\text{oil}}\delta_{\text{oil}} + F_{\text{ng}}\delta_{\text{ng}} \quad (6)$$

$$1 = F_{\text{coal}} + F_{\text{oil}} + F_{\text{ng}} \quad (7)$$

225

### 2.7 Correlation of $C_{\text{ff}}$ and CO and derivation of the ~~ir~~-emission ratio

We calculated Pearson correlation coefficient ( $r$ ) between  $C_{\text{ff}}$  and CO enhancement ( $\Delta\text{CO} = \text{CO}_{\text{obs}} - \text{CO}_{\text{bg}}$ ), and observational ~~emissionconcentration~~ ratio of  $\Delta\text{CO}$  to  $C_{\text{ff}}$  ( $R_{\text{CO}/\text{CO}_{2\text{ff}}}$ ) [ppb ppm<sup>-1</sup> (nmol μmol<sup>-1</sup>; similar hereafter)] using linear least squares regression. The  $R_{\text{CO}/\text{CO}_{2\text{ff}}}$  ratios were derived from the regression slopes of  $\Delta\text{CO}$  versus  $C_{\text{ff}}$  concentrations. Here,

230

CO and CO<sub>2ff</sub> enhancements are defined relative to a regional background site, which is intended to represent upwind regional conditions rather than a completely remote, pristine background. Consequently, the inferred ΔCO and C<sub>ff</sub>, and thus the derived R<sub>CO/CO<sub>2ff</sub></sub> ratios, may include contributions from emissions outside the target city. We do not explicitly correct for this potential bias, but we consider it as an additional source of uncertainty when comparing observational R<sub>CO/CO<sub>2ff</sub></sub> with city-level I<sub>CO/CO<sub>2ff</sub></sub> ratios from emission inventories.

235

To correct for the contribution of non-fossil CO<sub>2</sub> in the observed enhancement ( $C_{\text{xs}}$ ), the ~~emissionconcentration~~ ratio  $R_{\text{CO}/\text{CO}_{2\text{ff}}}$  was estimated by dividing observed  $R_{\text{CO}/\text{CO}_2}$  by 0.8 for sites and times without Δ(<sup>14</sup>CO<sub>2</sub>) observations.

240

Equivalently, we assume  $C_{\text{ff}}/C_{\text{xs}} = 0.8$  (i.e., 20% of  $C_{\text{xs}}$  is non-fossil), so that  $R_{\text{CO}/\text{CO}_{2\text{ff}}} = R_{\text{CO}/\text{CO}_2\text{xs}} / (C_{\text{ff}}/C_{\text{xs}}) = R_{\text{CO}/\text{CO}_2\text{xs}} / 0.8$  for those subsets. Previous urban Δ(<sup>14</sup>CO<sub>2</sub>) and CO–CO<sub>2</sub> studies (Turnbull et al., 2011; Lopez et al., 2013; Newman et al., 2016; Miller et al., 2020) have shown that ~10–30 % (Table E1) of the total CO<sub>2</sub> enhancement above background during daytime/ afternoon is typically of non-fossil origin, while CO is emitted almost exclusively from fossil-fuel combustion. Thus, the 20 % correction represents a reasonable first-order approximation for well-mixed afternoon conditions. Our Δ(<sup>14</sup>CO<sub>2</sub>)-based source separation (Sect. 3.2) provides city/season-dependent  $C_{\text{ff}}/C_{\text{xs}}$  constraints that are broadly consistent with this range.

245

For comparison, the inventory emission ratio of CO to  $C_{\text{ff}}$  ( $I_{\text{CO}/\text{CO}_{2\text{ff}}}$ ) [ppb ppm<sup>-1</sup> (nmol μmol<sup>-1</sup>)] was calculated following Lee et al. (2020) as:

$$I_{\text{CO}/\text{CO}_{2\text{ff}}} = E_{\text{CO}}/E_{\text{CO}_{2\text{ff}}} \times M_{\text{CO}_2}/M_{\text{CO}} \quad (8)$$

where  $E_{\text{CO}}$  and  $E_{\text{CO}_{2\text{ff}}}$  represent the total CO and  $C_{\text{ff}}$  emissions (Tg a<sup>-1</sup>), summed over all grid cells within the relevant administrative boundaries from MEIC v1.4, MIX v2, and EDGAR 2024 inventories; and  $M_{\text{xCO}}$  and  $M_{\text{CO}_2}$  refers to the molar masses of CO and CO<sub>2</sub> in grams per mole (g mol<sup>-1</sup>).

250

### 3 Results and discussions

#### 3.1 Background selection

We conducted atmospheric observations of CO<sub>2</sub> and its carbon isotope composition ( $\Delta(^{14}\text{C})$  and  $\delta(^{13}\text{C})$ ) in Guangzhou, Shenzhen, Zhanjiang, and Shaoguan in Guangdong Province, South China, during the summer and winter of 2022. To attribute CO<sub>2</sub> enhancements ( $C_{\text{xs}}$ ) to a particular region, it is necessary to isolate the component of the observed concentration attributable to fluxes within the region by removing the background (Karion et al., 2021). High-elevation mountains, representing the free troposphere, were considered ideal background locations for use in this study (Turnbull et al., 2009). Specifically, the Nanling site (NL, 1700 m above sea level (a.s.l.)), one of the 30 sampling sites of this study (SG5; Table A1), was selected because it serves as the nearest regional background site for the study areas with relatively complex boundary conditions (for more reasons see Appendix D). The “annual” CO<sub>2</sub> and  $\Delta(^{14}\text{C})$  averages at NL station, calculated as averages of summer and winter measurements, were  $(418.5 \pm 7.3) \mu\text{mol mol}^{-1}$  and  $(-7.1 \pm 3.9) \text{‰}$ , respectively. These values closely match those observed at Jungfraujoch (JFJ, 3580 m a.s.l.) and appear in the upper-right section of the Keeling plot of  $\Delta(^{14}\text{C})$  and CO<sub>2</sub> (i.e., scatter plot between  $\Delta(^{14}\text{C})$  and inverse of CO<sub>2</sub> mole fractions) representing background conditions (Pataki et al., 2003). This positioning becomes evident when comparing with Waliguan (WLG, 3890 m a.s.l.) station data (Fig. 2). The advantage of using the Keeling plot method to screen background data is that it simultaneously accounts for both higher values of  $\Delta(^{14}\text{C})$  and lower values of CO<sub>2</sub> (Zhou et al., 2024). The  $\Delta(^{14}\text{C})$  averages at NL were the highest among the 30 sampling sites considered in this study, with values of  $(-3.7 \pm 1.3) \text{‰}$  in summer and  $(-10.6 \pm 0.8) \text{‰}$  in winter (Table A1). ~~We selected a regional (rather than urban) background site in 2022 to capture higher C<sub>4</sub> concentrations. This approach establishes a lower baseline for analyzing C<sub>4</sub> reduction in subsequent sections.~~

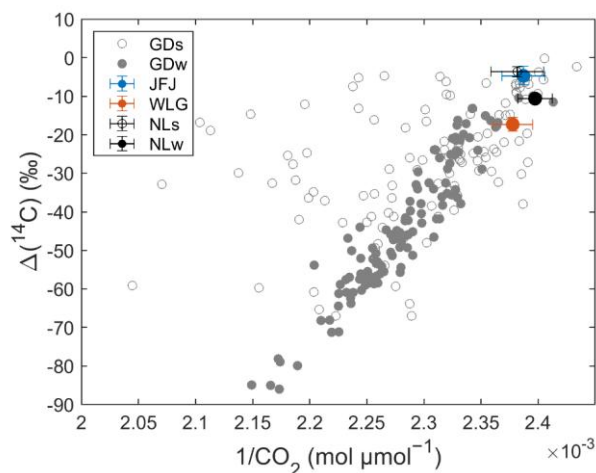


Figure 2: Keeling plot of  $\text{CO}_2$  and  $\Delta(^{14}\text{C})$  measurements from Guangdong Province in summer (GDs) and winter (GDw), and background stations including JFJ (Jungfrauoch) (Emmenegger et al., 2024b, a), WLJ (Waliguan) (Liu et al., 2024; Lan et al., 2023), and NL (Nanling) (this study) in 2022. For the JFJ background site, the complete 2022 dataset was used to calculate a true annual mean. For the WLJ background site,  $\text{CO}_2$  concentrations were obtained from the World Data Centre for Greenhouse Gases (WDCGG, <https://gaw.kishou.go.jp/>, last accessed: April 21, 2024), while  $\Delta(^{14}\text{C})$  observations were obtained from Liu et al. (2024). For the NL background site,  $\text{CO}_2$  and  $\Delta(^{14}\text{C})$  observations were obtained from two campaigns in August and December 2022, representing typical summer and winter conditions.

### 3.2 $\text{CO}_2$ , $\Delta(^{14}\text{C})$ , $C_{\text{xs}}$ and $C_{\text{ff}}$ concentrations

$\text{CO}_2$  concentrations in Guangzhou, Shenzhen, Zhanjiang, and Shaoguan were  $(438.8 \pm 12.3)$ ,  $(435.0 \pm 12.7)$ ,  $(444.2 \pm 17.2)$ , and  $(431.6 \pm 10.5)$   $\mu\text{mol mol}^{-1}$  (multisite mean and one-sigma standard deviation), respectively; the corresponding  $\Delta(^{14}\text{C})$  values were  $(-40.7 \pm 13.4)$  ‰,  $(-37.2 \pm 24.1)$  ‰,  $(-28.8 \pm 13.8)$  ‰, and  $(-25.0 \pm 14.9)$  ‰, respectively. Relative to the background,  $\text{CO}_2$  concentrations in the four cities were enhanced by  $(20.3 \pm 12.5)$ ,  $(16.5 \pm 13.5)$ ,  $(25.8 \pm 16.7)$ , and  $(13.1 \pm 10.1)$   $\mu\text{mol mol}^{-1}$  ( $C_{\text{xs}}$ ), respectively; the mean  $\Delta(^{14}\text{C})$  was depleted by  $(-33.6 \pm 11.3)$  ‰,  $(-29.9 \pm 22.3)$  ‰,  $(-21.5 \pm 11.7)$  ‰, and  $(-17.8 \pm 15.7)$  ‰ ( $\Delta\Delta(^{14}\text{C})$ ), respectively, reflecting the marked influence of  $^{14}\text{C}$ -free  $\text{CO}_2$  emissions from fossil fuel combustion. The fossil fuel and biogenic fractions of  $C_{\text{xs}}$ ,  $C_{\text{ff}}$  and  $C_{\text{bio}}$ , were determined using a two end-member mixing analysis. The  $C_{\text{ff}}$  fractions were  $(79 \pm 5)$  ‰,  $(73 \pm 6)$  ‰,  $(59 \pm 4)$  ‰, and  $(53 \pm 13)$  ‰ during winter in Guangzhou, Shenzhen, Zhanjiang, and Shaoguan, respectively. In comparison with other cities worldwide (Table E1, Fig. E1), we observed higher  $C_{\text{ff}}$  fractions ( $>70$  ‰) in some megacities and supercities compared with large and medium-sized cities.

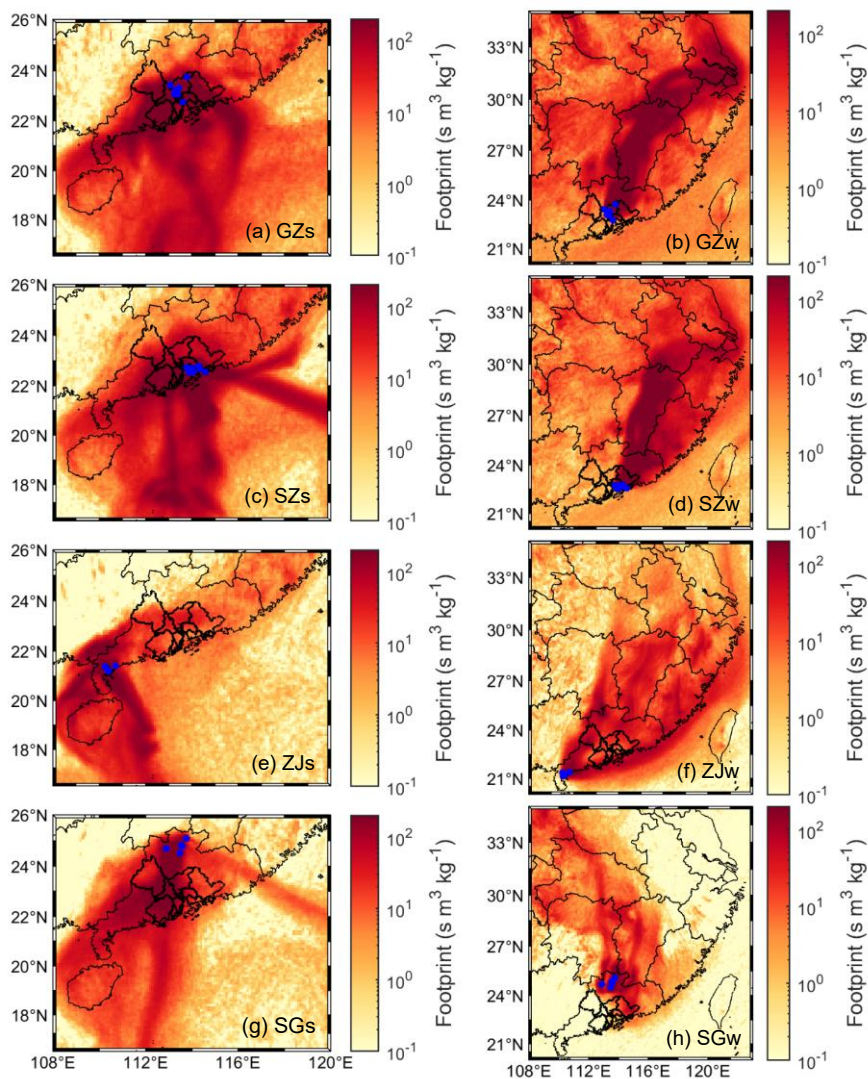
290 Noting that the  $C_{\text{ff}}/C_{\text{xs}}$  ratio is critically sensitive to background selection. Regional backgrounds (as implemented here) introduce  $C_{\text{bio}}$  contributions from surrounding rural/ agricultural sources to  $C_{\text{xs}}$ , whereas local urban backgrounds effectively isolate urban emissions by filtering out these external biogenic signals, thereby increasing the apparent  $C_{\text{ff}}$  fraction compared to regional background approaches. The consistent adoption of regional background methodologies across all studies in Table E1 ensures the comparative validity of the results, as they share a common framework for accounting for  $C_{\text{bio}}$  influences from peripheral non-urban sources. The derived annual  $C_{\text{ff}}$  averages are  $(15.3 \pm 5.2)$ ,  $(13.7 \pm 10.2)$ ,  $(10.0 \pm 5.2)$ , and  $(8.2 \pm 7.0) \mu\text{mol mol}^{-1}$  in Guangzhou, Shenzhen, Zhanjiang, and Shaoguan, respectively, based on the mass balance equations of  $\text{CO}_2$  and  $\Delta(^{14}\text{C})$ . These  $C_{\text{ff}}$  concentrations were low to moderate compared with those in other cities globally (Table E2, Fig. E1), despite the high emissions in Guangzhou and Shenzhen from inventories (Fig. 1).

### 300 3.3 Spatial distribution and seasonal variations

The spatial differences observed in  $C_{\text{ff}}$  primarily reflect the combined influence of emission intensity and atmospheric transport rather than direct emission magnitudes. We first identified potential source regions that are likely to contribute to the observed  $C_{\text{ff}}$  variability by analyzing its spatial distribution and seasonal variations. Higher  $C_{\text{ff}}$  levels were typically observed at densely populated downtown sites (GZ6 and GZ5; SG3 and SG2) in Guangzhou during summer (GZs) and Shaoguan during winter (SGw), forming an “urban  $C_{\text{ff}}$  dome” (Fig. 1c). This was further supported by significant positive correlations between the  $C_{\text{ff}}$  measurements and the corresponding  $1 \times 1$  km gridded ODIAC (Oda and Maksyutov, 2011; Oda and Maksyutov, 2024) inventory emissions in GZs ( $r = 0.53$ ,  $p = 0.1$ ), and a significant positive correlation in SGw ( $r = 0.91$ ,  $p = 0.03$ ). These correlations are used here as qualitative support and should be interpreted cautiously given uncertainties in the emission inventory (e.g., missing or spatially misallocated sources). The “urban  $C_{\text{ff}}$  dome” indicates that  $C_{\text{ff}}$  is mainly derived from the localized fossil fuel combustion, which is likely to be influenced by the urban topography. That is, downtown Guangzhou and downtown Shaoguan are surrounded by mountains to the east, north, and west. In contrast, we found that higher  $C_{\text{ff}}$  from western industrial areas and airport (SZ2) in Shenzhen during summer (SZs), and from port areas (ZJ5>ZJ2; ZJ2>ZJ3>ZJ4) in Zhanjiang during winter (ZJw) and summer (ZJs, by atmospheric transport) (Fig. 1ehg).

315 Atmospheric transmission of  $C_{\text{ff}}$  from potential source regions was observed at large spatial scales combined with air mass back trajectories by the Hybrid Single-Particle Lagrangian Integrated Trajectory (HYSPPLIT) model (Stein et al., 2015) and emission footprints by the FLEXPART dispersion model (Pisso et al., 2019). Shaoguan exhibited higher  $C_{\text{ff}}$  concentrations in summer  $((10.7 \pm 8.3) \mu\text{mol mol}^{-1})$  than in winter  $((5.8 \pm 4.4) \mu\text{mol mol}^{-1})$ . Trajectory and footprint analyses suggest that summer observations at Shaoguan were frequently influenced by air masses arriving from the Pearl River Delta (PRD) urban agglomeration, as illustrated by air mass back trajectories (HYSPPLIT, Fig. F1a; ) and emission footprints (FLEXPART, Fig. 3g), consistent with a larger upwind contribution under prevailing transport conditions. We note that the inference of “local versus non-local” contributions is

~~conditional on the completeness and spatial allocation of the emission inventories rather than high local emissions due to lower summer emissions from inventories.~~ In contrast, we found higher  $C_{\text{ff}}$  concentrations in winter compared with those in summer in Guangzhou ( $(17.7 \pm 3.5) > (12.9 \pm 5.6) \mu\text{mol mol}^{-1}$ ), Shenzhen ( $(18.0 \pm 9.9) > (9.2 \pm 8.5) \mu\text{mol mol}^{-1}$ ), and Zhanjiang ( $(12.1 \pm 5.1) > (7.6 \pm 4.3) \mu\text{mol mol}^{-1}$ ), consistent with the values in 14 other Chinese cities (Zhou et al., 2020). The higher winter concentrations ~~likely reflect a combination of (i) reduced ventilation found in Guangzhou, Shenzhen, and Zhanjiang in this study likely resulted from atmospheric trapping of emissions in the (e.g., a shallow planetary boundary layer), and (ii) higher local wintertime emissions, because suggested by ODIAC/(MEIC) indicates that (winter emissions were 8 %, 10 %, and 11 % [ODIAC] and 17 %, 22 %, and 14 % [MEIC]) higher than summer for Guangzhou, Shenzhen, and Zhanjiang, respectively, than those in summer (Oda and Maksyutov, 2024; Meic, 2023)), noting the associated inventory uncertainties. The atmospheric trapping of emissions is higher than local emissions during winter.~~ Within Guangzhou (GZw) and Shenzhen (SZw), ~~wintertime spatial gradients show which is supported by higher  $C_{\text{ff}}$  concentrations occurring in at downwind sites areas (GZ2, GZ6, and GZ10; SZ3 and SZ4) than at compared with upwind sites areas (GZ1 and GZ3; SZ8 and SZ9), suggesting an important role of transport/accumulation in shaping the observed enhancements.~~ The air mass back trajectories (HYSPLIT, Fig. F1b) and emission footprints (FLEXPART, Fig. 3bd) showed that the major source region was traced to the Yangtze River Delta (YRD) urban agglomeration in East China, and a portion from North China via long-range transport (Fig. F2ef). The major source region from the YRD was also reported in a study of CFC-11 in Shenzhen (Chen et al., 2024).



340

Figure 3: FLEXPART footprints simulating  $\text{Cr}$  emissions in summer (s) and winter (w) for (a and b, GZ) Guangzhou, (c and d, SZ) Shenzhen, (e and f, ZJ) Zhanjiang, and (g and h, SG) Shaoguan at heights from 0–100 m a.s.l. over a period of 30 days. Blue points

represent the locations of sampling sites. Black lines indicate the boundaries of continents (left), Chinese provinces (left, bold), and the nine cities of the PRD (right, bold) taken from Natural Earth (<https://www.naturalearthdata.com/>, last accessed: 9 March 2024).

### 3.4 Historical variations

#### 3.4.1 Meteorological typicality of the sampling months

As shown in Fig. G1, all five meteorological variables (10 m eastward wind, U10; 10 m northward wind, V10; 2 m air temperature, T2M; surface pressure, SP; and planetary boundary-layer height, PBLH) at all Guangzhou sites exhibit  $|z| \leq 1$ , indicating that both August and December 2022 were meteorologically typical relative to the same-year seasonal background and the 2010–2022 climatological baselines. At GZ7, December 2010 also shows  $|z| \leq 1$  relative to both the DJF 2010 seasonal mean and the 2010–2022 DJF climatology, indicating that the 2010 winter sampling month was likewise meteorologically typical (Fig. G1e–f). August 2022 featured slightly weaker easterly winds and near-climatological boundary-layer heights, while December 2022 was characterized by prevailing northerly flow and typical boundary-layer ventilation. Similarly, all five variables for December 2010 at GZ7 remained within  $\pm 1\sigma$  of both the DJF 2010 mean and the 2010–2022 DJF climatology, confirming that the 2010 winter sampling month was not associated with unusual circulation or mixing conditions.

Complementary ERA5 wind-rose analyses (Fig. G2) and 72 h HYSPLIT back-trajectory simulations (Fig. F1) confirm that both months followed the canonical East Asian monsoon regimes—maritime inflow during summer and continental outflow during winter. Using GZ7 as an illustrative example representative of central Guangzhou, the ERA5 wind roses show dominant east–east-southeasterly ( $90\text{--}135^\circ$ ) winds in August 2022, typically  $3\text{--}8\text{ m s}^{-1}$ . In comparison, JJA 2022 and the 2010–2021 JJA climatology peak in the south–south-westerly sector ( $157.5\text{--}225^\circ$ ), representing a within-sector rotation ( $90\text{--}225^\circ$ ) rather than a regime change. ERA5 anomalies of U10, V10, and PBLH remain below  $1\sigma$ , confirming transport typicality. HYSPLIT trajectories indicate that August 2022 air masses primarily originated over the South China Sea, consistent with summer maritime inflow. For December 2022, the ERA5 wind roses display a clear north–northeasterly ( $0\text{--}45^\circ$ ) dominance with  $3\text{--}8\text{ m s}^{-1}$  speeds. The DJF 2022 composite and the 2010–2021 DJF climatology show nearly identical northerly continental patterns, typical of the East Asian winter monsoon. HYSPLIT back trajectories confirm that the air parcels predominantly arrived from northern continental China under prevailing northerlies. Similarly, the ERA5 wind roses for December 2010 and DJF 2010 at GZ7 (Fig. G2g–h) show dominant northerly to north-easterly flow, closely matching the DJF climatological wind regime, indicating that the 2010 winter sampling period was also embedded in the canonical East Asian winter monsoon pattern.

To directly compare the meteorological environments of the two sampling years, we further analysed ERA5 diagnostics on flask sampling days at GZ7 (Tables G1–G2). Both December 2010 and December 2022 were dominated by northerly to north-easterly flow, with winds in the  $0\text{--}45^\circ$  sector accounting for 61.7 % and 82.7 % of occurrences, respectively (Table

G2). However, December 2022 exhibited stronger winds and deeper boundary layers than December 2010 (mean wind speed: 3.6 vs. 2.6 m s<sup>-1</sup>; mean PBLH: 476 vs. 377 m; mean ventilation: 2024.5 vs. 1258.0 m<sup>2</sup> s<sup>-1</sup>), and these differences are statistically significant ( $p < 0.01$  for both Student's t-test and Mann–Whitney U test; Table G1). These conditions would tend to dilute near-surface enhancements in 2022 relative to 2010, implying that the observed decreases in  $C_{\text{f}}$  and

$R_{\text{CO}_2/\text{CO}_2\text{ff}}$  between the two periods are, if anything, conservative with respect to emission changes.

Overall, these diagnostics suggest that the sampling windows in both 2010 and 2022 were not associated with anomalous large-scale transport. Nevertheless, variability in mixing and transport at sub-monthly scales may still contribute to uncertainty, especially given the limited number of winter flasks in 2022. Accordingly, we treat transport/mixing variability as an uncertainty in the inter-period comparison rather than assuming it to be negligible. These results demonstrate that both sampling periods were representative of their respective seasonal transport conditions. Consequently, atmospheric transport variability is unlikely to bias the reported  $C_{\text{f}}$  trend or the inferred changes in  $R_{\text{CO}_2/\text{CO}_2\text{ff}}$  ratios and fuel-type contributions.

#### 3.4.2 Representativeness of weekly flask samples

Each flask represents approximately 15–20 min of integrated air, and about 40 samples were collected per month across ten stations, providing broad spatial and temporal coverage. To evaluate how representative these discrete samples are for the respective seasons, we compared ERA5 diagnostics (PBLH, wind speed, and wind direction) during sampling days with the corresponding monthly means. The results show that meteorological conditions during sampling closely matched monthly climatological averages, confirming that no unusual stagnation or transport anomalies occurred on the sampling days. For the December 2010 flask sampling at GZ7, ERA5 diagnostics and wind roses (Fig. G1e–f and G2g–h) likewise show that sampling-day conditions were consistent with the DJF 2010 seasonal mean and the 2010–2022 DJF climatology, indicating that these earlier samples were also collected under typical winter transport regimes.

ERA5 wind roses (Fig. G2) and HYSPLIT 72-h back-trajectories (Fig. F1) further confirm that the flask collection periods coincided with the prevailing summer (90–225°) and winter (0–45°) monsoon sectors. Hence, the samples captured the dominant seasonal transport regimes rather than isolated short-term events. We therefore consider the weekly flask observations to be broadly representative of their seasonal backgrounds in terms of large-scale transport, while noting that the discrete nature of flask sampling (and the small winter 2022 sample size) limits the ability to fully average out synoptic-scale variability. This demonstrates that the weekly flask observations are meteorologically and dynamically representative of their respective seasonal backgrounds, minimizing the potential bias from short-term synoptic variability. Consequently, the derived  $C_{\text{f}}$  concentrations from these samples can be regarded as seasonally robust, and the subsequent interannual comparisons mainly reflect emission-driven rather than sampling-driven differences.

#### 3.4.3 Historical variation of $C_{\text{f}}$ concentrations

Because both August and December 2022 were meteorologically typical, the observed inter-annual differences in  $C_{\text{f}}$  are attributed mainly to emission rather than transport variability. To ensure comparability, all available historical datasets

(Table H1) were harmonized to identical sites, seasons, and local-time windows, and recalculated using unified background references (Table H2, Fig. 4a). This harmonization reduces methodological differences (e.g., background choice and sampling-window differences) and facilitates an inter-period comparison of  $C_{ff}$  mole fractions, while transport and mixing variability remains a source of uncertainty. These harmonized datasets minimize transport and spatial biases, allowing the remaining differences in  $C_{ff}$  mole fractions to be interpreted as primarily emission driven. We emphasize that the following comparison addresses observed near-surface  $C_{ff}$  concentrations. Without an atmospheric transport model and inverse modelling, we cannot quantitatively attribute the observed inter-period concentration differences to emission changes.

For Guangzhou, a site-specific long-term comparison was conducted at the GZ7 urban station, which was also used by Ding et al. (2013). In their study,  $C_{ff}$  was derived from flask observations collected around 20:00 LT (post-rush-hour) using a  $\Delta(^{14}C)$  background based on corn-leaf samples from Qinghai, Gansu, and Tibet. Such a background likely represents a different air-mass domain from Guangzhou. In contrast, the present study used atmospheric  $\Delta(^{14}C)$  observations from the NL regional background site, which directly samples the same regional air masses influencing Guangzhou. To harmonize the background reference used in the  $C_{ff}$  calculation between studies make the datasets directly comparable, the winter 2010  $C_{ff}$  values from Ding et al. (2013) and the winter 2022 values from this work were recalculated using the NL tree-ring  $\Delta(^{14}C)$  record (Li et al., 2025b) as a common background-reference baseline. The NL tree-ring  $\Delta(^{14}C)$  represents a growing-season (March–October) integrated proxy and the 2022 value is linearly extrapolated from the 2011–2020 record; it is therefore not intended to represent wintertime background variability and is used here only to provide an internally consistent baseline for inter-study comparison. This adjustment yields changes  $C_{ff}$  from  $45.6 \pm 5.3 \mu\text{mol mol}^{-1}$  to  $44.273 \pm 5.346.9 \mu\text{mol mol}^{-1}$  for 2010, and from  $16.8 \pm 3.4 \mu\text{mol mol}^{-1}$  to  $12.544.6 \pm 3.4 \mu\text{mol mol}^{-1}$  for 2022, indicating a pronounced reduction in fossil-fuel-derived  $\text{CO}_2$  over the decade.

Because sampling times differ (20:00 vs 14:00 LT), we quantified the expected diurnal  $C_{ff}$  contrast using continuous  $\text{CO}$  observations near GZ7.  $\Delta\text{CO}$  increased from 168 ppb at 14:00 to 221 ppb at 20:00, corresponding to a 21 %  $C_{ff}$  nighttime enhancement (Scheme 1, Appendix H1). A supplementary analysis using the winter 2023–2024 dataset gave a 35 % enhancement (Scheme 2, Appendix H1). These findings suggest that the evening  $C_{ff}$  level is typically 21–35 % higher than the well-mixed afternoon value due to weaker nocturnal boundary-layer mixing, although a diurnal cycle in emissions may also contribute to this difference. Applying this correction, the 2010 nighttime  $C_{ff}$  ( $44.273 \pm 5.346.9 \mu\text{mol mol}^{-1}$ ) corresponds to an afternoon-equivalent concentration between of  $\approx 2847.7 \pm 3.5 \mu\text{mol mol}^{-1}$  and  $34.924.6 \pm 4.2 \mu\text{mol mol}^{-1}$ , which remains substantially higher than the 2022 value of  $12.544.6 \pm 3.4 \mu\text{mol mol}^{-1}$ .

In addition to harmonizing background  $\Delta(^{14}C)$  and sampling times, we explicitly evaluated the impact of changes in boundary-layer mixing between 2010 and 2022 (Sect. 3.4.1, Table G1). To assess how much of the inter-period difference could plausibly be explained by changes in boundary-layer mixing, we provide a first-order estimate of the sensitivity of near-surface  $C_{ff}$  to PBLH variations. Under a well-mixed boundary-layer “box” approximation, the surface enhancement of predominantly surface-emitted tracers scales approximately as  $C_{ff} \propto 1/\text{PBLH}$ , implying  $\Delta C_{ff}/C_{ff} \approx -\Delta\text{PBLH}/\text{PBLH}$ . Using

ERA5 PBLH at the actual flask sampling hours (Fig. G1), the standardized anomaly of PBLH in Dec 2022 at Guangzhou sites is  $z \approx 0.17$ , corresponding to a relative PBLH increase of 11 % (based on the local winter mean and standard deviation used to define  $z$ ). If emissions and other factors were unchanged, this would translate into an expected dilution of  $C_{ff}$  by 11 % (i.e., 1–3  $\mu\text{mol mol}^{-1}$  for typical wintertime  $C_{ff}$  levels). This indicates that the modestly higher PBLH in Dec 2022 would tend to reduce the observed  $C_{ff}$ , but its magnitude is smaller than the observed inter-period difference (16.2–22.4  $\mu\text{mol mol}^{-1}$ ).

Taken together, even after harmonizing the  $\Delta(^{14}\text{C})$  background and accounting for sampling-time differences/bias, the observations indicate an indicative inter-period decrease in wintertime  $C_{ff}$  in Guangzhou declined by  $\approx 34$ –46 % between 2010 and 2022, confirming a genuine and statistically significant ( $p < 0.01$ ) decrease in fossil-fuel  $\text{CO}_2$ . Using the CO-based diurnal scaling (21–35% nighttime enhancement), the 2010 value corresponds to an afternoon-equivalent  $C_{ff}$  of 28.7–34.9  $\mu\text{mol mol}^{-1}$ , compared to  $12.5 \pm 3.4 \mu\text{mol mol}^{-1}$  in 2022 (i.e., 56–64 % lower; the range reflects uncertainty in the diurnal scaling). This percentage refers to the observed concentration change and may include a modest contribution from differences in boundary-layer mixing; our first-order PBLH-based scaling suggests that the Dec 2022 mixing anomaly would affect  $C_{ff}$  at the  $\sim 10$  % level (1–3  $\mu\text{mol mol}^{-1}$ ). Given the limited number of winter flasks in 2022, we performed a leave-one-out sensitivity test (Appendix H), which shows that the inferred 2010–2022 decrease remains negative for all subsets, although the magnitude varies. Accordingly, we interpret the Guangzhou 2010–2022 difference as an indicative inter-period change rather than a robustly quantified long-term trend. FLEXPART footprint analyses for 2010 and 2022 show similar source-sensitivity patterns centered on the Guangzhou urban core, supporting and confirming that GZ7 remains spatially representative of Guangzhou's urban influence domain in both periods.

Comparable harmonized analyses were performed for other Chinese cities (Tables H1 and H2; Fig. 4a). For Beijing, all measurements originate from the urban rooftop site of the Research Center for Eco-Environmental Sciences, Chinese Academy of Sciences (RCEES). The  $\Delta(^{14}\text{C})$  background used in Zhou et al. (2020) was based on Qixianling Mountain (QXL), whereas Wang et al. (2022b) adopted the Waliguan (WLG) background. All  $C_{ff}$  values were recalculated using WLG as a common reference background with the 2015 value from Niu et al. (2016). After this correction, the 2014–2016 winter  $C_{ff}$  value increases slightly from  $27.0 \pm 0.3 \mu\text{mol mol}^{-1}$  to  $27.6 \pm 0.3 \mu\text{mol mol}^{-1}$ , ensuring consistency across datasets. Relative to this harmonized baseline, the subsequent decline to  $19.7 \pm 22.0 \mu\text{mol mol}^{-1}$  by winter 2020 (Wang et al., 2022b) represents an approximate 29 % reduction ( $p < 0.05$ ). This trend is consistent with regional fossil-fuel  $\text{CO}_2$  emission reductions and corroborated by independent  $\Delta(^{14}\text{C})$  tree-ring records showing a peak near 2010 in Beijing (Niu et al., 2024).

For Xi'an, at the Institute of Earth Environment, Chinese Academy of Sciences (IEECAS) urban site,  $C_{ff}$  fell by 36 % from  $(40.1 \pm 3.8) \mu\text{mol mol}^{-1}$  in 2011–2013 to  $(25.7 \pm 1.1) \mu\text{mol mol}^{-1}$  in 2014–2016 ( $p < 0.001$ ) (Zhou et al., 2022). Suburban sites declined by  $\approx 12$  % from  $(23.5 \pm 6.5) \mu\text{mol mol}^{-1}$  in 2016 (Wang et al., 2018) to  $(13.1 \pm 10.9) \mu\text{mol mol}^{-1}$  in 2021–2022 (Liu et al., 2024) ( $p < 0.05$ ). These decreases are consistent with independent  $\Delta(^{14}\text{C})$  tree-ring records indicating emission peak near 2013 in Xi'an (Niu et al., 2024).

475 Overall, the harmonized, site-specific, and time-of-day-corrected comparisons demonstrate statistically significant reductions  
in fossil-fuel CO<sub>2</sub> across China's major urban centers. For Guangzhou particularly, the combined evidence—consistent  
background domain, typical meteorology, verified sampling representativeness, and quantified diurnal correction—provides  
strong support that the observed C<sub>ff</sub> decline reflects genuine decarbonization rather than artifacts of sampling or transport  
480 of South and East China (e.g., Hebei, Shandong, Zhejiang, and Guangdong; Fig. F2) according to the MEIC inventory (Shi  
et al., 2022), supporting the interpretation of a widespread decarbonization trend.

Similar reductions were found in C<sub>ff</sub> emissions from 2012 to 2020 according to the MEIC inventory (Shi et al., 2022), such  
as Guangzhou (by 16 % from 2011), Shenzhen (by 3 %), Zhanjiang (by 0.1 %), Beijing (by 16 %), and Xi'an (by 9 %) (Fig.  
485 4b), particularly in the industrial and power sectors (Li et al., 2017). We also found such declines in the MIXv2 Asian  
emission inventory (MIXv2, excluding Shenzhen and Shaoguan) (Li et al., 2024) and another carbon inventory for most  
Chinese cities (Zhang et al., 2024), but not in the ODIAC (Oda and Maksyutov, 2024) and the Emissions Database for  
Global Atmospheric Research (EDGAR) (Crippa et al., 2023). In fact, the mitigation of C<sub>ff</sub> emissions in China's MEIC  
inventory was primarily driven by heterogeneous trends across cities: 38 % exhibited sustained emission reductions, 29 %  
showed an initial decline followed by a rebound, while 33 % maintained increasing trajectories. Notably, cities achieving  
490 sustained reductions were disproportionately concentrated in larger cities, comprising 86 % of megacities, 43 % of  
supercities, and 43 % of Type I large cities (populations of 3–5 million). In contrast, smaller cities showed lower mitigation  
prevalence, with only 34 % of Type II large cities (1–3 million) and 38 % of medium/ small cities attaining emission  
decreases.

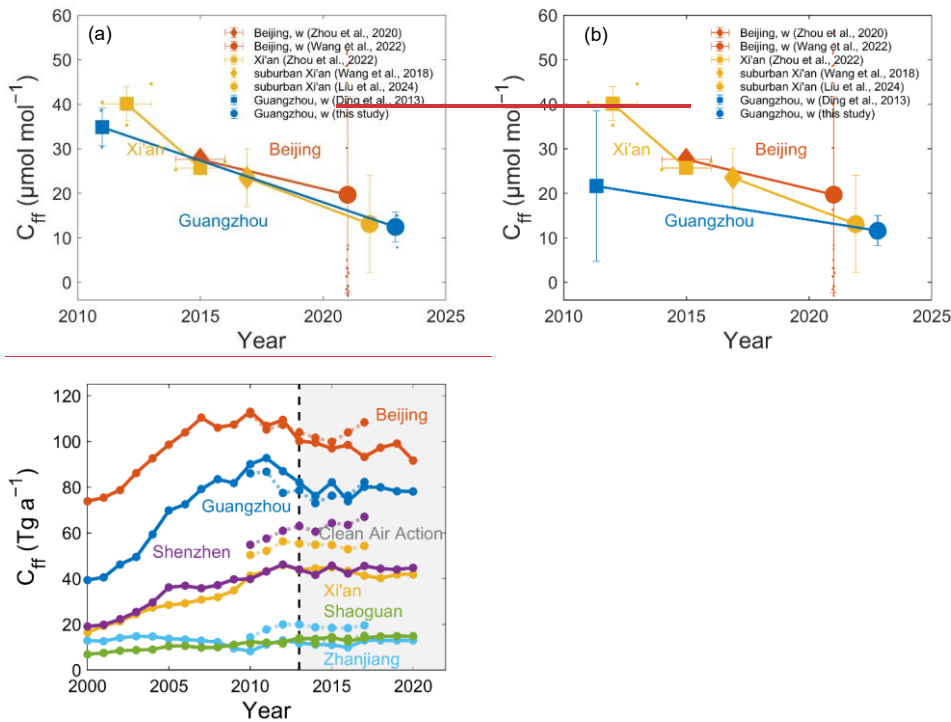


Figure 4: (a) Harmonized comparison of  $C_{ff}$  mole fractions at identical the same sites, and seasons, after applying consistent sampling times, and after correction to common background assumption conditions.  $C_{ff}$  concentrations are compiled from atmospheric measurements (Wang et al., 2022b; Zhou et al., 2022; Ding et al., 2013; Zhou et al., 2020; Wang et al., 2018) in Beijing, Xi'an, and Guangzhou. The large symbols indicate annual means, multiyear averages, or winter means (w) of the harmonized corrected  $C_{ff}$  values listed in Table H2, and the small symbols represent the corresponding individual scattered measurements.  $C_{ff}$  observations are calculated as enhancements over the regional background (Nanling for Guangzhou; and Waliguan for Beijing and Xi'an). For Guangzhou, the inter-study harmonization in Table H2 uses a common NL tree-ring  $\delta^{14}\text{C}$  reference baseline (growing-season integrated; extrapolated to 2022 from the 2011–2020 record; Li et al. (2025b)) to harmonize background definitions across studies (used for harmonization only, not as a winter background). The y-axis error bars indicate uncertainty, and the x-axis error bars represent the observed period. (b)  $C_{ff}$  emissions from the MEIC (solid lines) (Li et al., 2017; Meic, 2023; Zheng et al., 2018) and MIXv2 (dotted lines) (Li et al., 2024) inventories in Beijing, Xi'an, Guangzhou, Shenzhen, Zhanjiang, and Shaoguan since 2010. The vertical dashed line indicates the year 2013 when China's Clean Air Action Plan was implemented.

### 3.5 Driver factors

#### 3.5.1 Coal-to-gas transition

We first determined the coal, oil, and natural gas fractions of  $C_{ff}$  using the Keeling plot of  $\delta(^{13}C)$  and  $CO_2$  (i.e., scatter plot between  $\delta(^{13}C)$  and inverse of  $CO_2$  mole fractions) and the Bayesian mixing model (MixSIAR) (Stock et al., 2018) during winter 2022. The fractions in winter were  $(49 \pm 25) \%$ ,  $(29 \pm 22) \%$ , and  $(22 \pm 19) \%$ , respectively, for Guangzhou,  $(47 \pm 25) \%$ ,  $(29 \pm 21) \%$ , and  $(24 \pm 20) \%$  for Shenzhen,  $(43 \pm 24) \%$ ,  $(29 \pm 21) \%$ , and  $(28 \pm 21) \%$  for Zhanjiang, and  $(39 \pm 24) \%$ ,  $(34 \pm 23) \%$ , and  $(27 \pm 21) \%$  for Shaoguan (Table 11). Coal combustion was the largest contributor to  $C_{ff}$  emissions, followed in descending order by oil combustion and natural gas combustion. Compared with other cities around the world (Table 11), we found natural gas was the primary fuel type consumed in Paris (70 %) (Lopez et al., 2013) and Beijing [ $(55 \pm 9) \%$ ] (Wang et al., 2022b), whereas oil was the main fuel type consumed in Los Angeles ( $>50 \%$ ) (Djuricin et al., 2010; Newman et al., 2016). Coal remains the primary fossil fuel used in Xi'an [ $(72.6 \pm 10.4) \%$  in 2014 and  $(54 \pm 4) \%$  in 2019] (Wang et al., 2022b; Zhou et al., 2014), Guangzhou (49 % in 2022), and Shenzhen (47 % in 2022). Notably, cities with high  $C_{ff}$  emissions consume all three types of fossil fuels, with the dominant fuel type varying by city. Coal remains the primary fossil fuel used in many Chinese cities.

The reduction in  $C_{ff}$  concentrations can be attributed to changes in energy systems as a result of China's clean air measures (Shi et al., 2022). A major contribution has been the reduction in coal usage and the shift to low-carbon energy sources such as natural gas. During 2013–2022, the share of coal in the energy mix decreased by 4.9 % in China and by 7.1 % in Guangdong Province, whereas the share of natural gas increased by 3.0 % in China and by 7.2 % in Guangdong Province, according to the MEIC inventory (Li et al., 2017; Zheng et al., 2018; Meic, 2023; Xu et al., 2024). By applying the coal, oil, and natural gas fractions of  $C_{ff}$  derived from our measurements, it's likely that coal usage in Guangdong Province since 2013 have decreased  $\geq 21 \%$ , and natural gas usage have increased by  $\geq 16 \%$  (Fig. 5a). Similarly, in Guangzhou city, it's likely that coal usage since 2011 has decreased by 23 % instead of by 8.8 % (Fig. 5b), and natural gas usage has increased by 17 % instead of by 7.9 %, assuming that the fuel type fractions of  $C_{ff}$  in Guangzhou city were the same as those in Guangdong Province in the inventory.

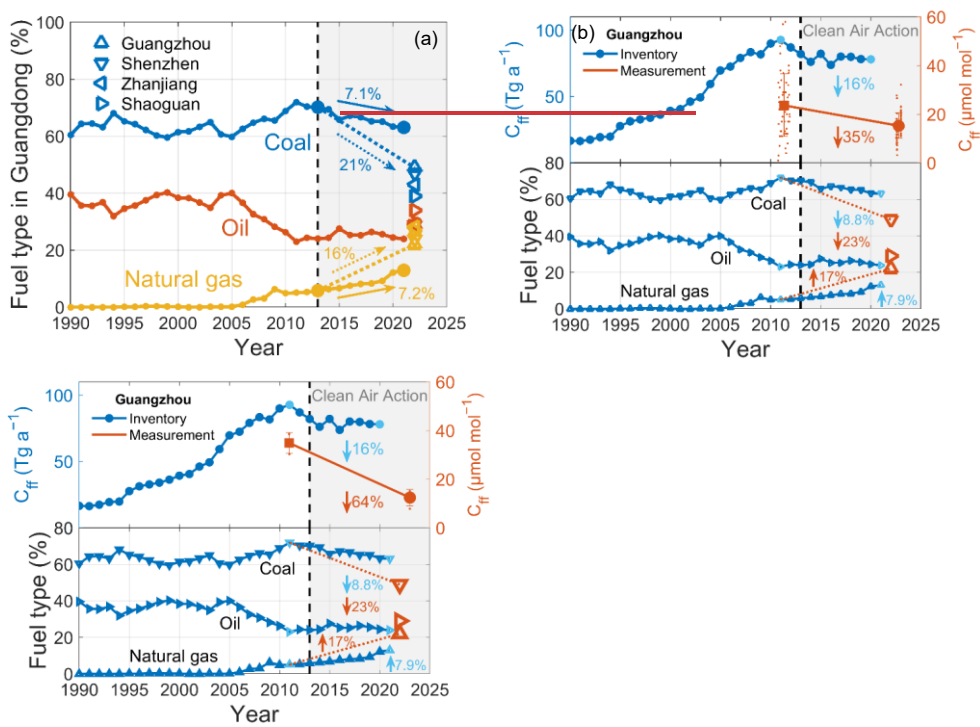


Figure 5: (a) Coal, oil, and natural gas fractions of  $C_{fr}$  in Guangdong Province from the MEIC inventory from 1990 to 2021 (points), and in the cities of Guangzhou, Shenzhen, Zhanjiang, and Shaoguan from measurements in this study in 2022 (triangles). (b) (Top) Comparison of reductions in  $C_{fr}$  inventory emissions (blue) and harmonized measured  $C_{fr}$  concentrations in Guangzhou (red; harmonized by applying consistent sampling-time and background assumptions) resulting from (Bottom) reduced coal usage and increased natural gas usage in Guangzhou. The vertical dashed line indicates the year 2013 when China's Clean Air Action Plan was implemented.

540

### 545 3.5.2 Combustion efficiency improvement

We first calculated  $R_{CO/CO_2fr}$  ratios at each measurement site and found higher ratios in summer than winter (Fig. J1). However, we focused only on observations in winter for four reasons. First, summer CO shows greater instability as its atmospheric lifetime depends on OH radical production, which is enhanced through photochemical reactions (e.g.,  $CH_4$  oxidation) under intense solar radiation, making CO a less reliable fossil fuel tracer (Rosendahl, 2022). Second, winter

550 exhibits stronger  $\Delta\text{CO}-C_{\text{ff}}$  correlations ( $r > 0.6$ ,  $p < 0.01$ ; Fig. J2) with better regional representativeness due to extended CO atmospheric lifetime from slower CO oxidation rates. Third, the winter  $\Delta\text{CO}-C_{\text{ff}}$  relationship better captures anthropogenic emission characteristics compared to other seasons. Fourth, weaker vertical mixing in winter accentuates local emission impacts (Wang et al., 2010). In addition, the lower  $C_{\text{ff}}$  signals observed in summer lead to higher uncertainty in the regression slope and thus greater uncertainty in the  $R_{\text{CO}/\text{CO}_{2\text{ff}}}$  ratios, as also noted in Maier et al. (2024), which can be seen in the larger error bars of the summer data in Fig. J2.

560 We then estimated winter 2022  $R_{\text{CO}/\text{CO}_{2\text{ff}}}$  ratios across Chinese cities using  $\Delta\text{CO}-C_{\text{ff}}$  regression slopes (Fig. J2), with spatial variations primarily attributed to differences in fuel composition and combustion efficiency (Graven et al., 2009). CO is generated through incomplete combustion of both fossil fuels and biomass. These spatial patterns are consistent with combustion characteristics showing biomass burning produces higher CO emissions per unit energy than fossil fuel combustion (Akagi et al., 2011). As shown in Fig. H4J1, suburban/rural sites (GZ1, SZ9, ZJ1, SG1) exhibited significantly higher ratios than urban sites (GZ5, SZ7, ZJ4, SG3): GZ1 > GZ5 ( $30.4 \pm 10.0$ ) > ( $19.8 \pm 4.6$ )  $\text{nmol } \mu\text{mol}^{-1}$ , SZ9 > SZ7 ( $41.3 \pm 23.0$ ) > ( $14.8 \pm 2.4$ )  $\text{nmol } \mu\text{mol}^{-1}$ , ZJ1 > ZJ4 ( $41.2 \pm 3.6$ ) > ( $11.9 \pm 6.4$ )  $\text{nmol } \mu\text{mol}^{-1}$ , and SG1 > SG3 ( $26.7 \pm 2.9$ ) > ( $15.1 \pm 3.6$ )  $\text{nmol } \mu\text{mol}^{-1}$ . This pattern is in agreement with previous studies attributing elevated ratios in non-urban areas to biomass burning contributions (Rosendahl, 2022). In contrast, megacities showed 35–40 % lower ratios (Guangzhou:  $13.3 \pm 3.1$   $\text{nmol } \mu\text{mol}^{-1}$ , Shenzhen:  $13.5 \pm 2.4$   $\text{nmol } \mu\text{mol}^{-1}$ ) compared to smaller cities (Zhanjiang:  $22.6 \pm 5.0$   $\text{nmol } \mu\text{mol}^{-1}$ , Shaoguan:  $21.7 \pm 6.4$   $\text{nmol } \mu\text{mol}^{-1}$ ;  $p < 0.01$ ; Fig. J2), suggest higher fossil fuel combustion efficiency and/or lower biomass burning inputs. Guangzhou's ratios are dominated by improved fossil fuel combustion efficiency due to having the highest biomass burning emissions among the four studied cities in the EDGAR2024 inventory, while Shenzhen's ratios are attributed to both factors with nearly negligible biomass contributions corresponding to its 2017 biomass boiler phase-out policy.

570 We retrieved historical  $R_{\text{CO}/\text{CO}_{2\text{ff}}}$  data from observations in China by estimation from  $\Delta(^{14}\text{C})$  measurements and correction from  $R_{\text{CO}/\text{CO}_2}$  (increased by 20 %) (Table J1), and  $I_{\text{CO}/\text{CO}_{2\text{ff}}}$  data from the MEIC, MIXv2, and EDGAR inventories (Fig. 6). Because the observational record consists of discrete campaigns, for the observations we assess changes using inter-period differences (rather than fitting a single 1998–2022 linear trend), and we test robustness by comparing the inferred change with the combined 1 $\sigma$  uncertainties (added in quadrature, using the reported vertical 1 $\sigma$  uncertainties for each period). Given the minor contribution of biomass burning (BB)-related CO emissions across all inventories, with  $I_{\text{CO}/\text{CO}_{2\text{ff}}}$  ratio below 0.003 (MEIC, incorporating OBBEIC data (Song et al., 2009; Huang et al., 2012)), less than 1.0 (MIXv2), and declining from 3.8 (1990) to 1.1 (2022) in EDGAR, we assume that interannual variability in BB emissions has negligible influence on the overall emission ratios. The compiled observations (1998–2022) and inventories (1990–2022) data show a sustained decline both indicate in China's  $R_{\text{CO}/\text{CO}_{2\text{ff}}}$  and  $I_{\text{CO}/\text{CO}_{2\text{ff}}}$  ratios over the past 30 years ratios tend to be lower in recent years than in earlier periods (Fig. 6a), consistent with demonstrating that efforts to improved fossil fuel combustion efficiency are effective (Wang et al., 2010; Lee et al., 2020), which is another factor contributing to the reduction in  $C_{\text{ff}}$  concentrations. The MEIC inventory attributes this trend to spatiotemporally heterogeneous mitigation pathways: 72 % of the cities started

585  $I_{\text{CO}/\text{CO}_2\text{ff}}$  reductions during 1990–1994, while the remaining 28 % (mainly concentrated in the western provinces) exhibited a  
delayed start until 1995–2004. The implementation of China’s clean air policies since 2013 has systematically phased out  
small, inefficient combustion facilities and replaced them with centralized, high efficient, and clean energy infrastructure  
(Shi et al., 2022). The phase-out of coal-fired industrial boilers during 2013–2020 reduced  $\text{CO}_2$  emissions by  $(1.5 \pm 0.3)$  Gt,  
accounting for 12 % of the national industrial emission reduction (Li, 2023). These technological transitions enhanced  
combustion efficiency by  $>10$  %, and reduced coal-dominated energy intensity by 40 % across the sector. The MEIC  
590 inventory showed that these synergistic measures resulted in significant energy savings, with a net reduction of 0.25  
gigatonnes of coal equivalent (Gtce) in 2020 and a cumulative reduction of 1.06 Gtce over the policy implementation period  
(Shi et al., 2022). Critically, the efficiency-driven transition decoupled energy demand from  $C_{\text{ff}}$  emissions, with combustion  
optimization directly reducing coal consumption 1–2 % and  $C_{\text{ff}}$  emissions by 1–3 Gt per year after 2015 (Le Quéré et al.,  
2016; Friedlingstein et al., 2023b).

595 We systematically compared observational  $R_{\text{CO}/\text{CO}_2\text{ff}}$  values with inventory  $I_{\text{CO}/\text{CO}_2\text{ff}}$  estimates. Our 2022 measurements of the  
 $R_{\text{CO}/\text{CO}_2\text{ff}}$  ratios in megacities (Guangzhou and Shenzhen) were consistent with EDGAR estimates ( $14.9 \text{ nmol } \mu\text{mol}^{-1}$ , 2022),  
while those in smaller cities (Zhanjiang and Shaoguan) were closer to MEIC values ( $19.2 \text{ nmol } \mu\text{mol}^{-1}$ , 2020) (Fig. 6a) and  
independent field measurements near Xi’an ( $23 \pm 6 \text{ nmol } \mu\text{mol}^{-1}$ , 2021) (Liu et al., 2024). City comparisons of observations  
against MEIC estimates revealed systematic deviations: Shenzhen’s observed ratio fell 42 % below inventory estimates ( $23.4$   
600  $\text{ nmol } \mu\text{mol}^{-1}$ ), whereas Shaoguan’s exceeded projections ( $12.7 \text{ nmol } \mu\text{mol}^{-1}$ ) by 71 %; Guangzhou’s and Zhanjiang’s  
are similar to inventory estimates ( $14.2$  and  $23.8 \text{ nmol } \mu\text{mol}^{-1}$ , respectively) (Fig. 6b). When a regional background site is used,  
however, the inferred  $R_{\text{CO}/\text{CO}_2\text{ff}}$  ratios may be influenced by emissions from outside the target city, so that the observed ratios  
represent a mixture of urban and regional emission signatures rather than a purely city-scale signal. This background effect  
may therefore contribute to some of the discrepancies between  $R_{\text{CO}/\text{CO}_2\text{ff}}$  and  $I_{\text{CO}/\text{CO}_2\text{ff}}$ .

605 The 24-yearthree-decade observational record of  $R_{\text{CO}/\text{CO}_2\text{ff}}$  ratios (1998–2022) are closer to (higher than) the MEIC estimates  
with a difference of  $(22 \pm 23)$  % compared with the MIXv2 and EDGAR estimates, when focusing on the ratios over time  
and ignoring the local deviations caused by the specific cities. These findings indicate that the MEIC inventory is more  
accurate than the EDGAR inventory for China. For specific cities, we found that the MEIC inventory estimates were  
deviated less from the observed  $R_{\text{CO}/\text{CO}_2\text{ff}}$  (based on  $\Delta^{14}\text{C}$  measurements) in recent years than the corrected  $R_{\text{CO}/\text{CO}_2\text{ff}}$  (using  
610  $R_{\text{CO}/\text{CO}_2}$ ) in earlier years for Beijing and Guangzhou (Fig. 6b). For example, in Beijing, the discrepancy in the ratios between  
observations and inventories decreased from 22 % in 2006–2007 ( $R_{\text{CO}/\text{CO}_2}$ -corrected) (Wang et al., 2010) to 8.7 % in 2009–  
2010 ( $\Delta^{14}\text{C}$ -derived) (Turnbull et al., 2011), and further declined to 7.0 % by 2014 ( $\Delta^{14}\text{C}$ -derived) (Niu et al., 2018).  
Similarly, in Guangzhou, the discrepancy dropped from 84 % in 2009–2010 ( $R_{\text{CO}/\text{CO}_2}$ -corrected) (Silva et al., 2013) to 34 %  
in 2014–2017 ( $R_{\text{CO}/\text{CO}_2}$ -corrected) (Mai et al., 2021), and eventually reached 6.4 % by 2022 ( $\Delta^{14}\text{C}$ -derived). These results  
615 suggest that  $R_{\text{CO}/\text{CO}_2}$  corrections should be carefully interpreted, as the effect of  $\text{CO}_2$  from non-fossil sources can significantly  
bias the results, even in megacities with high  $C_{\text{ff}}$  emissions. For example, human respiration could bias  $R_{\text{CO}/\text{CO}_2}$  low by about  
9 % at a rural site near Beijing (Wang et al., 2010; Turnbull et al., 2011).

620 Despite the relatively good agreement of ratios between observations ( $R_{\text{CO}/\text{CO}_2\text{ff}}$ ) and MEIC inventory ( $I_{\text{CO}/\text{CO}_2\text{ff}}$ ) at the national scale, observational data exhibited significantly greater  $R_{\text{CO}/\text{CO}_2\text{ff}}$  reduction rates than inventory estimates when examined at the city level. From observations (Fig. 6b), in Guangzhou,  $R_{\text{CO}/\text{CO}_2\text{ff}}$  decreased by 36 % from 35.8 nmol  $\mu\text{mol}^{-1}$  in 2009–2010 (Silva et al., 2013) to 23.8 nmol  $\mu\text{mol}^{-1}$  in winter of 2014–2017 (Mai et al., 2021) and by 63 % to 13.3 nmol  $\mu\text{mol}^{-1}$  in winter 2022 (partly reflecting seasonal differences, as the Silva et al. (2013) dataset included summer observations, and partly indicating reduced CO emissions relative to  $C_{\text{ff}}$  due to improved combustion efficiency); in Beijing,  $R_{\text{CO}/\text{CO}_2\text{ff}}$  decreased by 58 % from 72.3 nmol  $\mu\text{mol}^{-1}$  in 2004 (Han et al., 2009) to 30.4 nmol  $\mu\text{mol}^{-1}$  in 2014 (Niu et al., 2018); in 625 Xi'an,  $R_{\text{CO}/\text{CO}_2\text{ff}}$  decreased by 50 % from  $(46 \pm 13)$  nmol  $\mu\text{mol}^{-1}$  in 2016 (Wang et al., 2018) to  $(23 \pm 6)$  nmol  $\mu\text{mol}^{-1}$  in 2021 (Liu et al., 2024). The MEIC estimates for the above three cities decreased by 36 %, 52 %, and 21 %, respectively, over the same period. Larger reductions of the ratios were found from observations than those from the MEIC inventory (i.e., 63 % > 36 % for Guangzhou, 58 % > 52 % for Beijing, and 50 % > 21 % for Xi'an). This conclusion holds even after artificially biasing the  $R_{\text{CO}/\text{CO}_2\text{ff}}$  ratio downward by about 9 % to account for human respiration in Beijing (2004) and in Guangzhou 630 (2009–2010 and 2014–2017). These findings suggest that the MEIC inventory may insufficiently capture, or lag, the rapid improvement in combustion efficiency and energy structure transformation in China.

The ~~24-year~~~~three-decade~~ decline in China's  $R_{\text{CO}/\text{CO}_2\text{ff}}$  ratios (1998-2022) demonstrates both improved fossil fuel combustion efficiency and successful implementation of air pollution control policies i.e., the success of air pollution emission reduction efforts. Our observations reveal significantly greater urban  $R_{\text{CO}/\text{CO}_2\text{ff}}$  reductions than those estimated by the MEIC inventory, 635 indicating potential underestimation of CO emission reductions relative to  $C_{\text{ff}}$  mitigations in current inventories. This finding aligns with previous reports of inventory underestimates for real-world CO reductions. Mai et al. (2021) showed that the MEIC inventory may underestimate cumulative reductions from fleet turnover and catalytic converter upgrades, despite China's National V standards having achieved the  $\leq 1$  g  $\text{km}^{-1}$  CO emission limit since 2013. Together, these results imply that the MEIC inventory might systematically underestimate the actual effectiveness of clean air policies in reducing air 640 pollutant emissions.

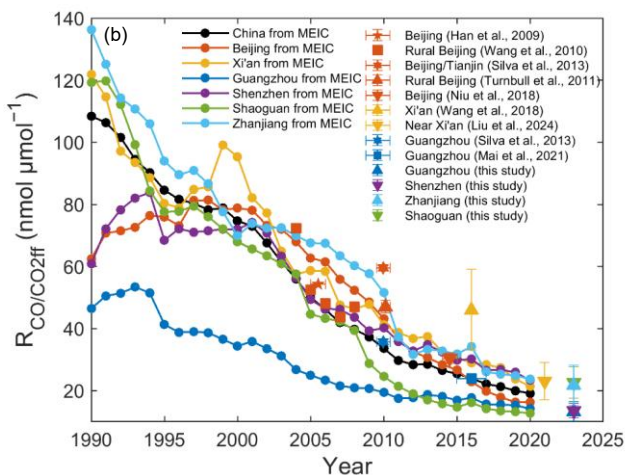
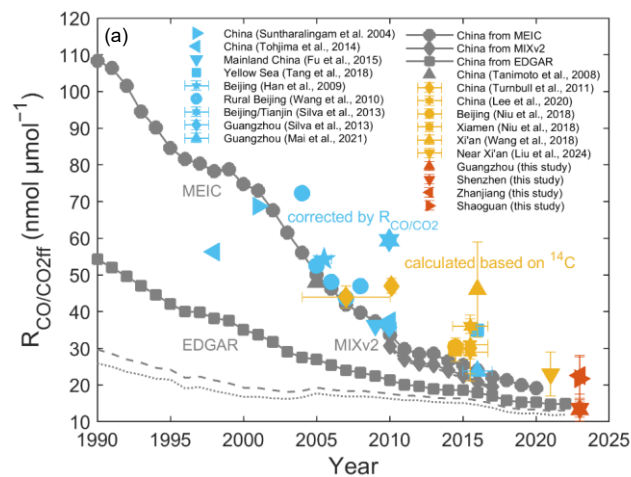


Figure 6:  $R_{CO/CO_2ff}$  for (a) China and for (b) Chinese cities obtained from inventories and observations (values refer to Table H1). For (a), the gray symbols represent data from the emission inventories (Tanimoto et al., 2008), including MEIC (Meic, 2023; Xu et al., 2024; Li et al., 2019; Li et al., 2017), MIXv2 (Li et al., 2024), and EDGAR2024 (Edgar, 2024). The  $I_{CO/CO_2ff}$  emission ratios

650 derived from the three inventories are shown with distinct approaches: (1) MEIC calculated the  $I_{CO/CO_{2f}}$  ratio for all anthropogenic sectors (represented by solid line with point symbols); (2) MIXv2 computed two variants: combining anthropogenic sectors with open biomass burning (solid line with diamond symbols) and anthropogenic-only emissions (dash-dotted line); while (3) EDGAR2024 provided three ratios: fossil + biogenic CO (solid line with square symbols), fossil + biomass burning CO (dashed line), and fossil-only CO (dotted line), all relative to  $C_{ff}$  emissions. The light blue symbols represent  $R_{CO/CO_{2f}}$  corrected by  $R_{CO/CO_2}$  from observational studies (Wang et al., 2010; Tohjima et al., 2014; Suntharalingam et al., 2004; Tang et al., 2018; Han et al., 2009; Fu et al., 2015), assuming that 20 % of the  $CO_2$  enhancement was from sources other than  $C_{ff}$ . The orange symbols represent  $R_{CO/CO_{2f}}$  calculated based on atmospheric  $^{14}CO_2$  measurements from previous studies (Turnbull et al., 2011; Niu et al., 2018; Lee et al., 2020; Wang et al., 2018; Liu et al., 2024). The red symbols depict the values observed in this study. For (b), the Chinese cities include Beijing, Xi'an, Guangzhou, Shenzhen, Zhanjiang, and Shaoguan from the MEIC inventory (filled circles) and observations from previous studies (Wang et al., 2018; Liu et al., 2024; Wang et al., 2010; Silva et al., 2013; Niu et al., 2018; Mai et al., 2021; Han et al., 2009; Turnbull et al., 2011) and this study since 1990. The up and down triangles represent  $R_{CO/CO_{2f}}$  estimated based on atmospheric  $\Delta(^{14}CO_2)$  measurements. Other symbols represent the  $R_{CO/CO_{2f}}$  corrected by  $R_{CO/CO_2}$  from observational studies, assuming that 20 % of the  $CO_2$  enhancement is from sources other than  $C_{ff}$ . The y-axis error bars indicate uncertainty, and the x-axis error bars represent the observed period. For observation-based  $R_{CO/CO_{2f}}$ , vertical error bars denote the uncertainty of the fitted  $\Delta CO-C_{ff}$  regression slope. Horizontal error bars indicate the time span of each observation period, and the symbol is plotted at the median time.

### 3.6 Implication

665 Since 2013, China has implemented a series of measures with the explicit aim of improving air quality. While the initial goal of China's clean air targets was to address air pollution, they also served as a powerful catalyst for the simultaneous transformation of energy systems and the mitigation of  $C_{ff}$  emissions. As a result, we have observed  $C_{ff}$  concentration and emission reductions in some Chinese megacities and supercities, such as Guangzhou, Beijing, and Xi'an. The achievement of peak emissions in Beijing (2010) and Xi'an (2013) marks a pivotal transition for China, signaling that cities across the nation, from megacities to small cities, are gradually reaching their emission peaks. This milestone has profound implications for both China's sustainable development and global climate governance, as China has dominated the global trend since 2010 (Friedlingstein et al., 2023a).

675 Despite China's remarkable success in reducing  $C_{ff}$  emissions, continued efforts are needed to optimize the nation's energy system and economic structure in order to facilitate future green growth. It is imperative that common solutions to climate change and air pollution are formulated and implemented with urgency, as China has set a goal for all cities to meet current air quality standards by 2035 and has pledged to achieve carbon peak by 2030 and carbon neutrality by 2060. One available solution is to control the common key sources and dominant source regions of air pollution and  $CO_2$  emissions (Wu et al., 2022; Zheng et al., 2024). In future policymaking, it is essential to adopt a co-beneficiary strategy that co-ordinates clean air measures and addresses climate change measures. This strategy, together with the associated assessment approach, will be an essential part of achieving sustainable development.

#### 4 Conclusions and outlook

This study advances the understanding of urban  $C_{ff}$  concentration changes in China through three key contributions. First, we ~~provide a comprehensive error analysis framework for  $C_{ff}$  estimation, including contributions from air–sea exchange, nuclear facilities, and particularly pioneer the integration of biomass burning emissions into  $C_{ff}$  estimation frameworks, significantly improving methodological accuracy.~~ Second, we identify ~~inter-period decreases in observed~~ substantial  $C_{ff}$  ~~concentrations~~ reductions in cities and their source regions, ~~which are consistent with~~ driven by coal-to-gas transitions (evidenced by stable isotope analysis) and combustion efficiency improvements (~~supported~~ confirmed by declining  $R_{CO/CO2ff}$  ratios), where megacities and supercities lead this decline. Finally, through systematic analysis of long-term  $R_{CO/CO2ff}$  trends, we reveal current emission inventories may underestimate combustion efficiency gains and CO emission reductions relative to  $C_{ff}$  mitigations. These findings provide critical support for refining emission accounting systems and developing evidence-based climate policies. The integrated approach offers new insights into urban emission dynamics and mitigation effectiveness.

This study has some limitations in sampling and source attribution. First, current sampling only covers summer and winter; future work should include all seasons to better capture annual trends. Second, the  $\delta(^{13}C)$ -based source partitioning is associated with large uncertainties—on the order of tens of percent—due to the limited isotopic separation among  $CO_2$  sources and the poorly constrained biogenic endmember. Similar uncertainty ranges have been reported in previous urban studies (see Table I1). Therefore, the  $\delta(^{13}C)$  partitioning results presented here should be considered as a preliminary, first-order estimate. Direct measurements of source-specific isotopic values would help refine the analysis.

In future work, a detailed quantitative analysis linking  $C_{ff}$  to emission distributions using FLEXPART footprints will be conducted to provide a more rigorous connection between observations and emission sources. Additionally, future studies should explicitly consider seasonally varying background references, ideally including coastal or marine background sites to better represent summer air masses. Furthermore, upcoming efforts could incorporate atmospheric modelling and inversion methods to improve emission estimates. This would require high resolution prior flux data and validation against direct measurements (e.g., radiocarbon analysis). Addressing these gaps would enhance source apportionment accuracy and enable a more robust integration of top-down (e.g., inversions) and bottom-up (e.g., inventories) approaches for evaluating urban emission mitigation strategies.

**Appendix A: Seasonal averages and quality control of  $\Delta^{14}\text{C}$  and  $\delta^{13}\text{C}$  measurements**

710 **Table A1**  $\Delta^{14}\text{C}$  and  $\delta^{13}\text{C}$  averages and standard deviations ( $n=4$  for each value) at 30 sampling sites

| City      | Site code  | Summer                    |                           | Winter                    |                           | Altitude (m a.s.l.) | Elevation (m a.g.l.) | Site description                                 |
|-----------|------------|---------------------------|---------------------------|---------------------------|---------------------------|---------------------|----------------------|--|
|           |            | $\Delta^{14}\text{C}$ (‰) | $\delta^{13}\text{C}$ (‰) | $\Delta^{14}\text{C}$ (‰) | $\delta^{13}\text{C}$ (‰) |                     |                      |  |
| Guangzhou | GZ1        | $-23.8 \pm 9.8$           | $-9.0 \pm 0.7$            | $-46.0 \pm 8.1$           | $-8.9 \pm 0.2$            | 212                 | 25                   | Suburban rooftops                                |
|           | GZ2        | $-30.2 \pm 4.7$           | $-9.0 \pm 0.3$            | $-56.8 \pm 5.6$           | $-8.9 \pm 0.3$            | 19                  | 20                   | Suburban rooftops                                |
|           | GZ3        | $-24.9 \pm 8.8$           | $-8.7 \pm 0.3$            | $-46.5 \pm 3.9$           | $-8.7 \pm 0.2$            | 120                 | 30                   | Suburban rooftops                                |
|           | GZ4        | $-24.6 \pm 4.8$           | $-9.0 \pm 0.7$            | $-49.7 \pm 9.3$           | $-9.0 \pm 0.3$            | 23                  | 35                   | Urban rooftops                                   |
|           | GZ5        | $-42.6 \pm 12.2$          | $-9.6 \pm 0.8$            | $-48.0 \pm 8.3$           | $-8.5 \pm 0.3$            | 46                  | 35                   | Urban rooftops                                   |
|           | GZ6        | $-42.1 \pm 16.7$          | $-9.5 \pm 1.0$            | $-52.8 \pm 11.2$          | $-8.9 \pm 0.1$            | 53                  | 60                   | Urban rooftops                                   |
|           | GZ7        | $-25.5 \pm 5.0$           | $-8.8 \pm 0.4$            | $-48.1 \pm 7.3$           | $-8.9 \pm 0.3$            | 120/ 75             | 118/ 40              | Urban tower/<br>Urban rooftops                   |
|           | GZ8        | $-32.8 \pm 9.4$           | $-9.4 \pm 0.5$            | $-49.6 \pm 8.1$           | $-9.2 \pm 0.2$            | 12                  | 30                   | Urban rooftops                                   |
|           | GZ9        | $-35.8 \pm 5.4$           | $-9.8 \pm 0.4$            | $-51.1 \pm 6.9$           | $-8.7 \pm 0.3$            | 50                  | 30                   | Urban rooftops                                   |
|           | GZ10       | $-34.8 \pm 19.8$          | $-9.5 \pm 0.9$            | $-51.2 \pm 5.9$           | $-9.0 \pm 0.2$            | 54                  | 40                   | Suburban rooftops                                |
| Shenzhen  | SZ1        | $-23.4 \pm 18.0$          | $-8.6 \pm 0.5$            | $-46.3 \pm 27.0$          | $-9.2 \pm 0.2$            | 40                  | 30                   | Suburban tower                                   |
|           | SZ2        | $-63.4 \pm 3.9$           | $-9.1 \pm 0.4$            | $-51.9 \pm 8.9$           | $-9.4 \pm 0.1$            | 28                  | 15                   | Rooftops in Industrial<br>area                   |
|           | SZ3        | $-20.8 \pm 22.5$          | $-8.7 \pm 0.5$            | $-56.3 \pm 16.1$          | $-9.4 \pm 0.3$            | 14                  | 15                   | Urban rooftops                                   |
|           | SZ4        | $-23.7 \pm 27.8$          | $-8.8 \pm 0.6$            | $-53.7 \pm 15.2$          | $-9.5 \pm 0.3$            | 42                  | 40                   | Urban campus rooftops                            |
|           | SZ5        | $-26.4 \pm 17.5$          | $-8.8 \pm 0.3$            | $-50.5 \pm 12.4$          | $-9.4 \pm 0.3$            | 40                  | 30                   | Urban campus rooftops                            |
|           | SZ6        | $-25.8 \pm 10.3$          | $-8.7 \pm 0.5$            | $-51.4 \pm 31.9$          | $-9.1 \pm 0.4$            | 60                  | 30                   | Suburban tower                                   |
|           | SZ7        | $-19.8 \pm 6.1$           | $-8.8 \pm 0.1$            | $-48.6 \pm 33.2$          | $-9.3 \pm 0.6$            | 210                 | 200                  | Urban rooftops                                   |
|           | SZ8        | $-18.4 \pm 12.7$          | $-8.6 \pm 0.5$            | $-43.8 \pm 31.7$          | $-9.0 \pm 0.3$            | 150                 | 110                  | Suburban rooftops at the<br>boundary site        |
|           | SZ9        | $-13.1 \pm 11.4$          | $-8.5 \pm 0.4$            | $-45.1 \pm 32.0$          | $-9.2 \pm 0.3$            | 60                  | 30                   | Suburban tower                                   |
|           | SZ10       | $6.8 \pm 1.9$             | $-9.0 \pm 0.6$            | $-52.8 \pm 7.7$           | $-9.4 \pm 0.2$            | 60                  | 20                   | Suburban rooftops                                |
| Zhanjiang | ZJ1        | $-19.1 \pm 9.4$           | $-10.2 \pm 0.5$           | $-35.7 \pm 12.9$          | $-9.1 \pm 0.4$            | 8                   | 20                   | Rural rooftops                                   |
|           | ZJ2        | $-23.5 \pm 14.6$          | $-9.4 \pm 0.6$            | $-35.5 \pm 12.6$          | $-9.0 \pm 0.2$            | 24                  | 40                   | Urban rooftops                                   |
|           | ZJ3        | $-18.4 \pm 4.8$           | $-10.2 \pm 0.6$           | $-37.0 \pm 12.7$          | $-9.1 \pm 0.1$            | 44                  | 40                   | Urban rooftops                                   |
|           | ZJ4        | $-14.2 \pm 7.0$           | $-8.9 \pm 0.3$            | $-38.7 \pm 12.3$          | $-9.1 \pm 0.2$            | 25                  | 40                   | Urban rooftops                                   |
|           | ZJ5        | $-18.0 \pm 13.1$          | $-9.1 \pm 0.5$            | $-40.3 \pm 11.7$          | $-9.4 \pm 0.4$            | 41/ 46              | 50/ 30               | Suburban campus site/<br>Site near the port area |
| Shaoguan  | SG1        | $-28.3 \pm 15.1$          | $-8.9 \pm 0.3$            | $-20.3 \pm 5.1$           | $-9.0 \pm 0.1$            | 114                 | 30                   | Suburban rooftops                                |
|           | SG2        | $-29.2 \pm 15.0$          | $-9.5 \pm 0.3$            | $-28.2 \pm 3.8$           | $-8.9 \pm 0.2$            | 60                  | 40                   | Urban campus rooftops                            |
|           | SG3        | $-26.5 \pm 17.3$          | $-9.2 \pm 0.5$            | $-35.0 \pm 10.3$          | $-9.0 \pm 0.2$            | 68                  | 40                   | Urban rooftops                                   |
|           | SG4        | $-43.6 \pm 20.8$          | $-9.0 \pm 0.2$            | $-19.7 \pm 6.2$           | $-8.8 \pm 0.2$            | 95                  | 30                   | Rural site                                       |
|           | SG5/<br>NL | $-3.7 \pm 1.3$            | $-9.2 \pm 0.2$            | $-10.9 \pm 0.8$           | $-9.3 \pm 0.2$            | 1700                | 15                   | Rooftops at the<br>background site               |

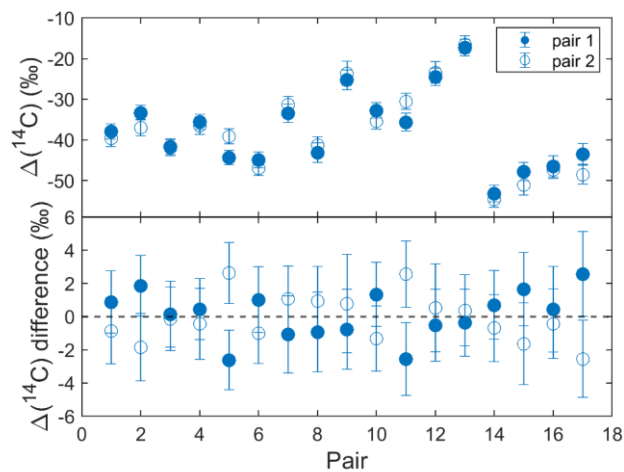


**Figure A1** Pair differences of  $\Delta(^{14}\text{C})$  for replicate measurements. Replicates were obtained from parallel air samples. The difference of each individual measurement from its pair mean is shown. Closed and open symbols are the first and second group taken from each pair, respectively. Error bars are the 1-sigma uncertainty on each measurement.

### Appendix B: Radiocarbon isotope endmembers for biomass burning

Atmospheric  $^{14}\text{CO}_2$  is assimilated by plants via photosynthesis, imprinting atmospheric  $\Delta(^{14}\text{CO}_2)$  signatures into plant tissues. This creates a bidirectional link: plant  $\Delta(^{14}\text{C})$  reflects atmospheric  $\Delta(^{14}\text{CO}_2)$  levels, while atmospheric  $\Delta(^{14}\text{CO}_2)$  dynamics can be inferred from plant biomass archives (e.g., tree-rings). Annual biomass  $\Delta(^{14}\text{C})$  closely matches contemporaneous atmospheric  $\Delta(^{14}\text{CO}_2)$  (due to rapid carbon turnover within a single growing season). Multi-year biomass  $\Delta(^{14}\text{C})$  represents an integrated signal, blending atmospheric  $\Delta(^{14}\text{CO}_2)$  variations over its growth period (e.g., tree-rings capture annual  $\Delta(^{14}\text{CO}_2)$  fluctuations).

**B1 Annual biomass.** The  $\Delta(^{14}\text{C})$  for annual biomass ( $\Delta_a$ ) in 2022 was estimated as  $-14.8 \pm 2.2$  ‰ (mean  $\pm$  MSE), derived from a linear regression model of atmospheric  $\Delta(^{14}\text{CO}_2)$  decline ( $-4.4$  ‰  $\text{a}^{-1}$ ) observed in Northern Hemisphere zone 3 between 2010 and 2018 (Hua et al., 2021).

**B2 Multi-year biomass.** The  $\Delta(^{14}\text{C})$  for multi-year biomass ( $\Delta_m$ ) is related with its age; the year it was growing, the annual increase in biomass, and atmospheric  $^{14}\text{CO}_2$  during its growth cycle. The  $\Delta(^{14}\text{C})$  for multi-year biomass can be determined

(Lewis et al., 2004):

$$\Delta^{14}C_m = \frac{\int_{t_1}^{t_2} \Delta^{14}C(t)w(t)dt}{\int_{t_1}^{t_2} w(t)dt} \quad (B1)$$

where  $\Delta^{14}C(t)$  is the atmospheric  $\Delta(^{14}CO_2)$  at age  $t$ , and the weighting function  $w(t)$  is the growth rate of carbon in biomass at age  $t$ , which can be determined by the Chapman-Richards growth model (Lewis et al., 2004):

$$V = A(1 - e^{-\frac{t-t_0}{\tau}})^m \quad (B2)$$

$$735 \quad w(t) = \frac{dV}{dt} \quad (B3)$$

where  $V$  is the volume of a tree at age  $t$  ( $V = 0$  at  $t = t_0$ ), and the parameters  $A$ ,  $\tau$ , and  $m$  can be chosen empirically to fit measured tree growth characteristics. The Chapman-Richards growth model describes cumulative growth of  $V$ .

It is assumed that the multi-year biomass was partitioned into five age cohorts (10-, 20-, 40-, 65-, and 85-year-old trees) with relative share of  $20 \pm 10\%$ ,  $20 \pm 10\%$ ,  $40 \pm 20\%$ ,  $10 \pm 5\%$  and  $10 \pm 5\%$ , respectively (Mohn et al., 2008). The corresponding  $\Delta(^{14}C)$  values were calculated as  $20.9 \pm 5.4\%$ ,  $52.9 \pm 4.0\%$ ,  $137.5 \pm 35.1\%$ ,  $261.2 \pm 50.4\%$ , and  $203.1 \pm 17.4\%$ , respectively. Consequently, the  $\Delta(^{14}C)$  signature of the multi-year biomass for the year 2022 was estimated as  $116.2 \pm 17.6\%$  (mean  $\pm 1\sigma$ ;  $\Delta_m$ ) using the Chapman-Richards growth model ( $\tau = 50$ ,  $m = 3$ ) and long-term tree-ring  $\Delta(^{14}C)$  measurements (Hua et al., 2021).

**B3 Biomass burning.** The  $\Delta(^{14}C)$  endmember for biomass burning ( $\Delta_{BB}$ ) was calculated using the two biomass types:

$$745 \quad \Delta_{BB} = f_a \cdot \Delta_a + (1 - f_a) \cdot \Delta_m \quad (B4)$$

where  $\Delta_a$  and  $\Delta_m$  represent the  $\Delta(^{14}C)$  signatures of annual biomass (e.g., crop residues) and multi-year biomass (e.g., woody waste), respectively, and  $f_a$  is the annual biomass fraction.

Using this framework, we estimated the 2022  $\Delta(^{14}C)$  endmembers for biomass burning as  $116.2 \pm 17.6\%$ ,  $103.1 \pm 15.8\%$ ,  $90.0 \pm 14.1\%$ ,  $76.9 \pm 12.3\%$ ,  $63.8 \pm 10.6\%$ , and  $50.7 \pm 8.9\%$  for  $f_a$  values of 0%, 10%, 20%, 30%, 40%, 50%, respectively.

## Appendix C: Bias correction for $C_{ff}$ calculation

**C1 Air-sea exchange.** The potential influence of  $CO_2$  outgassing from the adjacent South China Sea (SCS) on our onshore measurements was assessed. Although the SCS is a net source of  $CO_2$  to the atmosphere (with an annual flux of  $0.44 \text{ mol m}^{-2} \text{ yr}^{-1}$  (Li et al., 2020)), its influence is negligible. This conclusion is supported by an analogous study of the California coast: the high-resolution WRF-STILT simulation by Graven et al. (2018) was conducted using flux data that included intense local nearshore sources (with fluxes up to  $1.11 \text{ mol m}^{-2} \text{ yr}^{-1}$  (Turi et al., 2014)). Their results demonstrated that even these potent sources altered onshore  $CO_2$  concentrations by less than 0.001 ppm (Graven et al., 2018). Given that the regional net flux from the SCS is weaker than this analogue, we conclude its impact on our  $\Delta(^{14}CO_2)$  measurements and derived  $C_{ff}$  estimates is physically insignificant and within the measurement uncertainty.

760 **C2 Nuclear facilities.** All operational (Daya Bay, Ling'ao, Yangjiang, Taishan) and under-construction (Lufeng, Taipingling, Lianjiang) nuclear power plants (NPPs) along the Guangdong Province coastline (Table C1) employ pressurized water reactor (PWR) technology. Airborne  $^{14}\text{C}$  releases from these facilities are predominantly hydrocarbons (75–95 %), mainly  $\text{CH}_4$ , with only a small fraction emitted as  $\text{CO}_2$  (Iaea, 2004). In fact, almost all commercial reactors in China (> 95 %) are of the PWR type, which exhibits the lowest  $^{14}\text{CO}_2$  emission factor among nuclear technologies (Graven and Gruber, 2011; Yang, 2024).

765 Graven and Gruber (2011) reported that most of China and the western US are regions with minimal potential bias in  $^{14}\text{CO}_2$ -based  $C_{\text{ff}}$  estimates, owing to strong fossil fuel signals and limited nuclear  $^{14}\text{C}$  influence. Consistently, Graven et al. (2018) simulated the impact of reactor emissions on atmospheric  $\Delta^{14}\text{CO}_2$  using WRF-STILT and found that an average  $^{14}\text{CO}_2$  release rate of  $6.6 \text{ Ci yr}^{-1}$  ( $\sim 0.24 \text{ TBq yr}^{-1}$ ) from the Diablo Canyon NPP in California produced an effect of < 0.1 ppm in inferred  $C_{\text{ff}}$  at all sites, confirming that nuclear  $^{14}\text{C}$  emissions have a negligible influence on atmospheric radiocarbon measurements.

770 In Guangdong Province, Zazzeri et al. (2018) estimated  $^{14}\text{CO}_2$  emissions from the Daya Bay, Ling'ao, and Yangjiang NPPs to be 0.111, 0.233, and 0.166  $\text{TBq yr}^{-1}$ , respectively, values comparable to or smaller than those reported for Diablo Canyon. Although Daya Bay and Ling'ao are located only 6–7 km from the nearest observation sites (SZ10-and-SZ9) (Table C1), their emission rates remain extremely low. Under prevailing southeasterly winds in summer and northeasterly winds in winter, dispersion within the coastal boundary layer further dilutes any potential  $^{14}\text{CO}_2$  plumes before they reach the sampling locations.

775 Based on Gaussian plume scaling and regional wind climatology, we estimate that even under typical plume condition, the contribution of local reactor  $^{14}\text{CO}_2$  to measured  $\Delta^{14}\text{CO}_2$  at these urban sites would be < 0.1 %, corresponding to an effect on inferred  $C_{\text{ff}}$  below 0.05 ppm. This estimate can be regarded as an upper bound for potential nuclear contamination at our sites, because all NPPs that could influence Guangzhou are located at distances >100 km from the Guangzhou observation site (Table C1).

780 Therefore, even for the closest stations, the impact of nearby nuclear facilities on  $\Delta^{14}\text{CO}_2$  measurements is considered negligible and does not affect our radiocarbon-based source partitioning. For Guangzhou in particular, any nuclear influence on individual flask samples, and thus on the derived  $C_{\text{ff}}$  trend, is expected to be even smaller than this upper bound and negligible compared to other sources of uncertainty.

785 **Table C1** Summary of operational nuclear facility in Guangdong Province: installed capacity, operational period,  $^{14}\text{CO}_2$  emissions, and proximity to sampling sites with dominant wind directions.

| Nuclear facility | Installed electric capacity <sup>a</sup> (MWe) | Operation period <sup>b</sup>   | $^{14}\text{CO}_2$ emissions in 2016 <sup>c</sup> ( $\text{TBq yr}^{-1}$ ) | Closest site | Distance (km) | Dominant wind direction |
|------------------|--|---------------------------------|--|--------------|---------------|-------------------------|
| Daya Bay 1-2     | 984/984  | 1994/1994-present               | 0.111  | SZ10/<br>SZ9 | 6/<br>22      | SE (Summer)             |
| Ling'ao 1-4      | 990/990/<br>1086/1086                          | 2022/2003/<br>2010/2011-present | 0.233  | SZ10/<br>SZ9 | 7/<br>22      | NE (Winter)             |

|               |                                   |   |                   |                      |                     |  |
|---------------|-----------------------------------|---|-------------------|----------------------|---------------------|--|
| Yangjiang 1-6 | 1086/1086/1086/<br>1086/1086/1086 | 2014/2015/2016/<br>2017/2018/2019-<br>present | 0.166/<br>unknown | ZJ1/<br>GZ10/<br>SZ3 | 164/<br>182/<br>191 |  |
| Taishan 1-2   | 1750/1750                         | 2018/2019-present                             | unknown           | GZ10/<br>SZ3/<br>ZJ1 | 114/<br>116/<br>242 |  |

<sup>a</sup> Data from China Nuclear Energy Association, *Operational Performance of Nuclear Power in China (January-December 2024)* (in Chinese). Retrieved from: <https://www.china-nea.cn/site/content/48480.html> (last access: 18 October 2025). <sup>b</sup> Data from National Nuclear Safety Administration, *The Status of Mainland China's Nuclear Power Units in 2024* (in Chinese). Retrieved from: [https://nnsa.mee.gov.cn/ywdt/hyzz/202501/t20250107\\_1100142.html](https://nnsa.mee.gov.cn/ywdt/hyzz/202501/t20250107_1100142.html) (last access: 18 October 2025). <sup>c</sup> Emission data from Zazzeri et al. (2018), estimated using emission factors multiplied by IAEA PRIS data, assuming 28 % of <sup>14</sup>C released from PWRs is in the form of CO<sub>2</sub>.

**C3 Biospheric exchange.** Biospheric carbon fluxes associated with photosynthesis, autotrophic respiration, and annual biomass burning generally do not alter atmospheric  $\Delta(^{14}\text{C})$  levels, as the carbon exchanged through these processes largely maintains isotopic equilibrium with contemporary atmospheric CO<sub>2</sub> (Turnbull et al., 2009). In contrast, heterotrophic respiration and multi-year biomass burning (e.g., wildfire consuming legacy organic matter) release carbon fixed during periods of elevated atmospheric  $\Delta(^{14}\text{C})$ , such as the 1960s nuclear bomb testing peak. This temporal decoupling between carbon uptake and release introduces a measurable positive bias in modern  $\Delta(^{14}\text{C})$ , reflecting the delayed contribution of older carbon pools. Therefore, we use estimates of heterotrophic respiration (Rh) and biomass burning (BB) fluxes to correct for biospheric influence on C<sub>ff</sub> calculation.

**C3.1 Heterotrophic respiration.** The heterotrophic respiration correction term ( $\beta_{\text{Rh}}$ ) is calculated by the following equation:

$$\beta_{\text{Rh}} = \frac{C_{\text{Rh}}(\Delta_{\text{bg}} - \Delta_{\text{Rh}})}{\Delta_{\text{bg}} + 1000\text{‰}} \quad (\text{C1})$$

where  $C_{\text{Rh}}$  is the CO<sub>2</sub> mole fraction estimated by coupling hourly FLEXPART footprints with the heterotrophic respiration fluxes extracted from the Carnegie Ames Stanford Approach Global Fire Emissions Database Version 4 (CASA-GFED4s) (Randerson et al., 2017; Van Der Werf et al., 2017). We imposed the diurnal cycle from the CASA-GFED3 (Van Der Werf et al., 2010) heterotrophic respiration fluxes (estimated as half of the ecosystem respiration, which is calculated as the difference between net ecosystem exchange and gross ecosystem exchange;  $[\text{NEE} - \text{GEE}]/2$ ) onto the nearest neighbor CASA-GFED4s monthly mean fluxes to approximate hourly resolved fluxes. By aggregating these flux estimates, we created flux maps matching the spatial resolution of the hourly FLEXPART footprints. We then calculated  $C_{\text{Rh}}$  by multiplying the FLEXPART footprints with heterotrophic respiration flux maps. The simulated  $C_{\text{Rh}}$  concentrations were  $1.5 \pm 0.7 \mu\text{mol mol}^{-1}$  (range: 0.5–3.1  $\mu\text{mol mol}^{-1}$ ) in summer and  $2.2 \pm 0.9 \mu\text{mol mol}^{-1}$  (range: 0.4–3.8  $\mu\text{mol mol}^{-1}$ ) in winter.

We used a value of  $40 \pm 35 \text{‰}$  for the  $\Delta(^{14}\text{CO}_2)$  signature of heterotrophic respiration ( $\Delta_{\text{Rh}}$ ), based on the value of  $75 \pm 35 \text{‰}$  in 2015 (Graven et al., 2018) and considering a decrease of 5 % per year (Zazzeri et al., 2023). The disequilibrium

correction from heterotrophic respiration ( $\beta_{RH}$ ) were estimated to be  $-0.06 \pm 0.03$  ppm (range:  $-0.14$  to  $-0.02$  ppm) in summer and  $-0.11 \pm 0.04$  ppm (range:  $-0.20$  to  $-0.02$  ppm) in winter.

**C3.2 Biomass burning.** For the influence of biomass burning, we compared CO<sub>2</sub> emissions from two datasets: CASA-

820 GFED4s (Randerson et al., 2017; Van Der Werf et al., 2017), and the Emissions Database for Global Atmospheric Research (EDGAR) (Edgar, 2024). The key methodological distinction lies in their scopes. CASA-GFED4s quantifies emissions from *open-environment fires* that are detectable by satellites, including wildfires, agricultural residue burning, savanna/rangeland fires, and other small-scale open burning events. In contrast, EDGAR  $C_{bio\_edgar}$  represents *anthropogenic biofuel combustion*, such as emissions from industrial and residential biomass use, while explicitly excluding large-scale wildfires and land-use change-related emissions (LULUCF). Thus, the two datasets characterize different aspects of biomass combustion: CASA-

825 GFED4s captures open burning, whereas EDGAR focuses on controlled, human-induced combustion.

Across Guangdong Province and the four studied cities, biomass burning emissions from CASA-GFED4s accounted for  $<2$  % of Rh emissions, indicating a minor contribution from open-environment fires in this region. By contrast, EDGARv2024ghg  $C_{bio\_edgar}$  estimates represented a much larger proportion of Rh emissions, ranging from 7–

830 29 % (Guangdong), 24–92 % (Guangzhou), 16–97 % (Shenzhen), 13–38 % (Zhanjiang), and 73–248 % (Shaoguan). Given the negligible magnitude of CASA-GFED4s emissions and their minimal effect on  $C_{ff}$  quantification, we focused on the EDGAR  $C_{bio\_edgar}$  dataset for subsequent analysis. This dataset provides a more complete and representative estimate of anthropogenic biomass combustion CO<sub>2</sub> emissions in urban areas, which are most relevant to our study objectives.

To estimate the biomass burning correction term ( $\beta_{BB}$ ) using the EDGAR2024  $C_{bio}$  inventory (Edgar, 2024), we first derived

835 total  $C_{BB}$  simulations ( $C_{BB}$ ) by applying a biomass burning fraction ( $\alpha_{BB}$ ) to the  $C_{bio\_edgar}$  simulations ( $C_{bio\_edgar}$ ). This parameter  $\alpha_{BB}$  represents the proportion of  $C_{bio\_edgar}$  emissions attributable to biomass burning:

$$C_{BB} = C_{bio\_edgar} \cdot \alpha_{BB} \quad (C2)$$

The correction term  $\beta_{BB}$  was subsequently calculated as:

$$\beta_{BB} = \frac{C_{BB}(\Delta_{bg} - \Delta_{BB})}{\Delta_{bg} + 1000\text{‰}} \quad (C3)$$

840 For simulated  $C_{bio\_edgar}$  mole fraction estimation in 2022, we implemented a three-stage process: (1) Generating  $0.1^\circ \times 0.1^\circ$  resolution flux maps through integration of EDGAR2024  $C_{bio\_edgar}$  emission fluxes with FLEXPART atmospheric transport footprints, (2) performing spatiotemporal aggregation to align with FLEXPART model output specifications, and (3) calculating concentrations via convolution operations between transport footprints and optimized flux fields.

We adopted  $\Delta(^{14}\text{CO}_2)$  signatures of  $-14.8 \pm 2.2$  ‰ (annual biomass burning) and  $116.2 \pm 17.6$  ‰ (multi-year biomass burning) calculated in Appendix B. For 2022  $\Delta(^{14}\text{C})$  endmembers for biomass burning, we estimated values of  $116.2 \pm 17.6$  ‰ (0 % annual biomass),  $103.1 \pm 15.8$  ‰ (10 %),  $90.0 \pm 14.1$  ‰ (20 %),  $76.9 \pm 12.3$  ‰ (30 %),  $63.8 \pm 10.6$  ‰ (40 %), and  $50.7 \pm 8.9$  ‰ (50 %), corresponding to incremental annual biomass burning fractions from 0 % to 50 %.

We quantified disequilibrium correction terms under the maximum biomass burning (BB) contribution scenario ( $f_a = 0$  % and  $\alpha_{BB} = 100$  %). The simulated  $C_{BB}$  concentrations were  $0.8 \pm 0.7$   $\mu\text{mol mol}^{-1}$  (range:  $0.0$ – $1.9$   $\mu\text{mol mol}^{-1}$ ) in summer and

850  $1.9 \pm 1.0 \mu\text{mol mol}^{-1}$  (range:  $0.1\text{--}4.4 \mu\text{mol mol}^{-1}$ ) in winter. The BB-specific correction term ( $\beta_{\text{BB}}$ ) exhibited seasonal  
variations:  $-0.09 \pm 0.08 \mu\text{mol mol}^{-1}$  (range:  $-0.46$  to  $-0.01 \mu\text{mol mol}^{-1}$ ) in summer and  $-0.24 \pm 0.12 \mu\text{mol mol}^{-1}$  (range:  
860  $-0.56$  to  $-0.02 \mu\text{mol mol}^{-1}$ ) in winter under 0 % annual biomass burning contribution. The combined correction factor  $\beta$ ,  
integrating contributions from both heterotrophic respiration (Rh) and biomass burning (BB), showed broader ranges:  $-0.16$   
 $\pm 0.09 \mu\text{mol mol}^{-1}$  (range:  $-0.55$  to  $-0.03 \mu\text{mol mol}^{-1}$ ) in summer and  $-0.35 \pm 0.15 \mu\text{mol mol}^{-1}$  (range:  $-0.72$  to  $-0.04 \mu\text{mol}$   
885  $\text{mol}^{-1}$ ) in winter.

#### Appendix D: Background selection

As we summarized in Zhou et al. (2024), Turnbull et al. (2015) concluded that for Indianapolis, a city with relatively simple  
boundary conditions, the upwind background site (Tower 1) is more appropriate compared with continental and regional  
background sites (LEF and NWR). In contrast, for Los Angeles, a city with relatively complex boundary conditions,  
860 Newman et al. (2016) and Miller et al. (2020) tend to use the neighboring regional or continental background sites (MWO  
and LJO; BRW and NWR), because the upwind background within the city may be influenced by emissions from  
neighboring cities and therefore cannot represent the local urban background.

In this study, the cities concerned are central cities or neighboring cities of the Pearl River Delta (PRD) urban agglomeration  
with relatively complex boundary conditions, so we chose the nearest regional background site NL (i.e., SG5) as the  
865 background for determining the  $C_{\text{ff}}$  concentrations.

The Nanling site serves as an ideal atmospheric background monitoring station for Guangdong due to its remote location ( $>$   
 $100$  km from the PRD urban agglomeration), high-altitude terrain ( $1700$  m a.s.l.) avoiding localized pollution.  
Situated above the mixed boundary layer under most meteorological conditions, NL is well isolated from urban  
influences. Its strategic position as a climatic and watershed boundary intercepting seasonal airflows further enables precise  
870 monitoring of regional atmospheric transport patterns while meeting strict background-station criteria for pollution isolation  
and cross-boundary impact assessment.

In addition, trajectory and potential source region analyses further confirm that the Nanling site is representative of regional  
background air under both monsoon regimes. HYSPLIT clustering and PSCF analyses by Zhang et al. (2022) showed that  
during winter, air masses arriving at Nanling predominantly originate from the northern inland provinces (e.g., Hunan,  
875 Jiangxi, Sichuan), while in summer they mostly come from the South China Sea and southeastern coastal regions. These  
summer air masses are typically marine-influenced and low in  $\text{CO}_2$ , consistent with clean background characteristics.

Continuous  $\text{CO}$  observations at NL further support its background representativeness: approximately 90 % of summer  
samples had concentrations below 200 ppb, comparable to other regional background sites, indicating that pollution from the  
PRD rarely reaches NL. Therefore, NL can be considered a robust regional background site for both monsoon seasons.

880 Furthermore, the “annual”  $\text{CO}_2$  and  $\Delta(^{14}\text{C})$  averages at NL, which are close to those at the Jungfraujoch, occupy the upper-  
right section of the Keeling plot of  $\Delta(^{14}\text{C})$  versus  $\text{CO}_2$ , representing the background end-member when compared with

Waliguan (Fig. 3). Additionally, the  $\delta^{14}\text{C}$  and  $\text{CO}_2$  averages at NL were the highest and the lowest, respectively, among the 30 sampling sites (Table A1), consistent with background-level characteristics.

885 **Appendix E: Comparison of C<sub>fl</sub> fractions and concentrations among various cities****Table E1** Comparison of C<sub>fl</sub> and C<sub>bio</sub> fractions derived from  $\Delta(^{14}\text{CO}_2)$  measurements in various cities

| City            | Time             | Background       | C <sub>fl</sub> (%) | C <sub>bio</sub> (%) | References            |
|-----------------|------------------|------------------|---------------------|----------------------|-----------------------|
| Paris           | 2010             | MHD <sup>a</sup> | 77                  | 23                   | (Lopez et al., 2013)  |
| Los Angeles     | 2006-2013 winter | LJO <sup>b</sup> | 86                  | 14                   | (Newman et al., 2016) |
| Los Angeles     | 2006-2013 summer | LJO              | 93                  | 7                    | (Newman et al., 2016) |
| Los Angeles     | 2014.11-2016.03  | MWO <sup>c</sup> | 80                  | 20                   | (Miller et al., 2020) |
| Beijing         | 2014             | WLG <sup>d</sup> | 75.2 ± 14.6         | 24.8                 | (Niu et al., 2016)    |
| Xiamen          | 2014             | WLG              | 59.1 ± 26.8         | 40.9                 | (Niu et al., 2016)    |
| Xi'an           | 2014 winter      | WLG              | 92.7 ± 9.7          | 7.3 ± 9.7            | (Zhou et al., 2020)   |
| Xi'an, urban    | 2016 summer      | WLG              | 82.5 ± 23.8         | 17.5                 | (Wang et al., 2018)   |
| Xi'an, urban    | 2016 winter      | WLG              | 61.8 ± 10.6         | 38.2                 | (Wang et al., 2018)   |
| Xi'an, suburban | 2016 summer      | WLG              | 90.0 ± 24.8         | 10.0                 | (Wang et al., 2018)   |
| Xi'an, suburban | 2016 winter      | WLG              | 57.4 ± 9.7          | 42.6                 | (Wang et al., 2018)   |
| Guangzhou       | 2022 winter      | NL <sup>e</sup>  | 79 ± 5              | 21                   | this study            |
| Shenzhen        | 2022 winter      | NL               | 73 ± 6              | 27                   | this study            |
| Zhanjiang       | 2022 winter      | NL               | 59 ± 4              | 41                   | this study            |
| Shaoguan        | 2022 winter      | NL               | 53 ± 13             | 47                   | this study            |

<sup>a</sup> Mace Head, <sup>b</sup> La Jolla, <sup>c</sup> Mount Wilson Observatory, <sup>d</sup> Waliguan, <sup>e</sup> Nanling

**Table E2** Comparison of  $C_{ff}$  concentrations derived from  $\Delta(^{14}\text{CO}_2)$  measurements in various cities

| Country        | City            | Sampling period | Sampling time | Duration | $C_{ff}$ ( $\mu\text{mol mol}^{-1}$ ) | References                  |
|----------------|-----------------|-----------------|---------------|----------|---------------------------------------|-----------------------------|
| Poland         | Krakow          | 1989            | --            | 2 weeks  | 27.5                                  | (Kuc et al., 2003)          |
| Poland         | Krakow          | 1994            | --            | 2 weeks  | 10                                    | (Kuc et al., 2003)          |
| Poland         | Krakow          | 2005–2009       | --            | 1 week   | 1.98–2.18                             | (Zimnoch et al., 2012)      |
| Poland         | Kasprowy Wierch | 2005–2009       | --            | 1 week   | 1.95–2.08                             | (Zimnoch et al., 2012)      |
| Poland         | Gliwice         | 2011.01–2013.01 | 10:00         | --       | 23–24                                 | (Piotrowska et al., 2020)   |
| Czech Republic | Prague          | 2001–2018       | --            | 1 month  | $25.51 \pm 11.45$                     | (Svetlik et al., 2010)      |
| Slovakia       | Bratislava      | 1999–2007       | --            | 1 month  | $25.56 \pm 6.90$                      | (Svetlik et al., 2010)      |
| Germany        | Heidelberg      | 1986–1996       | --            | 2 weeks  | $11.09 \pm 0.24$                      | (Levin and Rödenbeck, 2008) |
| Germany        | Heidelberg      | 1997–2007       | --            | 2 weeks  | $10.92 \pm 0.34$                      | (Levin and Rödenbeck, 2008) |
| Hungary        | Debrecen        | 2009/10.01      | --            | 4 weeks  | 10–15                                 | (Molnár et al., 2010)       |
| France         | Paris           | 2010.01–02      | --            | --       | 26.4                                  | (Lopez et al., 2013)        |
| United Kingdom | London          | 2020.06–07      | 12:00         | 30 min   | $17.3 \pm 3.0$                        | (Zazzeri et al., 2023)      |
| United States  | Los Angeles     | 2006–2013       | 14:00         | 1 h      | $22.9 \pm 5.6$                        | (Newman et al., 2016)       |
| United States  | Los Angeles     | 2014.11–2016.03 | 14:00         | 1 h      | $13.2 \pm 9.4$                        | (Miller et al., 2020)       |
| United States  | Indianapolis    | 2010–2015       | 14:00         | 1 h      | $10.8 \pm 1.0$                        | (Turnbull et al., 2015)     |
| China          | Urumqi          | 2014–2016       | 14:00–16:00   | 2 h      | $45.6 \pm 12.9$                       | (Zhou et al., 2020)         |
| China          | Lanzhou         | 2014–2016       | 14:00–16:00   | 2 h      | $36.4 \pm 8.8$                        | (Zhou et al., 2020)         |
| China          | Xi'an           | 2011–2013       | afternoon     | --       | $40.1 \pm 3.8$                        | (Zhou et al., 2022)         |
| China          | Xi'an           | 2014–2016       | afternoon     | --       | $25.7 \pm 1.1$                        | (Zhou et al., 2022)         |
| China          | Suburban Xi'an  | 2016.01–11      | 14:00         | 15 min   | $23.5 \pm 6.5$                        | (Wang et al., 2018)         |
| China          | Near Xi'an      | 2021.04–2022.03 | 14:00         | 40 min   | $13.1 \pm 10.9$                       | (Liu et al., 2024)          |
| China          | Beijing         | 2014.01–12      | 10:00         | 10 min   | $39.7 \pm 36.1$                       | (Niu et al., 2016)          |
| China          | Beijing         | 2014–2016 (Jan) | 14:00–16:00   | 2 h      | $27.0 \pm 0.3$                        | (Zhou et al., 2020)         |
| China          | Beijing         | 2020 winter     | 14:00         | 1 h      | $19.7 \pm 22.0$                       | (Wang et al., 2022b)        |
| China          | Wuhan           | 2014–2016       | 14:00–16:00   | 2 h      | $34.5 \pm 10.0$                       | (Zhou et al., 2020)         |
| China          | Xiamen          | 2014            | 10:00         | 10 min   | $13.6 \pm 12.3$                       | (Niu et al., 2016)          |
| China          | Guangzhou       | 2011            | 20:00         | 45 min   | $23.7 \pm 12.9$                       | (Ding et al., 2013)         |
| China          | Guangzhou       | 2022            | 13:00–17:00   | 20 min   | $15.3 \pm 5.2$                        | this study                  |
| China          | Shenzhen        | 2022            | 13:00–17:00   | 20 min   | $13.7 \pm 10.2$                       | this study                  |
| China          | Zhanjiang       | 2022            | 13:00–17:00   | 20 min   | $10.0 \pm 5.2$                        | this study                  |
| China          | Shaoguan        | 2022            | 13:00–17:00   | 20 min   | $8.2 \pm 7.0$                         | this study                  |

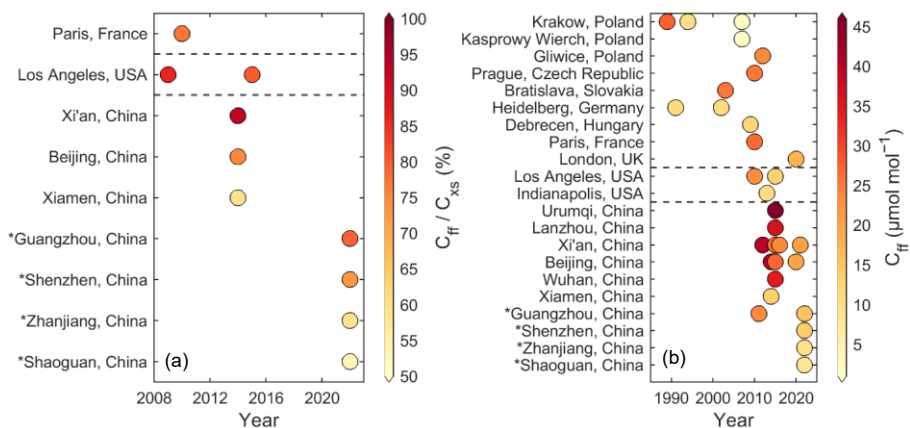
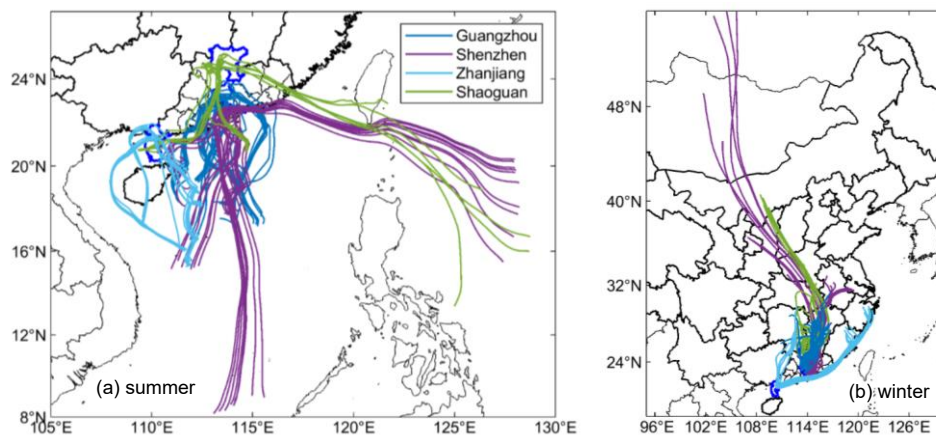
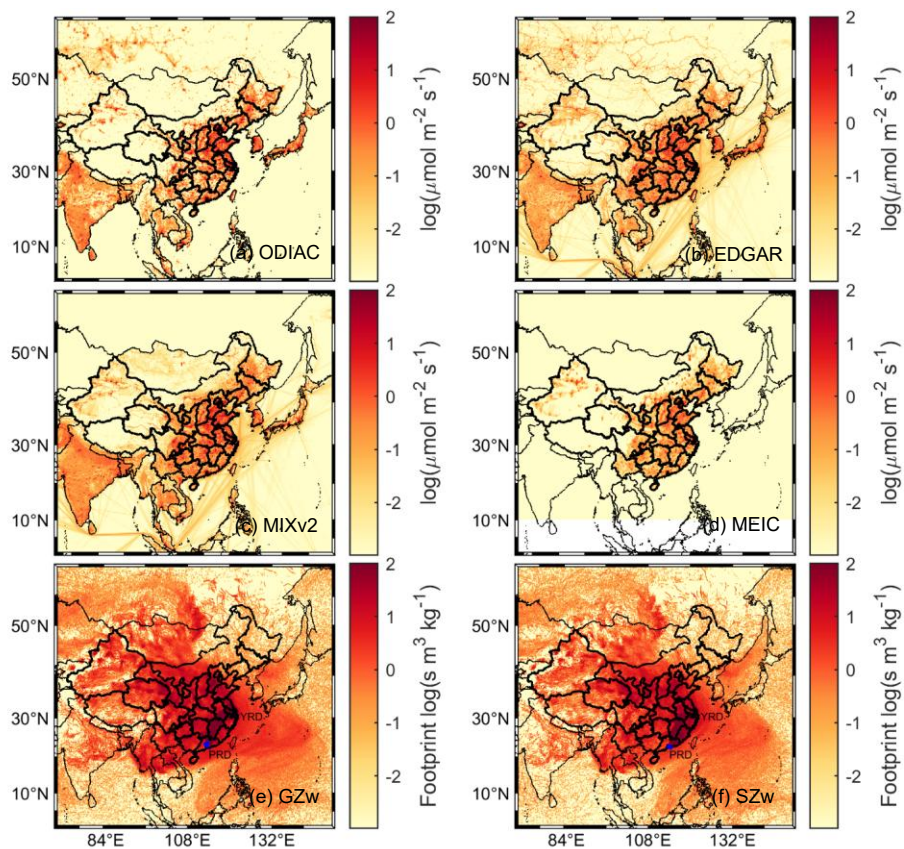


**Figure E1** Comparison of (a)  $C_{ff}$  fractions in  $C_{xs}$  and (b)  $C_{ff}$  concentrations derived from  $\Delta(^{14}\text{CO}_2)$  measurements from previous studies and this study (\*) in various cities across European countries (Kuc et al., 2003; Levin and Rödenbeck, 2008; Molnár et al., 2010; Svetlik et al., 2010; Zimnoch et al., 2012; Lopez et al., 2013; Piotrowska et al., 2020; Zazzeri et al., 2023), United States (Turnbull et al., 2015; Newman et al., 2016; Miller et al., 2020), and China (Ding et al., 2013; Niu et al., 2016; Zhou et al., 2020; Wang et al., 2022b; Liu et al., 2024; Zhou et al., 2022). In (a), Los Angeles, Beijing, Guangzhou, and Shenzhen are megacities, Xi'an is a supercity, and other are large and medium cities (Council, 2022). Values in (a) and (b) refer to Tables E1 and E2, respectively.

Appendix F: HYSPLIT back trajectories and FLEXPART footprints

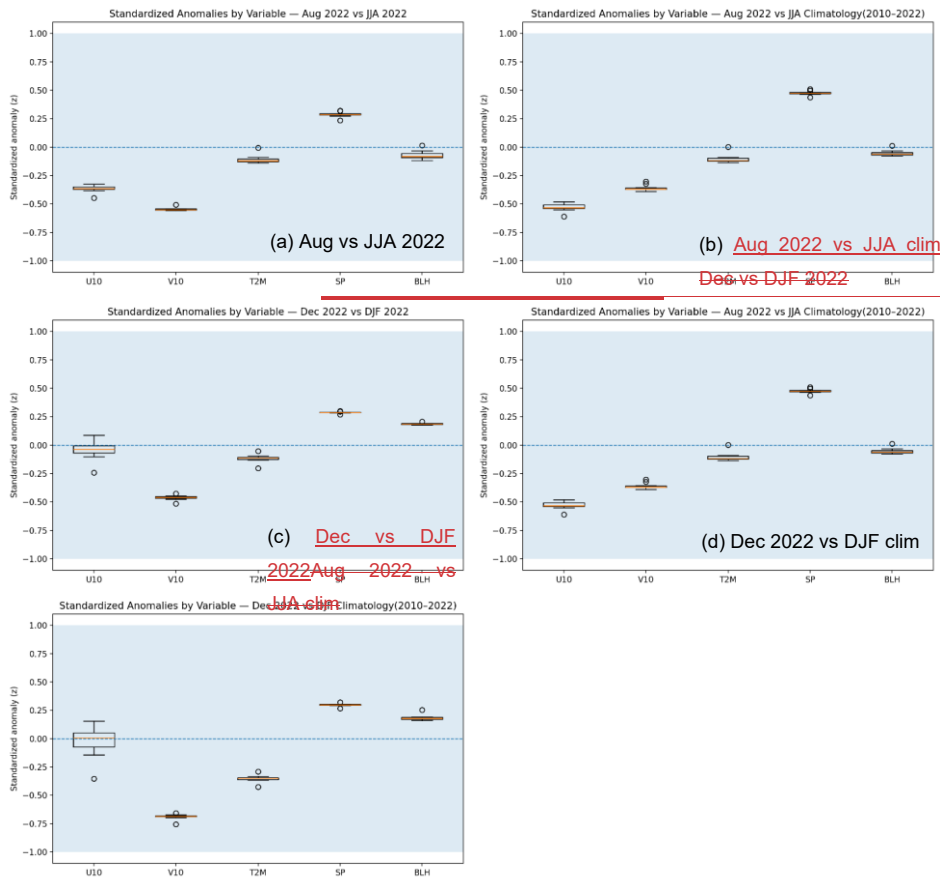


905 **Figure F1** HYSPLIT back trajectories for a 72-h duration for Guangzhou, Shenzhen, Zhanjiang, and Shaoguan in **(a)** summer and **(b)** winter. The trajectories reveal maritime inflow in summer and continental inflow in winter, corroborating the ERA5-based analysis. National boundaries were taken from Natural Earth (<https://www.naturalearthdata.com/>, last accessed: 9 March 2024).



**Figure F2** Annual mean  $C_{ff}$  emissions in China from four gridded inventory datasets: **(a)** ODIAC, **(b)** EDGAR, **(c)** MIXv2, and **(d)** MEIC, and FLEXPART footprints simulating  $C_{ff}$  emissions for **(e)** Guangzhou (GZ), **(f)** Shenzhen (SZ) in winter (w) by releasing particles at the blue sampling sites at heights from 0–100 m a.s.l. over a period of 30 days. The YRD and PRD represent Yangtze River Delta and Pearl River Delta urban agglomeration labelled in (e) and (f). Boundaries of nations and Chinese provinces were obtained from Natural Earth (<https://www.naturalearthdata.com/>, last accessed: 9 March 2024).

**Appendix G: Transport representativeness analysis**



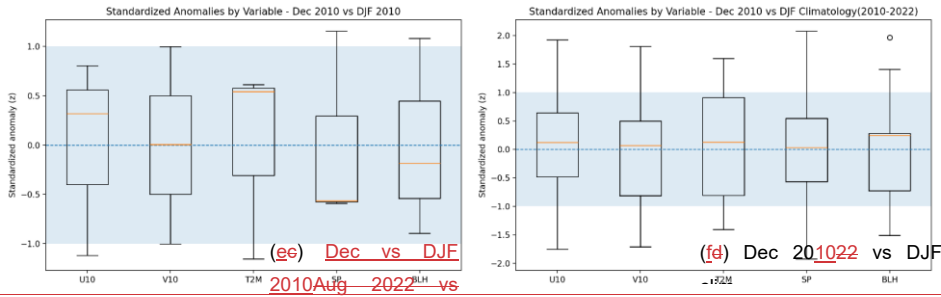
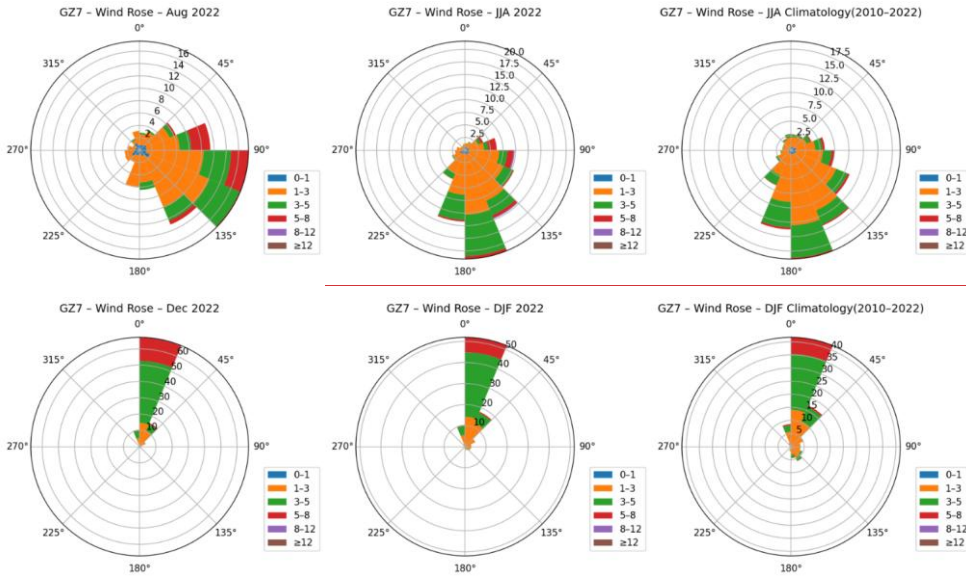
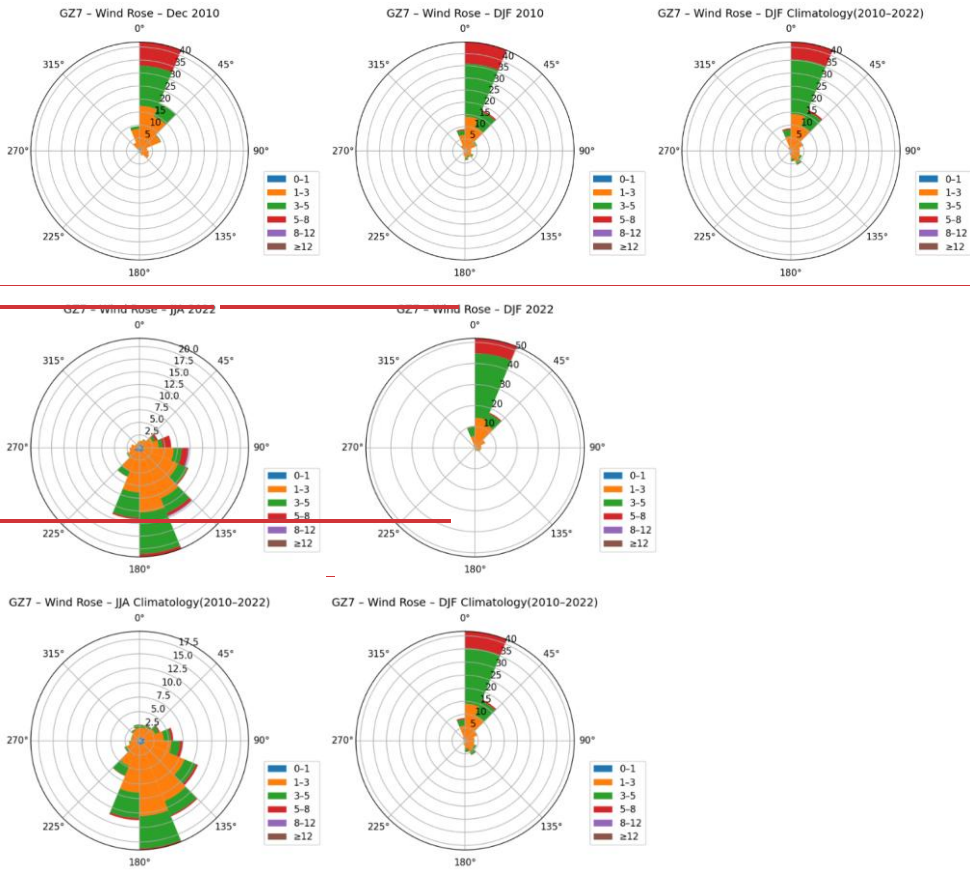


**Figure G1** Box-and-whisker plots of standardized anomalies ( $z$ ) by ERA5 meteorological variables (U10, V10, T2M, SP, BLH) across Guangzhou sites (GZ1-10) for (a) Aug 2022 vs JJA 2022, (b) Aug 2022 vs JJA climatology (2010-2022), (c) Dec 2022 vs DJF 2022, (d) Dec 2022 vs DJF climatology (2010-2022), (e) Aug 2022 vs JJA climatology (2010-2022), and (f) Dec 2010 vs DJF climatology (2010-2022) at GZ7.

U10, V10, T2M, SP, BLH are 10 m zonal and meridional winds (U10, V10), 2 m temperature (T2M), surface pressure (SP), and planetary boundary-layer height (PBLH), respectively. The shaded region denotes  $|z| \leq 1$  (typical range).



930



935

**Figure G2** ERA5 wind roses for GZ7 site (wind speed unit:  $\text{m s}^{-1}$ ) showing six panels: (a) August 2022, (b) JJA 2022December 2022, (c) JJA climatology (2010–2022)–JJA 2022, (d) December 2022DJF 2022, (e) DJF 2022JJA climatology (2010–2022), and (f) DJF climatology (2010–2022). (g) December 2010, (h) DJF 2010, (i) DJF climatology (2010–2022). These illustrate that both August 2022, and December 2022, and December 2010 are consistent with their canonical summer and winter flow regimes.

940 **Table G1** Dec 2010 vs Dec 2022 statistics of U10, V10, wind speed, T2M, PBLH, and ventilation at GZ7, including mean, standard deviation, median, and p-values from Student's t-test and Mann–Whitney U test.

| variable    | Dec 2010 |        |        | Dec 2022 |        |        | t_stat | t_p_value             | mw_stat           | mw_p_value            |
|-------------|----------|--------|--------|----------|--------|--------|--------|-----------------------|-------------------|-----------------------|
|             | mean     | std    | median | mean     | std    | median |        |                       |                   |                       |
| u10         | -0.8     | 0.8    | -0.9   | -0.8     | 0.7    | -0.9   | 1.1    | $2.8 \times 10^{-1}$  | $2.8 \times 10^5$ | $6.8 \times 10^{-1}$  |
| v10         | -2.1     | 1.9    | -1.9   | -3.4     | 1.5    | -3.4   | 15.2   | $2.2 \times 10^{-48}$ | $4.0 \times 10^5$ | $3.5 \times 10^{-52}$ |
| wind speed  | 2.6      | 1.5    | 2.2    | 3.6      | 1.3    | 3.5    | -13.6  | $1.3 \times 10^{-39}$ | $1.5 \times 10^5$ | $1.4 \times 10^{-49}$ |
| t2m         | 289.0    | 5.3    | 289.6  | 287.1    | 3.1    | 286.8  | 8.6    | $2.3 \times 10^{-17}$ | $3.6 \times 10^5$ | $3.1 \times 10^{-23}$ |
| PBLH        | 377.0    | 359.9  | 261.9  | 476.4    | 304.0  | 457.6  | -5.8   | $1.1 \times 10^{-08}$ | $2.1 \times 10^5$ | $6.4 \times 10^{-15}$ |
| ventilation | 1258.0   | 1651.0 | 578.4  | 2024.5   | 1761.7 | 1724.4 | -8.7   | $1.2 \times 10^{-17}$ | $1.8 \times 10^5$ | $5.3 \times 10^{-31}$ |

**Table G2** Dec 2010 vs Dec 2022 wind direction sector frequencies (in %) at GZ7.

| Wind sector (°C) | Dec2010 freq (%) | Dec2022 freq (%) |
|------------------|------------------|------------------|
| 0–45             | 61.7             | 82.7             |
| 45–90            | 12.1             | 5.2              |
| 90–135           | 7.7              | 1.2              |
| 135–180          | 3.0              | 0.0              |
| 180–225          | 1.2              | 0.0              |
| 225–270          | 0.4              | 0.0              |
| 270–315          | 0.9              | 0.0              |
| 315–360          | 13.0             | 10.9             |

945

## Appendix H: Historical comparison and corrections

**Table H1.** Summary of all available  $C_{ff}$  datasets for historical variations used in this study and referenced from previous literature, including site type, coordinates, sampling period, time, number of samples ( $n$ ), and references.

| City      | Site type        | Site location       | Sampling period     | Sampling time | Duration | $n$   | Reference           |
|-----------|------------------|---------------------|---------------------|---------------|----------|-------|---------------------|
| Guangzhou | Urban            | GZ7 in Fig. 1f      | Oct 2010 – Nov 2011 | 20:00         | 45 min   | 58    | (Ding et al., 2013) |
|           | Urban & suburban | GZ1–10 in Figs. 1ef | Aug/Dec 2022        | 13:00–17:00   | 20 min   | 40/40 | This study          |

|         |          |  |                   |             |        |       |                      |
|---------|----------|--|-------------------|-------------|--------|-------|----------------------|
| Beijing | Urban    | RCEES <sup>a</sup> (40.02°N, 116.34°E, 15 m a.g.l.)  | Jan–Dec 2014      | 10:00       | 10 min | 24    | (Niu et al., 2016)   |
|         |          |  | Jan/Jul 2014–2016 | 14:00–16:00 | 2 h    | 42/42 | (Zhou et al., 2020)  |
|         |          |  | Dec 2020–Jan 2021 | 14:00       | 1 h    | 31    | (Wang et al., 2022b) |
| Xi'an   | Urban    | IEECAS <sup>b</sup> (34.23°N, 108.89°E, 10 m a.g.l.) | 2011–2013         | afternoon   | --     | ~120  | (Zhou et al., 2022)  |
|         |          |  | 2014–2016         | afternoon   | --     | ~75   |                      |
|         | Suburban | two sites (34.34°N, 108.86°E; 34.21°N, 108.88°E)     | Jan–Nov 2016      | 14:00       | 15 min | 38    | (Wang et al., 2018)  |
|         | Suburban | Qinling Mountain (34.06°N, 108.34°E)                 | Apr 2021–Mar 2022 | 14:00       | 40 min | 24    | (Liu et al., 2024)   |

<sup>a</sup> Research Center for Eco-Environmental Sciences, Chinese Academy of Sciences (RCEES). <sup>b</sup> Institute of Earth

950 Environment, Chinese Academy of Sciences (IEECAS).

**Table H2.** Harmonized comparison of  $C_{\text{IT}}$  mole fractions at identical sites, seasons, and sampling times, after correction to common background conditions.

| City      | Site type | Site location                                    | Sampling period  | Sampling time | Duration | $n$  | Background                  | $C_{\text{IT}}$ ( $\mu\text{mol mol}^{-1}$ ) | Corrected $C_{\text{IT}}$ ( $\mu\text{mol mol}^{-1}$ ) |
|-----------|-----------|--|------------------|---------------|----------|------|-----------------------------|--|--|
| Guangzhou | Urban     | GZ7 (GIGCAS) <sup>a</sup>                        | Winter 2010      | 20:00         | 45 min   | 83   | remote regions <sup>b</sup> | 44.228.4 ± 5.30                              | 34.921.6 ± 4.246.9 <sup>d</sup>                        |
|           |           |  | Winter 2022      | 13:00–17:00   | 20 min   | 4    | NL air                      | 16.8 ± 3.4                                   | 12.51.6 ± 3.4 <sup>e</sup>                             |
| Beijing   | Urban     | RCEES (40.02°N, 116.34°, 15 m.a.g.l.)            | Winter 2014–2016 | 14:00–16:00   | 2 h      | 21   | QXL                         | 27.0 ± 0.3                                   | 27.6 ± 0.3 <sup>f</sup>                                |
|           |           |  | Winter 2020      | 14:00         | 1 h      | 31   | WLG <sup>c</sup>            | 19.7 ± 22.0                                  | 19.7 ± 22.0  |
| Xi'an     | Urban     | IEECAS (34.23°N, 108.89°E, 10 m.a.g.l.)          | 2011–2013        | afternoon     | --       | ~120 | WLG                         | 40.1 ± 3.8                                   | 40.1 ± 3.8   |
|           |           |  | 2014–2016        | afternoon     | --       | ~75  | WLG                         | 25.7 ± 1.1                                   | 25.7 ± 1.1   |
|           | Suburban  | two sites (34.34°N, 108.86°E; 34.21°N, 108.88°E) | 2016             | 14:00         | 15 min   | 38   | WLG                         | 23.5 ± 6.5                                   | 23.5 ± 6.5   |
|           | Suburban  | Qinling Mountain (34.06°N, 108.34°E)             | 2021–2022        | 14:00         | 40 min   | 24   | WLG                         | 13.1 ± 10.9                                  | 13.1 ± 10.9  |

<sup>a</sup> Guangzhou Institute of Geochemistry, Chinese Academy of Sciences (GIGCAS). <sup>b</sup> remote regions (Qinghai, Gansu, and Tibet) with  $\delta^{13}\text{C}$  value of  $37.5 \pm 3.0$  ‰. <sup>c</sup>  $C_{\text{IT}}$  concentrations in winter Beijing obtained from Wang et al. (2022b) Wang et al.<sup>40</sup> were estimated based on the background atmospheric  $\Delta(^{14}\text{C}\text{O}_2)$  measurements from Waliguan (Liu et al., 2024). <sup>d</sup> corrected to 14:00 sampling and recalculated

955

960 using a common NL tree-ring  $\delta^{14}\text{C}$  background as a harmonized reference baseline for inter-period comparison. The NL tree-ring  $\delta^{14}\text{C}$  represents a growing-season (March–October) integrated proxy at Nanling, and the 2022 value ( $-20.8\text{‰}$ ) is linearly extrapolated from the 2011–2020 tree-ring record (Li et al., 2025b); it is therefore not intended to represent wintertime background variability. <sup>e</sup> corrected-to recalculated using the same NL tree-ring  $\delta^{14}\text{C}$  background harmonized reference baseline (33.9 ‰) as in footnote d. <sup>f</sup> corrected to the WLG background.

**H1 Sampling-time difference (20:00 vs 14:00) in  $C_{\text{ff}}$  for Guangzhou.** Ding et al. (2013) collected flask samples around 20:00 LT, immediately after the evening rush hour, whereas our 2022 samples were collected between 13:00 and 975 17:00 LT under well-mixed boundary-layer conditions. To quantify the potential diurnal  $C_{\text{ff}}$  bias, we used continuous CO observations near GZ7 from two independent sources: (1) the Guangdong Provincial Environmental Monitoring Centre and (2) the nationwide air quality database (<https://quotsoft.net/air/#messy>, last access: 18 October 2025), and applied the formulation

$$C_{\text{ff}} \approx \Delta\text{CO}/R - \frac{\Delta\text{CO}}{R}$$

970 where  $\Delta\text{CO} = \text{CO} - \text{CO}_{\text{bg}}$ , and  $R = \Delta\text{CO}/\Delta\text{CO}_{2,\text{ff}}$  denotes the **emissionconcentration** ratio between CO and fossil-fuel  $\text{CO}_2$ . The value of  $R$  is strongly time-dependent and source-specific. Nighttime  $R$  values tend to be higher than daytime values because (i) nighttime emissions are dominated by direct fossil-fuel combustion while biogenic  $\text{CO}_2$  sources (e.g., respiration) remain constant but emit no CO, and (ii) oxidative sinks (e.g., OH radicals) are weaker at night. Therefore, applying an afternoon-derived  $R$  to nighttime data likely provides a lower bound for the actual nighttime  $C_{\text{ff}}$  enhancement.

975 **Scheme 1 (this study’s observation, December 2022):**

We used the December diurnal mean CO data at a site close to GZ7, subtracted the NL background to obtain  $\Delta\text{CO}$ , and divided by the afternoon-specific  $R = 13.3 \text{ ppb ppm}^{-1}$  (derived from the regression between  $\Delta\text{CO}$  and  $^{14}\text{C}$ -based  $\Delta\text{CO}_{2,\text{ff}}$ ). The  $\Delta\text{CO}$  increased from 168.3 ppb at 14:00 to 220.7 ppb at 20:00, corresponding to an estimated nighttime  $C_{\text{ff}}$  enhancement of approximately 3.2 ppm, or about 21 % higher than the afternoon value. Because the slope  $R$  was determined during well- 980 mixed afternoon periods, this result likely represents a lower limit; the actual nighttime–afternoon  $C_{\text{ff}}$  contrast may be smaller.

**Scheme 2 (Guangzhou dataset, winter 2023, supplementary analysis):**

We applied the same approach to the continuous CO data at the site close to GZ7 for the winter season (December 2023 – February 2024). After subtracting the NL background,  $\Delta\text{CO}$  was divided by the seasonal  $R = 9.08 \text{ ppb ppm}^{-1}$  obtained from regressions of CO against total  $\text{CO}_2$  (Zhang et al., 2025). As this  $R$  reflects bulk  $\text{CO}_2$  rather than specifically fossil-fuel  $\text{CO}_2$ , we applied an empirical correction (dividing  $R$  by 0.8; Turnbull et al. (2011)). The resulting analysis indicates that  $\Delta\text{CO}$  increased by 66.9 ppb from 14:00 to 20:00, implying a  $C_{\text{ff}}$  enhancement difference of roughly 5.9 ppm ( $\approx 35\%$ ).

Overall, while continuous CO<sub>2ff</sub> data are not available for 2022, our CO-based analysis suggests that the C<sub>ff</sub> signal at 20:00 is moderately higher than that at 14:00. This finding is consistent with the reviewer's expectation that post-rush-hour conditions retain a stronger fossil-fuel signature compared with the well-mixed afternoon atmosphere. The semi-quantitative assessment indicates that the C<sub>ff</sub> concentration during post-rush-hour (20:00) is approximately 21–35 % higher than during well-mixed afternoon periods, consistent with the expected diurnal accumulation of fossil-fuel CO<sub>2</sub> under weaker nighttime boundary-layer mixing.

#### 995 Appendix I: Comparison of contributions of coal, oil and natural gas to C<sub>ff</sub> concentrations in various cities

**Table II** Comparison of contributions of coal, oil and natural gas to C<sub>ff</sub> concentrations in various cities

| City        | Time             | F <sub>coal</sub> (%) | F <sub>oil</sub> (%) | F <sub>ng</sub> (%) | References              |
|-------------|------------------|-----------------------|----------------------|---------------------|-------------------------|
| Paris       | 2010             | < 1                   | 30                   | 70                  | (Lopez et al., 2013)    |
| Los Angeles | 2007.10          | < 1                   | 69                   | 31                  | (Djuricin et al., 2010) |
| Los Angeles | 2007.12          | < 1                   | 61                   | 39                  | (Djuricin et al., 2010) |
| Los Angeles | 2008.02          | < 1                   | 58                   | 42                  | (Djuricin et al., 2010) |
| Los Angeles | 2008.04          | < 1                   | 52                   | 48                  | (Djuricin et al., 2010) |
| Los Angeles | 2006-2013 winter | < 1                   | 68                   | 32                  | (Newman et al., 2016)   |
| Los Angeles | 2006-2013 summer | < 1                   | 55                   | 45                  | (Newman et al., 2016)   |
| Xi'an       | 2014 winter      | 72.6 ± 10.4           | 13.8 ± 10.4          | 13.6                | (Zhou et al., 2014)     |
| Xi'an       | 2019.12-2020.01  | 54 ± 4                | 24 ± 14              | 22 ± 13             | (Wang et al., 2022b)    |
| Beijing     | 2020.12-2021.01  | 17 ± 10               | 28 ± 19              | 55 ± 9              | (Wang et al., 2022b)    |
| Guangzhou   | 2022 winter      | 49 ± 25               | 29 ± 22              | 22 ± 19             | this study              |
| Shenzhen    | 2022 winter      | 47 ± 25               | 29 ± 21              | 24 ± 20             | this study              |
| Zhanjiang   | 2022 winter      | 43 ± 24               | 29 ± 21              | 28 ± 21             | this study              |
| Shaoguan    | 2022 winter      | 39 ± 24               | 34 ± 23              | 27 ± 21             | this study              |

Appendix J:  $R_{CO/CO2ff}$  for sites, cities and comparison

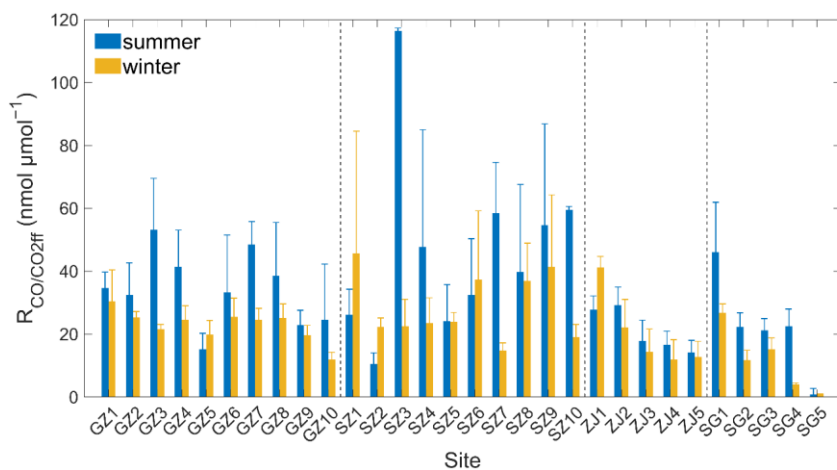


Figure J1  $R_{CO/CO2ff}$  averages at the 30 sampling sites. Error bars denote  $\pm 1$  SD of the seasonal  $R_{CO/CO2ff}$  ratios at each site.

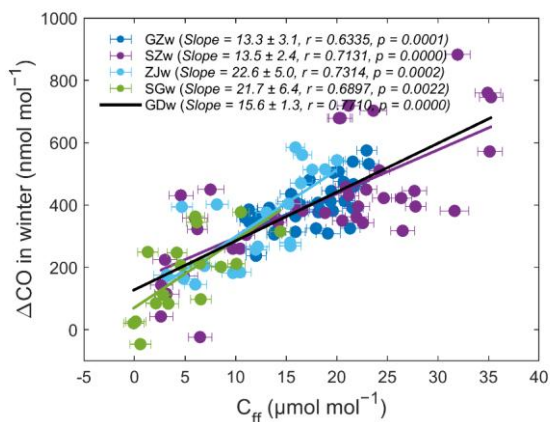


Figure J2  $\Delta CO: C_{ff}$  for Guangzhou, Shenzhen, Zhanjiang, and Shaoguan in winter. Vertical and horizontal error bars denote the propagated uncertainties in  $C_{ff}$  and  $CO$ , respectively, propagated from their measurement and calculation uncertainties.

||005

**Table J1** Observational emissionconcentration ratios of CO to C<sub>ff</sub> (R<sub>CO/CO2ff</sub>) for China and Chinese cities

| City                   | Time             | R <sub>CO/CO2ff</sub> (nmol μmol <sup>-1</sup> ) | Method <sup>a</sup> | References                    |
|------------------------|------------------|--|---------------------|-------------------------------|
| China                  | 2001             | 68.8   | I                   | (Suntharalingam et al., 2004) |
| China                  | 2004–2010        | 44 ± 3   | II                  | (Turnbull et al., 2011)       |
| China                  | 1998             | 56.3   | I                   | (Tohjima et al., 2014)        |
| China                  | 2010             | 37.5   | I                   | (Tohjima et al., 2014)        |
| Mainland China         | 2009             | 36.3   | I                   | (Fu et al., 2015)             |
| Yellow Sea             | 2016             | 35.0   | I                   | (Tang et al., 2018)           |
| China, CN <sup>b</sup> | 2014–2016        | 31 ± 8   | II                  | (Lee et al., 2020)            |
| China, CE <sup>b</sup> | 2014–2016        | 36 ± 2   | II                  | (Lee et al., 2020)            |
| China, CB <sup>b</sup> | 2014–2016        | 29 ± 8   | II                  | (Lee et al., 2020)            |
| China, OB <sup>b</sup> | 2014–2016        | 31 ± 4   | II                  | (Lee et al., 2020)            |
| Beijing                | 2005             | 54.3   | I                   | (Han et al., 2009)            |
| Beijing/Tianjin        | 2009–2010        | 59.5   | I                   | (Silva et al., 2013)          |
| Beijing                | 2014             | 30.4 ± 1.6                                       | II                  | (Niu et al., 2018)            |
| Rural Beijing          | 2004             | 72.3   | I                   | (Wang et al., 2010)           |
| Rural Beijing          | 2005             | 52.5   | I                   | (Wang et al., 2010)           |
| Rural Beijing          | 2006             | 48.1   | I                   | (Wang et al., 2010)           |
| Rural Beijing          | 2007             | 43.7   | I                   | (Wang et al., 2010)           |
| Rural Beijing          | 2008             | 47.0   | I                   | (Wang et al., 2010)           |
| Rural Beijing          | 2009–2010        | 47 ± 2   | II                  | (Turnbull et al., 2011)       |
| Xi'an                  | 2016             | 46 ± 13  | II                  | (Wang et al., 2018)           |
| Near Xi'an             | 2021             | 23 ± 6   | II                  | (Liu et al., 2024)            |
| Xiamen                 | 2014             | 29.6 ± 3   | II                  | (Niu et al., 2018)            |
| Guangzhou              | 2009–2010        | 35.8   | I                   | (Silva et al., 2013)          |
| Guangzhou              | 2014–2017 winter | 23.8   | I                   | (Mai et al., 2021)            |
| Guangzhou              | 2022 winter      | 13.3 ± 3.1                                       | II                  | Fig. J2, this study           |
| Shenzhen               | 2022 winter      | 13.5 ± 2.4                                       | II                  | Fig. J2, this study           |
| Zhanjiang              | 2022 winter      | 22.6 ± 5.0                                       | II                  | Fig. J2, this study           |
| Shaoguan               | 2022 winter      | 21.7 ± 6.4                                       | II                  | Fig. J2, this study           |

<sup>a</sup> by correction from R<sub>CO/CO2</sub> by increased 20 % (Method I) and estimation from Δ<sup>14</sup>C measurements (Method II), <sup>b</sup> CN represents the air masses from northeast China, CE for central eastern China around the Shandong area, CB for continental background air, and OB for ocean background.

#### 1010 **Code availability**

The FLEXPART 10.4 model is available at <https://www.flexpart.eu/>. The MixSIAR 3.1.12 model is available via GitHub at <https://brianstock.github.io/MixSIAR/index.html>. The HYSPLIT model is available at <https://www.arl.noaa.gov/hysplit/>. In this study, commercial software such as MATLAB R2023a, and public software such as R 4.3.2 and Python 3.9 are used for data processing and result visualization.

#### 1015 **Data availability**

Data generated in this study are available in Supplement Dataset 1 and seasonal averages in Table A1. Additional data related to this paper may be requested from the corresponding authors. The Carnegie Ames Stanford Approach Global Fire Emissions Database Version 4 (CASA-GFED4s) dataset is available at [https://daac.ornl.gov/VEGETATION/guides/fire\\_emissions\\_v4\\_R1.html](https://daac.ornl.gov/VEGETATION/guides/fire_emissions_v4_R1.html). The CASA-GFED3 dataset is available at <http://nacp-files.nacarbon.org/nacp-kawa-01/>. The Open-source Data Inventory for Anthropogenic CO<sub>2</sub> (ODIAC) is available from <https://db.cger.nies.go.jp/dataset/ODIAC/>. The Emissions Database for Global Atmospheric Research (EDGAR) Global Greenhouse Gas and Air Pollutant Emissions are from <https://edgar.jrc.ec.europa.eu>. The Multi-resolution Emission Inventory for China (MEIC) and the Open Biomass Burning Emission Inventory for China (OBBEIC) are available from <http://meicmodel.org.cn>. The MIXv2 Asian emission inventory (MIXv2) is available from <https://csl.noaa.gov/groups/csl4/modeldata/data/Li2023/>. The National Centers for Environmental Prediction's Climate Forecast System (CFSv2) Reanalysis data that drive the FLEXPART model is available at <https://rda.ucar.edu/datasets/ds094.0/>. The National Centers for Environmental Prediction's Global Data Assimilation System (GDAS) Reanalysis data that drives the HYSPLIT model is available at <ftp.arl.noaa.gov/pub/archives/reanalysis>.

#### **Author contribution**

1030 G.Z., D.C., Jun Li, and P.L. conceived and designed the study. Almost all authors participated in the sampling organized by Jun Li and P.L.. Z.N. provided data in Beijing and Xi'an. P.D. provided data from Ding et al., (2013) in Guangzhou. R.L. conducted the sample graphitization. Sanyuan Z. handled the <sup>14</sup>C measurement by AMS. P.L. and B.L. performed the simulations. P.L. conducted the data search and analysis, and wrote the article, with contributions from G.Z., Jun Li, Z.C., Jing L., and T.Z. for revisions and improvements.

#### 1035 **Competing interests**

The authors declare no competing interest.

## Acknowledgements

We gratefully acknowledge the research team from Professor Gan Zhang's group for their essential support in air sampling, including staff scientists, postdoctoral researchers, and graduate students. Special thanks are extended to Mr. Jiangtao Li for his dedicated assistance with field sampling and laboratory extraction procedures.

## Financial support

This study was supported by the National Natural Science Foundation of China (NSFC; nos. 42330715, 42103082, 42030715, and 42177241), Guangdong Provincial Applied Science and Technology Research and Development Program (Grant nos. 2022A1515011271, and 2022A1515011851), the Alliance of International Science Organizations (Grant no. ANSO-CR-KP-2021-05), China Postdoctoral Science Foundation (Grant no. 2022T150652), Special Research Assistant Program of the Chinese Academy of Sciences (CAS), and Director's Fund of Guangzhou Institute of Geochemistry, CAS (Grant no. 2021SZJJ-3).

## References

- Akagi, S. K., Yokelson, R. J., Wiedinmyer, C., Alvarado, M. J., Reid, J. S., Karl, T., Crounse, J. D., and Wennberg, P. O.: Emission factors for open and domestic biomass burning for use in atmospheric models, *Atmos. Chem. Phys.*, 11, 4039–4072, 10.5194/acp-11-4039-2011, 2011.
- Bakwin, P. S., Tans, P. P., White, J. W. C., and Andres, R. J.: Determination of the isotopic ( $^{13}\text{C}/^{12}\text{C}$ ) discrimination by terrestrial biology from a global network of observations, *Global Biogeochem. Cy.*, 12, 555–562, <https://doi.org/10.1029/98GB02265>, 1998.
- Chen, Y., Yao, B., Wu, J., Yang, H., Ding, A., Liu, S., Li, X., O'Doherty, S., Li, J., Li, Y., Yu, H., Wang, W., Chen, L., Yang, X., Fu, T.-M., Shen, H., Ye, J., Wang, C., and Zhu, L.: Observations and emission constraints of trichlorofluoromethane (CFC-11) in southeastern China: first-year results from a new AGAGE station, *Environ. Res. Lett.*, 19, 074043, 10.1088/1748-9326/ad5857, 2024.
- Cheng, P., Xiao, X. M., Tian, H., Huang, B. J., Wilkins, R. W. T., and Zhang, Y. Z.: Source controls on geochemical characteristics of crude oils from the Qionghai Uplift in the western Pearl River Mouth Basin, offshore South China Sea, *Mar. Pet. Geol.*, 40, 85–98, <https://doi.org/10.1016/j.marpetgeo.2012.10.003>, 2013.
- Coplen, T. B.: New guidelines for reporting stable hydrogen, carbon, and oxygen isotope-ratio data, *Geochim. Cosmochim. Ac.*, 60, 3359–3360, 1996.
- Council, O. o. t. L. G. f. t. S. N. P. C. o. t. S., Guo, D., and She, J. (Eds.): Tabulation on 2020 China Population Census by County, China Statistics Press, Beijing, China2022.
- Crippa, M., Guizzardi, D., Pagani, F., Banja, M., Muntean, M., E., S., Becker, W., Monforti-Ferrario, F., Quadrelli, R., Riusquez Martin, A., Taghavi-Moharamli, P., Köykkä, J., Grassi, G., Rossi, S., Brandao De Melo, J., Oom, D., Branco, A., San-Miguel, J., and Vignati, E.: GHG emissions of all world countries, Publications Office of the European Union, LuxembourgJRC134504, 10.2760/953322, 2023.
- Dhakal, S.: Urban energy use and carbon emissions from cities in China and policy implications, *Energy Policy*, 37, 4208–4219, <https://doi.org/10.1016/j.enpol.2009.05.020>, 2009.
- Ding, P., Shen, C., Yi, W., Wang, N., Ding, X., Fu, D., and Liu, K.: Fossil-Fuel-Derived  $\text{CO}_2$  Contribution to the Urban Atmosphere in Guangzhou, South China, Estimated by  $^{14}\text{CO}_2$  Observation, 2010–2011, *Radiocarbon*, 55, 791–803, 2013.
- Djuricin, S., Pataki, D. E., and Xu, X.: A comparison of tracer methods for quantifying  $\text{CO}_2$  sources in an urban region, *J. Geophys. Res. Atmos.*, 115, D11303, <https://doi.org/10.1029/2009JD012236>, 2010.

- Duren, R. M. and Miller, C. E.: Measuring the carbon emissions of megacities, *Nature Clim. Change*, 2, 560–562, 10.1038/nclimate1629, 2012.
- Emissions Database for Global Atmospheric Research (EDGAR\_2024\_GHG): [https://edgar.jrc.ec.europa.eu/dataset\\_ghg2024](https://edgar.jrc.ec.europa.eu/dataset_ghg2024), last
- 1080 ICOS ATC CO<sub>2</sub> Release, Jungfraujoch (13.9 m), 2016-12-12–2024-03-31, ICOS RI: <https://hdl.handle.net/11676/4-Kot58QX1b5u-e8SGD8XTPy> (last accessed: 28 July 2024) last
- ICOS ATC/CAL <sup>14</sup>C Release, Jungfraujoch (6.0 m), 2015-09-21–2023-10-02, ICOS RI: [https://hdl.handle.net/11676/6c\\_RZ7NHc2dnZv7d84BMY\\_YY](https://hdl.handle.net/11676/6c_RZ7NHc2dnZv7d84BMY_YY) (last accessed: 28 July 2024) last
- 1085 Friedlingstein, P., O'Sullivan, M., Jones, M. W., Andrew, R. M., Bakker, D. C. E., Hauck, J., Landschützer, P., Le Quéré, C., Lujikx, I. T., Peters, G. P., Peters, W., Pongratz, J., Schwingshackl, C., Sitch, S., Canadell, J. G., Ciais, P., Jackson, R. B., Alin, S. R., Anthoni, P., Barbero, L., Bates, N. R., Becker, M., Bellouin, N., Decharme, B., Bopp, L., Brasika, I. B. M., Cadule, P., Chamberlain, M. A., Chandra, N., Chau, T. T. T., Chevallier, F., Chini, L. P., Cronin, M., Dou, X., Enyo, K., Evans, W., Falk, S., Feely, R. A., Feng, L., Ford, D. J., Gasser, T., Ghattas, J., Gkritzalis, T., Grassi, G., Gregor, L., Gruber, N., Gürses, Ö., Harris, I., Hefner, M., Heinke, J., Houghton, R. A., Hurtt, G. C., Iida, Y., Ilyina, T., Jacobson, A. R., Jain, A., Jarníková, T., Jersild, A., Jiang, F., Jin, Z., Joos, F., Kato, E., Keeling, R. F., Kennedy, D., Klein Goldewijk, K., Knauer, J., Korsbakken, J. I., Körtzinger, A., Lan, X., Lefèvre, N., Li, H., Liu, J., Liu, Z., Ma, L., Marland, G., Mayot, N., McGuire, P. C., McKinley, G. A., Meyer, G., Morgan, E. J., Munro, D. R., Nakaoka, S. I., Niwa, Y., O'Brien, K. M., Olsen, A., Omar, A. M., Ono, T., Paulsen, M., Pierrot, D., Pockock, K., Poulter, B., Powis, C. M., Rehder, G., Resplandy, L., Robertson, E., Rödenbeck, C., Rosan, T. M., Schwinger, J., Séférian, R., Smallman, T. L., Smith, S. M., Sospedra-Alfonso, R., Sun, Q., Sutton, A. J., Sweeney, C., Takao, S., Tans, P. P., Tian, H., Tilbrook, B., Tsujino, H., Tubiello, F., van der Werf, G. R., van Ooijen, E., Wanninkhof, R., Watanabe, M., Wimart-Rousseau, C., Yang, D., Yang, X., Yuan, W., Yue, X., Zaehle, S., Zeng, J., and Zheng, B.: Global Carbon Budget 2023, *Earth Syst. Sci. Data*, 15, 5301–5369, 10.5194/essd-15-5301-2023, 2023a.
- 1090 Friedlingstein, P., O'Sullivan, M., Jones, M. W., Andrew, R. M., Bakker, D. C. E., Hauck, J., Landschützer, P., Le Quéré, C., Lujikx, I. T., Peters, G. P., Peters, W., Pongratz, J., Schwingshackl, C., Sitch, S., Canadell, J. G., Ciais, P., Jackson, R. B., Alin, S. R., Anthoni, P., Barbero, L., Bates, N. R., Becker, M., Bellouin, N., Decharme, B., Bopp, L., Brasika, I. B. M., Cadule, P., Chamberlain, M. A., Chandra, N., Chau, T. T. T., Chevallier, F., Chini, L. P., Cronin, M., Dou, X., Enyo, K., Evans, W., Falk, S., Feely, R. A., Feng, L., Ford, D. J., Gasser, T., Ghattas, J., Gkritzalis, T., Grassi, G., Gregor, L., Gruber, N., Gürses, Ö., Harris, I., Hefner, M., Heinke, J., Houghton, R. A., Hurtt, G. C., Iida, Y., Ilyina, T., Jacobson, A. R., Jain, A., Jarníková, T., Jersild, A., Jiang, F., Jin, Z., Joos, F., Kato, E., Keeling, R. F., Kennedy, D., Klein Goldewijk, K., Knauer, J., Korsbakken, J. I., Körtzinger, A., Lan, X., Lefèvre, N., Li, H., Liu, J., Liu, Z., Ma, L., Marland, G., Mayot, N., McGuire, P. C., McKinley, G. A., Meyer, G., Morgan, E. J., Munro, D. R., Nakaoka, S. I., Niwa, Y., O'Brien, K. M., Olsen, A., Omar, A. M., Ono, T., Paulsen, M., Pierrot, D., Pockock, K., Poulter, B., Powis, C. M., Rehder, G., Resplandy, L., Robertson, E., Rödenbeck, C., Rosan, T. M., Schwinger, J., Séférian, R., Smallman, T. L., Smith, S. M., Sospedra-Alfonso, R., Sun, Q., Sutton, A. J., Sweeney, C., Takao, S., Tans, P. P., Tian, H., Tilbrook, B., Tsujino, H., Tubiello, F., van der Werf, G. R., van Ooijen, E., Wanninkhof, R., Watanabe, M., Wimart-Rousseau, C., Yang, D., Yang, X., Yuan, W., Yue, X., Zaehle, S., Zeng, J., and Zheng, B.: Global Carbon Budget 2023, *Earth Syst. Sci. Data*, 15, 5301–5369, 10.5194/essd-15-5301-2023, 2023b.
- 1100 Fu, X., Zhang, H., Lin, C.-J., Feng, X., Zhou, L., and Fang, S.: Correlation slopes of GEM/CO, GEM/CO<sub>2</sub>, and GEM/CH<sub>4</sub> and estimated mercury emissions in China, South Asia, the Indochinese Peninsula, and Central Asia derived from observations in northwestern and southwestern China, *Atmos. Chem. Phys.*, 15, 1013–1028, 2015.
- 1115 Graven, H., Fischer, M. L., Lueker, T., Jeong, S., Guilderson, T. P., Keeling, R. F., Bambha, R., Brophy, K., Callahan, W., Cui, X., Frankenberg, C., Gurney, K. R., LaFranchi, B. W., Lehman, S. J., Michelsen, H., Miller, J. B., Newman, S., Paplawsky, W., Parazoo, N. C., Sloop, C., and Walker, S. J.: Assessing fossil fuel CO<sub>2</sub> emissions in California using atmospheric observations and models, *Environ. Res. Lett.*, 13, 065007, 10.1088/1748-9326/aabd43, 2018.
- Graven, H. D. and Gruber, N.: Continental-scale enrichment of atmospheric <sup>14</sup>C from the nuclear power industry: Potential impact on the estimation of fossil fuel-derived CO<sub>2</sub>, *Atmos. Chem. Phys.*, 11, 12339–12349, 2011.
- 1120 Graven, H. D., Stephens, B. B., Guilderson, T. P., Campos, T. L., Schimel, D. S., Campbell, J. E., and Keeling, R. F.: Vertical profiles of biospheric and fossil fuel-derived CO<sub>2</sub> and fossil fuel CO<sub>2</sub>:CO ratios from airborne measurements of  $\Delta^{14}\text{C}$ , CO<sub>2</sub> and CO above Colorado, USA, *Tellus B*, 61, 536–546, <https://doi.org/10.1111/j.1600-0889.2009.00421.x>, 2009.
- Gurney, K. R., Liang, J. M., Roest, G., Song, Y., Mueller, K., and Lauvaux, T.: Under-reporting of greenhouse gas emissions in U.S. cities, *Nat. Commun.*, 12, 553, 10.1038/s41467-020-20871-0, 2021.

- Han, P., Zeng, N., Oda, T., Lin, X., Crippa, M., Guan, D., Janssens-Maenhout, G., Ma, X., Liu, Z., and Shan, Y.: Evaluating China's fossil-fuel CO<sub>2</sub> emissions from a comprehensive dataset of nine inventories, *Atmos. Chem. Phys.*, 20, 11371–11385, 2020.
- Han, S., Kondo, Y., Oshima, N., Takegawa, N., Miyazaki, Y., Hu, M., Lin, P., Deng, Z., Zhao, Y., and Sugimoto, N.: Temporal variations of elemental carbon in Beijing, *J. Geophys. Res. Atmos.*, 114, D23202, 2009.
- 1130 Hua, Q., Turnbull, J. C., Santos, G. M., Rakowski, A. Z., Ancapichún, S., De Pol-Holz, R., Hammer, S., Lehman, S. J., Levin, I., and Miller, J. B.: Atmospheric radiocarbon for the period 1950–2019, *Radiocarbon*, 1–23, 2021.
- Huang, X., Li, M., Li, J., and Song, Y.: A high-resolution emission inventory of crop burning in fields in China based on MODIS Thermal Anomalies/Fire products, *Atmos. Environ.*, 50, 9–15, <https://doi.org/10.1016/j.atmosenv.2012.01.017>, 2012.
- 1135 IAEA: Management of waste containing tritium and carbon-14, Technical Report Series No. 421, International Atomic Energy Agency, Vienna, Austria 2004.
- Karion, A., Lopez-Coto, I., Gourdji, S. M., Mueller, K., Ghosh, S., Callahan, W., Stock, M., DiGangi, E., Prinzivalli, S., and Whetstone, J.: Background conditions for an urban greenhouse gas network in the Washington, DC, and Baltimore metropolitan region, *Atmos. Chem. Phys.*, 21, 6257–6273, [10.5194/acp-21-6257-2021](https://doi.org/10.5194/acp-21-6257-2021), 2021.
- 1140 Kuc, T., Rozanski, K., Zimnoch, M., Necki, J. M., and Korus, A.: Anthropogenic emissions of CO<sub>2</sub> and CH<sub>4</sub> in an urban environment, *Appl. Energy*, 75, 193–203, [https://doi.org/10.1016/S0306-2619\(03\)00032-1](https://doi.org/10.1016/S0306-2619(03)00032-1), 2003.
- Atmospheric Carbon Dioxide Dry Air Mole Fractions from the NOAA GML Carbon Cycle Cooperative Global Air Sampling Network, 1968–2022, Version: 2023-08-28: <https://doi.org/10.15138/wkqj-f215>, last
- 1145 Le Quéré, C., Andrew, R. M., Canadell, J. G., Sitch, S., Korsbakken, J. I., Peters, G. P., Manning, A. C., Boden, T. A., Tans, P. P., Houghton, R. A., Keeling, R. F., Alin, S., Andrews, O. D., Anthoni, P., Barbero, L., Bopp, L., Chevallier, F., Chini, L. P., Ciais, P., Currie, K., Delire, C., Doney, S. C., Friedlingstein, P., Gkritzalis, T., Harris, I., Hauck, J., Haverd, V., Hoppema, M., Klein Goldewijk, K., Jain, A. K., Kato, E., Körtzinger, A., Landschützer, P., Lefèvre, N., Lenton, A., Lienert, S., Lombardozi, D., Melton, J. R., Metzl, N., Millero, F., Monteiro, P. M. S., Munro, D. R., Nabel, J. E. M. S., Nakaoka, S., O'Brien, K., Olsen, A., Omar, A. M., Ono, T., Pierrot, D., Poulter, B., Rödenbeck, C., Salisbury, J., Schuster, U., Schwinger, J., Séférian, R., Skjelvan, I., Stocker, B. D., Sutton, A. J., Takahashi, T., Tian, H., Tilbrook, B., van der Laan-Luijkx, I. T., van der Werf, G. R., Viovy, N., Walker, A. P., Wiltshire, A. J., and Zaehe, S.: Global Carbon Budget 2016, *Earth Syst. Sci. Data*, 8, 605–649, [10.5194/essd-8-605-2016](https://doi.org/10.5194/essd-8-605-2016), 2016.
- Lee, H., Dlugokencky, E. J., Turnbull, J. C., Lee, S., Lehman, S. J., Miller, J. B., Pétron, G., Lim, J. S., Lee, G. W., Lee, S. S., and Park, Y. S.: Observations of atmospheric <sup>14</sup>C<sub>2</sub> at Anmyeondo GAW station, South Korea: implications for fossil fuel CO<sub>2</sub> and emission ratios, *Atmos. Chem. Phys.*, 20, 12033–12045, [10.5194/acp-20-12033-2020](https://doi.org/10.5194/acp-20-12033-2020), 2020.
- 1155 Levin, I. and Rödenbeck, C.: Can the envisaged reductions of fossil fuel CO<sub>2</sub> emissions be detected by atmospheric observations?, *Naturwissenschaften*, 95, 203–208, 2008.
- Levin, I., Kromer, B., Schmidt, M., and Sartorius, H.: A novel approach for independent budgeting of fossil fuel CO<sub>2</sub> over Europe by <sup>14</sup>C<sub>2</sub> observations, *Geophys. Res. Lett.*, 30, 2194, 2003.
- 1160 Lewis, C. W., Klouda, G. A., and Ellenson, W. D.: Radiocarbon measurement of the biogenic contribution to summertime PM-2.5 ambient aerosol in Nashville, TN, *Atmos. Environ.*, 38, 6053–6061, <https://doi.org/10.1016/j.atmosenv.2004.06.011>, 2004.
- Li, J., Lin, B., Wang, W., Li, P., Li, J., Han, P., Feng, W., Cheng, Z., Zhu, S., Zhang, T., Chen, D., and Zhang, G.: High-Resolution Mapping of Fossil Fuel CO<sub>2</sub> Using Plant Radiocarbon and Bayesian Inversion: Toward a City-Scale Emission Audit, *Environ. Sci. Technol.*, 10.1021/acs.est.5c09553, 2025a.
- 1165 Li, J., Wei, N., Wang, X., Li, P., Sun, Y., Feng, W., Cheng, Z., Zhu, S., Wang, W., Chen, D., Zhao, S., Zhong, G., Zhou, G., Li, J., and Zhang, G.: Continental-scale impact of bomb radiocarbon affects historical fossil fuel carbon dioxide reconstruction, *Communications Earth & Environment*, 6, 603, [10.1038/s43247-025-02532-6](https://doi.org/10.1038/s43247-025-02532-6), 2025b.
- Li, L.: A Decade of Transformative Achievements in Energy Consumption Revolution (in Chinese), 2023.
- 1170 Li, M., Liu, H., Geng, G., Hong, C., Liu, F., Song, Y., Tong, D., Zheng, B., Cui, H., Man, H., Zhang, Q., and He, K.: Anthropogenic emission inventories in China: a review, *Natl. Sci. Rev.*, 4, 834–866, [10.1093/nsr/nwx150](https://doi.org/10.1093/nsr/nwx150) %J National Science Review, 2017.
- Li, M., Kurokawa, J., Zhang, Q., Woo, J. H., Morikawa, T., Chatani, S., Lu, Z., Song, Y., Geng, G., Hu, H., Kim, J., Cooper, O. R., and McDonald, B. C.: MIXv2: a long-term mosaic emission inventory for Asia (2010–2017), *Atmos. Chem. Phys.*, 24, 3925–3952, [10.5194/acp-24-3925-2024](https://doi.org/10.5194/acp-24-3925-2024), 2024.
- 1175

- Li, M., Zhang, Q., Zheng, B., Tong, D., Lei, Y., Liu, F., Hong, C., Kang, S., Yan, L., Zhang, Y., Bo, Y., Su, H., Cheng, Y., and He, K.: Persistent growth of anthropogenic non-methane volatile organic compound (NMVOC) emissions in China during 1990–2017: drivers, speciation and ozone formation potential, *Atmos. Chem. Phys.*, 19, 8897–8913, 10.5194/acp-19-8897-2019, 2019.
- 1180 Li, Q., Guo, X., Zhai, W., Xu, Y., and Dai, M.: Partial pressure of CO<sub>2</sub> and air-sea CO<sub>2</sub> fluxes in the South China Sea: Synthesis of an 18-year dataset, *Progress in Oceanography*, 182, 102272, <https://doi.org/10.1016/j.pocan.2020.102272>, 2020.
- Liu, W., Niu, Z., Feng, X., Zhou, W., Liang, D., Lyu, M., Wang, G., Lu, X., Liu, L., and Turnbull, J. C.: Atmospheric CO<sub>2</sub> and <sup>14</sup>C observations at the northern foot of the Qinling Mountains in China: Temporal characteristics and source quantification, *Sci. Total Environ.*, 920, 170682, <https://doi.org/10.1016/j.scitotenv.2024.170682>, 2024.
- 1185 Lo Vullo, E. and Monforti, F.: Fossil CO<sub>2</sub> and GHG emissions of all world countries, 10.2760/687800, 2019.
- Lopez, M., Schmidt, M., Delmotte, M., Colomb, A., Gros, V., Janssen, C., Lehman, S. J., Mondelain, D., Perrussel, O., Ramonet, M., Xueref-Remy, I., and Bousquet, P.: CO, NO<sub>x</sub> and <sup>13</sup>C as tracers for fossil fuel CO<sub>2</sub>: results from a pilot study in Paris during winter 2010, *Atmos. Chem. Phys.*, 13, 7343–7358, 10.5194/acp-13-7343-2013, 2013.
- 1190 Mai, B., Deng, X., Liu, X., Li, T., Guo, J., and Ma, Q.: The climatology of ambient CO<sub>2</sub> concentrations from long-term observation in the Pearl River Delta region of China: Roles of anthropogenic and biogenic processes, *Atmos. Environ.*, 251, 118266, <https://doi.org/10.1016/j.atmosenv.2021.118266>, 2021.
- Maier, F., Levin, I., Conil, S., Gachkivskiy, M., Denier van der Gon, H., and Hammer, S.: Uncertainty in continuous ΔCO<sub>2</sub>-based ΔffCO<sub>2</sub> estimates derived from 14C flask and bottom-up ΔCO/ΔffCO<sub>2</sub> ratios, *Atmos. Chem. Phys.*, 24, 8205–8223, 10.5194/acp-24-8205-2024, 2024.
- 1195 Multi-resolution Emission Inventory model for China: <http://meicmodel.org.cn> (last accessed: 14 March 2024) last
- Miller, J. B. and Tans, P. P.: Calculating isotopic fractionation from atmospheric measurements at various scales, *Tellus B*, 55, 207–214, <https://doi.org/10.1034/j.1600-0889.2003.00020.x>, 2003.
- 1200 Miller, J. B., Lehman, S. J., Verhulst, K. R., Miller, C. E., Duren, R. M., Yadav, V., Newman, S., and Sloop, C. D.: Large and seasonally varying biospheric CO<sub>2</sub> fluxes in the Los Angeles megacity revealed by atmospheric radiocarbon, *Proc. Natl. Acad. Sci.*, 117, 26681–26687, 2020.
- Mohn, J., Szidat, S., Fellner, J., Rechberger, H., Quartier, R., Buchmann, B., and Emmenegger, L.: Determination of biogenic and fossil CO<sub>2</sub> emitted by waste incineration based on 14CO<sub>2</sub> and mass balances, *Bioresour. Technol.*, 99, 6471–6479, <https://doi.org/10.1016/j.biortech.2007.11.042>, 2008.
- 1205 Molnár, M., Major, I., Haszpra, L., Svétlík, I., Svingor, É., and Veres, M.: Fossil fuel CO<sub>2</sub> estimation by atmospheric <sup>14</sup>C measurement and CO<sub>2</sub> mixing ratios in the city of Debrecen, Hungary, *J. Radioanal. Nucl.*, 286, 471–476, 10.1007/s10967-010-0791-2, 2010.
- Newman, S., Xu, X., Gurney, K. R., Hsu, Y. K., Li, K. F., Jiang, X., Keeling, R., Feng, S., O’Keefe, D., Patarasuk, R., Wong, K. W., Rao, P., Fischer, M. L., and Yung, Y. L.: Toward consistency between trends in bottom-up CO<sub>2</sub> emissions and top-down atmospheric measurements in the Los Angeles megacity, *Atmos. Chem. Phys.*, 16, 3843–3863, 10.5194/acp-16-3843-2016, 2016.
- 1210 Niu, Z., Zhou, W., Huang, Y., Wang, S., Zhang, G., Feng, X., Lu, X., Lyu, M., and Turnbull, J. C.: Identification of Urban Carbon Emission Peaks through Tree-Ring 14C, *Environ. Sci. Technol.*, 58, 17313–17319, 10.1021/acs.est.4c06041, 2024.
- Niu, Z., Zhou, W., Feng, X., Feng, T., Wu, S., Cheng, P., Lu, X., Du, H., Xiong, X., and Fu, Y.: Atmospheric fossil fuel CO<sub>2</sub> traced by <sup>14</sup>C and air quality index pollutant observations in Beijing and Xiamen, China, *Environ. Sci. Pollut. R.*, 25, 17109–17117, 10.1007/s11356-018-1616-z, 2018.
- 1215 Niu, Z. C., Zhou, W. J., Wu, S. G., Cheng, P., Lu, X., Xiong, X., Du, H., Fu, Y., and Wang, G.: Atmospheric fossil fuel CO<sub>2</sub> traced by Δ<sup>14</sup>C in Beijing and Xiamen, China: temporal variations, inland/coastal differences and influencing factors, *Environ. Sci. Technol.*, 50, 5474–5480, 2016.
- 1220 Oda, T. and Maksyutov, S.: A very high-resolution (1 km×1 km) global fossil fuel CO<sub>2</sub> emission inventory derived using a point source database and satellite observations of nighttime lights, *Atmos. Chem. Phys.*, 11, 543–556, 10.5194/acp-11-543-2011, 2011.
- ODIAC Fossil Fuel CO<sub>2</sub> Emissions Dataset (Version name: ODIAC2022), Center for Global Environmental Research, National Institute for Environmental Studies. (Reference date: 2024/01/22): <https://db.cger.nies.go.jp/dataset/ODIAC/>, last

- 1225 Pataki, D. E., Ehleringer, J. R., Flanagan, L. B., Yakir, D., Bowling, D. R., Still, C. J., Buchmann, N., Kaplan, J. O., and Berry, J. A.: The application and interpretation of Keeling plots in terrestrial carbon cycle research, *Global Biogeochem. Cy.*, 17, 1022, <https://doi.org/10.1029/2001GB001850>, 2003.
- Ping, H., Chen, H., Zhu, J., George, S. C., Mi, L., Pang, X., and Zhai, P.: Origin, source, mixing, and thermal maturity of natural gases in the Panyu lower uplift and the Baiyun depression, Pearl River Mouth Basin, northern South China Sea, AAPG Bull., 102, 2171–2200, 10.1306/04121817160 %J AAPG Bulletin, 2018.
- 1230 Piotrowska, N., Pazdur, A., Pawelczyk, S., Rakowski, A. Z., Sensula, B., and Tudyka, K.: Human Activity Recorded in Carbon Isotopic Composition of Atmospheric CO<sub>2</sub> in Gliwice Urban Area and Surroundings (Southern Poland) in the Years 2011–2013, *Radiocarbon*, 62, 141–156, 10.1017/RDC.2019.92, 2020.
- Pisso, I., Sollum, E., Grythe, H., Kristiansen, N. I., Cassiani, M., Eckhardt, S., Arnold, D., Morton, D., Thompson, R. L., Groot Zwaaftink, C. D., Evangeliou, N., Sodemann, H., Haimberger, L., Henne, S., Brunner, D., Burkhart, J. F., Fouilloux, A., Brioude, J., Philipp, A., Seibert, P., and Stohl, A.: The Lagrangian particle dispersion model FLEXPART version 10.4, *Geosci. Model Dev.*, 12, 4955–4997, 10.5194/gmd-12-4955-2019, 2019.
- 1235 Qian, Y., Liu, J., Hao, F., Bao, X., Xu, S., Teng, C., and Wang, Z.: Geochemical characteristics and origins of natural gas in the Zhu III sub-basin, Pearl River Mouth Basin, China, *Mar. Pet. Geol.*, 101, 117–131, 10.1016/j.marpetgeo.2018.12.007, 2018.
- 1240 Global Fire Emissions Database, Version 4.1 (GFEDv4): <https://doi.org/10.3334/ORNLDAC/1293>, last  
Rosendahl, C.: Proxy to fossil-fuel CO<sub>2</sub> emission ratios: in-situ versus inventory data, 2022.
- Saha, S., Moorthi, S., Wu, X., Wang, J., Nadiga, S., Tripp, P., Behringer, D., Hou, Y.-T., Chuang, H.-y., Iredell, M., Ek, M., Meng, J., Yang, R., Mendez, M. P., van den Dool, H., Zhang, Q., Wang, W., Chen, M., and Becker, E.: NCEP Climate Forecast System Version 2 (CFSv2) Selected Hourly Time-Series Products, Research Data Archive at the National Center for Atmospheric Research, Computational and Information Systems Laboratory [dataset], 2011.
- 1245 Shi, Q., Zheng, B., Zheng, Y., Tong, D., Liu, Y., Ma, H., Hong, C., Geng, G., Guan, D., He, K., and Zhang, Q.: Co-benefits of CO<sub>2</sub> emission reduction from China's clean air actions between 2013–2020, *Nat. Commun.*, 13, 5061, 10.1038/s41467-022-32656-8, 2022.
- 1250 Silva, S. J., Arellano, A. F., and Worden, H. M.: Toward anthropogenic combustion emission constraints from space-based analysis of urban CO<sub>2</sub>/CO sensitivity, *Geophys. Res. Lett.*, 40, 4971–4976, <https://doi.org/10.1002/grl.50954>, 2013.  
(Shaoguan Municipal Bureau of Statistics), Shaoguan Statistical Yearbook 2023: [https://www.sg.gov.cn/sgtj/gkmlpt/content/2/2565/post\\_2565540.html#6602](https://www.sg.gov.cn/sgtj/gkmlpt/content/2/2565/post_2565540.html#6602) (last accessed: 14 March 2024), last
- 1255 Song, Y., Liu, B., Miao, W., Chang, D., and Zhang, Y.: Spatiotemporal variation in nonagricultural open fire emissions in China from 2000 to 2007, *Global Biogeochem. Cy.*, 23, <https://doi.org/10.1029/2008GB003344>, 2009.
- Stein, A. F., Draxler, R. R., Rolph, G. D., Stunder, B. J. B., Cohen, M. D., and Ngan, F.: NOAA's HYSPLIT Atmospheric Transport and Dispersion Modeling System, *Bulletin of the American Meteorological Society*, 96, 2059–2077, 10.1175/bams-d-14-00110.1, 2015.
- 1260 Stock, B., Jackson, A., Ward, E., Parnell, A., Phillips, D., and Semmens, B.: Analyzing mixing systems using a new generation of Bayesian tracer mixing models, *PeerJ*, 10.7287/peerj.preprints.26884, 2018.
- Stuiver, M. and Polach, H. A.: Discussion reporting of <sup>14</sup>C data, *Radiocarbon*, 19, 355–363, 1977.
- Suntharalingam, P., Jacob, D. J., Palmer, P. I., Logan, J. A., Yantosca, R. M., Xiao, Y., Evans, M. J., Streets, D. G., Vay, S. L., and Sachse, G. W.: Improved quantification of Chinese carbon fluxes using CO<sub>2</sub>/CO correlations in Asian outflow, *J. Geophys. Res. Atmos.*, 109, D18S18, <https://doi.org/10.1029/2003JD004362>, 2004.
- 1265 Svetlík, I., Povinec, P. P., Molnár, M., Vána, M., Šivo, A., and Bujtás, T.: Radiocarbon in the Air of Central Europe: Long-Term Investigations, *Radiocarbon*, 52, 823–834, 10.1017/S0033822200045847, 2010.
- Tang, W., Arellano, A. F., DiGangi, J. P., Choi, Y., Diskin, G. S., Agustí-Panareda, A., Parrington, M., Massart, S., Gaubert, B., Lee, Y., Kim, D., Jung, J., Hong, J., Hong, J. W., Kanaya, Y., Lee, M., Stauffer, R. M., Thompson, A. M., Flynn, J. H., and Woo, J. H.: Evaluating high-resolution forecasts of atmospheric CO and CO<sub>2</sub> from a global prediction system during KORUS-AQ field campaign, *Atmos. Chem. Phys.*, 18, 11007–11030, 10.5194/acp-18-11007-2018, 2018.
- 1270 Tanimoto, H., Sawa, Y., Yonemura, S., Yumimoto, K., Matsueda, H., Uno, I., Hayasaka, T., Mukai, H., Tohjima, Y., Tsuboi, K., and Zhang, L.: Diagnosing recent CO emissions and ozone evolution in East Asia using coordinated surface observations, adjoint inverse modeling, and MOPITT satellite data, *Atmos. Chem. Phys.*, 8, 3867–3880, 10.5194/acp-8-3867-2008, 2008.

- 1275 Taubenböck, H., Weigand, M., Esch, T., Staab, J., Wurm, M., Mast, J., and Dech, S.: A new ranking of the world's largest cities—Do administrative units obscure morphological realities?, *Remote Sensing of Environment*, 232, 111353, <https://doi.org/10.1016/j.rse.2019.111353>, 2019.
- Tohjima, Y., Kubo, M., Minejima, C., Mukai, H., Tanimoto, H., Ganshin, A., Maksyutov, S., Katsumata, K., Machida, T., and Kita, K.: Temporal changes in the emissions of CH<sub>4</sub> and CO from China estimated from CH<sub>4</sub>/CO<sub>2</sub> and CO/CO<sub>2</sub> correlations observed at Hateruma Island, *Atmos. Chem. Phys.*, 14, 1663–1677, 2014.
- 1280 Turi, G., Lachkar, Z., and Gruber, N.: Spatiotemporal variability and drivers of CO<sub>2</sub> and air–sea CO<sub>2</sub> fluxes in the California Current System: an eddy-resolving modeling study, *Biogeosciences*, 11, 671–690, 10.5194/bg-11-671-2014, 2014.
- Turnbull, J., Rayner, P., Miller, J., Naegler, T., Ciais, P., and Cozic, A.: On the use of <sup>14</sup>C as a tracer for fossil fuel CO<sub>2</sub>: Quantifying uncertainties using an atmospheric transport model, *J. Geophys. Res. Atmos.*, 114, D22302, 2009.
- 1285 Turnbull, J. C., Miller, J., Lehman, S., Tans, P., Sparks, R., and Southon, J.: Comparison of <sup>14</sup>C, CO, and SF<sub>6</sub> as tracers for recently added fossil fuel CO<sub>2</sub> in the atmosphere and implications for biological CO<sub>2</sub> exchange, *Geophys. Res. Lett.*, 33, L01817, 2006.
- Turnbull, J. C., Tans, P. P., Lehman, S. J., Baker, D., Conway, T. J., Chung, Y. S., Gregg, J., Miller, J. B., Southon, J. R., and Zhou, L.-X.: Atmospheric observations of carbon monoxide and fossil fuel CO<sub>2</sub> emissions from East Asia, *J. Geophys. Res. Atmos.*, 116, D24306, <https://doi.org/10.1029/2011JD016691>, 2011.
- 1290 Turnbull, J. C., Sweeney, C., Karion, A., Newberger, T., Lehman, S. J., Tans, P. P., Davis, K. J., Lauvaux, T., Miles, N. L., Richardson, S. J., Cambaliza, M. O., Shepson, P. B., Gurney, K., Patarasuk, R., and Razlivanov, I.: Toward quantification and source sector identification of fossil fuel CO<sub>2</sub> emissions from an urban area: Results from the INFLUX experiment, *J. Geophys. Res. Atmos.*, 120, 292–312, <https://doi.org/10.1002/2014JD022555>, 2015.
- 1295 van der Werf, G. R., Randerson, J. T., Giglio, L., Collatz, G. J., Mu, M., Kasibhatla, P. S., Morton, D. C., DeFries, R. S., Jin, Y., and van Leeuwen, T. T.: Global fire emissions and the contribution of deforestation, savanna, forest, agricultural, and peat fires (1997–2009), *Atmos. Chem. Phys.*, 10, 11707–11735, 10.5194/acp-10-11707-2010, 2010.
- van der Werf, G. R., Randerson, J. T., Giglio, L., van Leeuwen, T. T., Chen, Y., Rogers, B. M., Mu, M., van Marle, M. J. E., Morton, D. C., Collatz, G. J., Yokelson, R. J., and Kasibhatla, P. S.: Global fire emissions estimates during 1997–2016, *Earth Syst. Sci. Data*, 9, 697–720, 10.5194/essd-9-697-2017, 2017.
- 1300 Wang, P., Zhou, W., Niu, Z., Cheng, P., Wu, S., Xiong, X., Lu, X., and Du, H.: Emission characteristics of atmospheric carbon dioxide in Xi'an, China based on the measurements of CO<sub>2</sub> concentration, Δ<sup>14</sup>C and δ<sup>13</sup>C, *Sci. Total Environ.*, 619, 1163–1169, 2018.
- Wang, P., Zhou, W., Xiong, X., Wu, S., Niu, Z., Cheng, P., Du, H., and Hou, Y.: Stable carbon isotopic characteristics of fossil fuels in China, *Sci. Total Environ.*, 805, 150240, <https://doi.org/10.1016/j.scitotenv.2021.150240>, 2022a.
- 1305 Wang, P., Zhou, W., Xiong, X., Wu, S., Niu, Z., Yu, Y., Liu, J., Feng, T., Cheng, P., Du, H., Lu, X., Chen, N., and Hou, Y.: Source attribution of atmospheric CO<sub>2</sub> using <sup>14</sup>C and <sup>13</sup>C as tracers in two Chinese megacities during winter, *J. Geophys. Res. Atmos.*, 127, e2022JD036504, <https://doi.org/10.1029/2022JD036504>, 2022b.
- Wang, Y., Munger, J., Xu, S., McElroy, M. B., Hao, J., Nielsen, C., and Ma, H.: CO<sub>2</sub> and its correlation with CO at a rural site near Beijing: implications for combustion efficiency in China, *Atmos. Chem. Phys.*, 10, 8881–8897, 2010.
- 1310 Wen, X. F., Meng, Y., Zhang, X. Y., Sun, X. M., and Lee, X.: Evaluating calibration strategies for isotope ratio infrared spectroscopy for atmospheric <sup>13</sup>CO<sub>2</sub>/<sup>12</sup>CO<sub>2</sub> measurement, *Atmos. Meas. Tech.*, 6, 1491–1501, 10.5194/amt-6-1491-2013, 2013.
- Wu, F., Li, F., Zhao, X., Bolan, N. S., Fu, P., Lam, S. S., Mašek, O., Ong, H. C., Pan, B., Qiu, X., Rinklebe, J., Tsang, D. C. W., Van Zwieten, L., Vithanage, M., Wang, S., Xing, B., Zhang, G., and Wang, H.: Meet the challenges in the “Carbon Age”, *Carbon Research*, 1, 1, 10.1007/s44246-022-00001-9, 2022.
- 1315 Xu, R., Tong, D., Xiao, Q., Qin, X., Chen, C., Yan, L., Cheng, J., Cui, C., Hu, H., Liu, W., Yan, X., Wang, H., Liu, X., Geng, G., Lei, Y., Guan, D., He, K., and Zhang, Q.: MEIC-global-CO<sub>2</sub>: A new global CO<sub>2</sub> emission inventory with highly-resolved source category and sub-country information, *Sci. China Earth Sci.*, 67, 450–465, 10.1007/s11430-023-1230-3, 2024.
- 1320 Xu, X., Trumbore, S. E., Zheng, S., Southon, J. R., McDuffee, K. E., Luttgen, M., and Liu, J. C.: Modifying a sealed tube zinc reduction method for preparation of AMS graphite targets: Reducing background and attaining high precision, *Nuclear Instruments and Methods in Physics Research Section B: Beam Interactions with Materials and Atoms*, 259, 320–329, <https://doi.org/10.1016/j.nimb.2007.01.175>, 2007.

- 1325 Nuclear Power Industry Report: The Development of Fourth-Generation Nuclear Power Accelerates, and Controllable Nuclear Fusion Moves Forward Steadily (in Chinese): [https://pdf.dfcfw.com/pdf/H3\\_AP202401221617892738\\_1.pdf?1705938486000.pdf](https://pdf.dfcfw.com/pdf/H3_AP202401221617892738_1.pdf?1705938486000.pdf) (last accessed: 14 March 2025) last
- Zazzeri, G., Acuña Yeomans, E., and Graven, H. D.: Global and Regional Emissions of Radiocarbon from Nuclear Power Plants from 1972 to 2016, *Radiocarbon*, 60, 1067-1081, 10.1017/RDC.2018.42, 2018.
- 1330 Zazzeri, G., Graven, H., Xu, X., Saboya, E., Blyth, L., Manning, A., Chawner, H., Wu, D., and Hammer, S.: Radiocarbon Measurements Reveal Underestimated Fossil CH<sub>4</sub> and CO<sub>2</sub> Emissions in London, *Geophys. Res. Lett.*, 50, e2023GL103834, 10.1029/2023GL103834, 2023.
- Zhang, C. L., Wu, G. C., Wang, H., Wang, Y., Gong, D., and Wang, B.: Regional effect as a probe of atmospheric carbon dioxide reduction in southern China, *J. Clean. Prod.*, 340, 130713, <https://doi.org/10.1016/j.jclepro.2022.130713>, 2022.
- 1335 Zhang, J., Liang, Y., Pei, C., Huang, B., Huang, Y., Lian, X., Song, S., Cheng, C., Wu, C., Zhou, Z., Li, J., and Li, M.: Atmospheric CO<sub>2</sub> dynamics in a coastal megacity: spatiotemporal patterns, sea-land breeze impacts, and anthropogenic-biogenic emission partitioning, *EGU sphere*, 2025, 1-30, 10.5194/egusphere-2025-3215, 2025.
- Zhang, L., Ruan, J., Zhang, Z., Qin, Z., Lei, Z., Cai, B., Wang, S., and Tang, L.: City-level pathways to carbon peak and neutrality in China, *Cell Reports Sustainability*, 1, 100102, <https://doi.org/10.1016/j.crsus.2024.100102>, 2024.
- 1340 Zhang, Q., Zheng, Y., Tong, D., Shao, M., Wang, S., Zhang, Y., Xu, X., Wang, J., He, H., Liu, W., Ding, Y., Lei, Y., Li, J., Wang, Z., Zhang, X., Wang, Y., Cheng, J., Liu, Y., Shi, Q., Yan, L., Geng, G., Hong, C., Li, M., Liu, F., Zheng, B., Cao, J., Ding, A., Gao, J., Fu, Q., Huo, J., Liu, B., Liu, Z., Yang, F., He, K., and Hao, J.: Drivers of improved PM<sub>2.5</sub> air quality in China from 2013 to 2017, *Proc. Natl. Acad. Sci.*, 116, 24463-24469, doi:10.1073/pnas.1907956116, 2019.
- Zheng, B., Tong, D., Li, M., Liu, F., Hong, C., Geng, G., Li, H., Li, X., Peng, L., Qi, J., Yan, L., Zhang, Y., Zhao, H., Zheng, Y., He, K., and Zhang, Q.: Trends in China's anthropogenic emissions since 2010 as the consequence of clean air actions, *Atmos. Chem. Phys.*, 18, 14095-14111, 10.5194/acp-18-14095-2018, 2018.
- 1345 Zheng, Y., Cao, W., Zhao, H., Chen, C., Lei, Y., Feng, Y., Qi, Z., Wang, Y., Wang, X., Xue, W., and Yan, G.: Identifying Key Sources for Air Pollution and CO<sub>2</sub> Emission Co-control in China, *Environ. Sci. Technol.*, 10.1021/acs.est.4c03299, 2024.
- Zhou, W., Wu, S., Huo, W., Xiong, X., Cheng, P., Lu, X., and Niu, Z.: Tracing fossil fuel CO<sub>2</sub> using  $\Delta^{14}\text{C}$  in Xi'an City, China, *Atmos. Environ.*, 94, 538-545, 2014.
- 1350 Zhou, W., Niu, Z., Wu, S., Xiaohu, X., Wang, P., Cheng, P., Hou, Y., du, H., Chen, N., and Lu, X.: Recent progress in atmospheric fossil fuel CO<sub>2</sub> trends traced by radiocarbon in China, *Radiocarbon*, 64, 1-11, 10.1017/RDC.2022.32, 2022.
- Zhou, W. J., Niu, Z. C., Wu, S. G., Xiong, X., Hou, Y., Wang, P., Feng, T., Cheng, P., Du, H., and Lu, X.: Fossil fuel CO<sub>2</sub> traced by radiocarbon in fifteen Chinese cities, *Sci. Total Environ.*, 729, 138639, 2020.
- 1355 Zhou, Z., Li, P., Cheng, Z., Li, J., Li, J., Chen, D., Zhang, T., Xiong, X., Sa, R., Ma, S., and Zhang, G.: Selection of background stations and values for urban atmospheric  $\Delta^{14}\text{CO}_2$  observation: a case study in Shenzhen (in Chinese), *Geochimica*, 53, 309-319, 2024.
- Zhu, S., Ding, P., Wang, N., Shen, C., Jia, G., and Zhang, G.: The compact AMS facility at Guangzhou Institute of Geochemistry, Chinese Academy of Sciences, Nuclear Instruments and Methods in Physics Research Section B: Beam Interactions with Materials and Atoms, 361, 72-75, 2015.
- 1360 Zimnoch, M., Jelen, D., Galkowski, M., Kuc, T., Necki, J., Chmura, L., Gorczyca, Z., Jasek, A., and Rozanski, K.: Partitioning of atmospheric carbon dioxide over Central Europe: insights from combined measurements of CO<sub>2</sub> mixing ratios and their carbon isotope composition, *Isot. Environ. Health Stud.*, 48, 421-433, 10.1080/10256016.2012.663368, 2012.
- (Zhanjiang Municipal Bureau of Statistics), Zhanjiang Statistical Yearbook 2024, last

1365